SEA ICE SUBJECTED TO CYCLIC COMPRESSION

Laboratory experiments and a dislocation based model

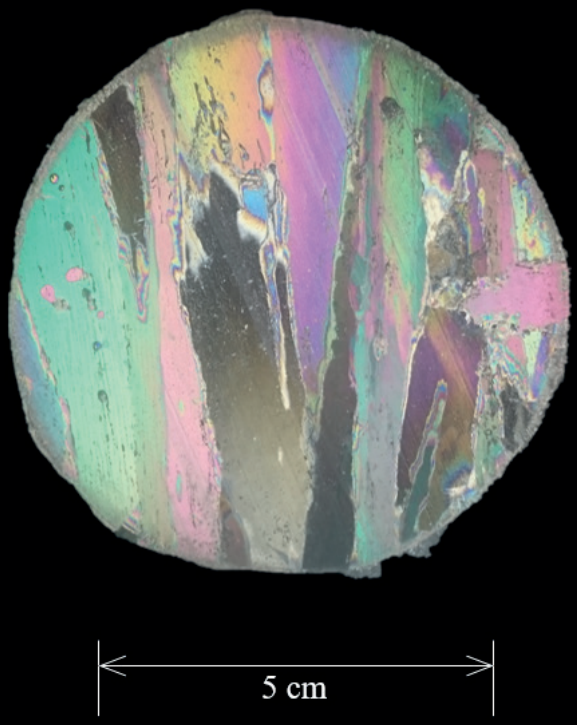

MSc thesis

A. Heijkoop

TU Delft

UNIS

Sea ice subjected to cyclic compression
Laboratory experiments and a dislocation based model

By

Anne-Niekolai Heijkoop

in partial fulfilment of the requirements for the degree of

Master of Science
in Offshore & Dredging Engineering

at the Delft University of Technology,
to be defended publicly on Monday August 28, 2017

Thesis committee:	Prof. Dr. A.V. Metrikine,	TU Delft
	Ir. J.S. Hoving,	TU Delft
	Dr. K.N. van Dalen	TU Delft
	Dr. T.S. Nord,	UNIS

TU Delft

UNIS

Abstract

Wave or vehicular action on an ice sheet as well as structural vibrations and thermally induced loading cause cyclic loading on an ice sheet. To better understand the effects of cyclic loading on the strength of sea ice, cyclic loading tests have been conducted at the University Centre in Svalbard (UNIS). In addition, the corresponding ice behaviour was modelled based on Cole (1995), thereby describing the viscoelastic response of saline ice subjected to a cyclic stress. The aim of this study was to design and execute a reproducible experimental campaign for saline ice subjected to a cyclic compression, and to model the stress-strain relationship of the ice. Specifically, the effects of frequency and displacement amplitude were studied.

The laboratory-grown saline ice was frozen from a mixture of sea water and fresh water with a salinity of approximately 8. The structure was classified as S2 columnar ice through inspection of thin sections. The specimens were retrieved from horizontal and vertical cylindrical cores. The porosities of the specimens ranged from 22 to 34 ppt and the salinities from 2 to 4. The experiments were performed by applying a sinusoidal varying uniaxial displacement of one piston of the loading frame using a stepper engine. An initial compressive load (equivalent to 1 MPa) was reached by applying a constant strain rate.

The model by Cole (1995) uses kinematics to describe the ice behaviour, which is explained by the line defaults in the ice lattice, so-called dislocations. The input parameters of the model are the central relaxation time of dislocation relaxation, the dislocation density and an empirically derived distribution factor. The model results were given by the amplitude and phase lag of the steady-state stress response for an applied sinusoidal strain.

The experimental campaign proved to be reproducible and demonstrated the stress response of saline ice subjected to a cyclic compression well. However, some improvements of the experiments are recommended; most importantly, a higher resolution of the strain sensors and more stringent displacement control, such that the input strain can be defined. The results from the experiments furthermore showed a dependence of the energy dissipation on the loading frequencies, as well as a considerable influence of stress relaxation on specifically the first cycle of the tests.

To compare the tests and the model, the strain signal was filtered to remove the influence of the strain sensor location. The parameter used to compare the experimental results to the model was the loss compliance, which describes the energy dissipation per load cycle and is

derived from the area per loop of the stress-strain curve. The loss compliance was compared to those modelled for parameters given in the literature per frequency. For all amplitudes and frequencies, the test results match well to the model results. Naturally, the viscoelastic model did not capture any of the non-linear phenomena that were observed in the experiments. A discernible trend was an apparent increase in the loss compliance for an increasing frequency or per consecutive test, which may be caused by an increase of the dislocation density.

In conclusion, the experimental method provides a successful experimental campaign that demonstrates the energy dissipation per cycle. The model provides solid results for the steady-state response of saline ice subjected to cyclic compression.

Acknowledgements

The last year I have spent as a guest master student at the University Centre in Svalbard (UNIS) to write my MSc thesis to complete the Masters Programme: Offshore and Dredging Engineering on the Delft University of Technology(TU Delft). Both the thesis and the Masters Programme have been a great learning experience.

This work has been carried out under the supervision of Postdoctoral Fellow Torodd Nord at the Department of Civil and Environmental Engineering, Norwegian University of Science and Technology (NTNU). I cannot thank him enough for offering this project to me and supervising it. I would also like Professor Andrei Metrikine for the valuable comments and continuous discussions and Jeroen Hoving for his useful insights and advice.

The laboratory work would not have been possible without the help and tips from Postdoc Aleksey Shestov, PHd Stipendiat Evgenii Salganik and the logistics department at UNIS.

Furthermore, I want to thank Carmen Klausbruckner and Daniela König for the continuous proofreading.

I would also like to thank Professor David Cole. He lectured at UNIS for two weeks about the model on which I have based my work. During and long after this period, we discussed the topic and both my interest and knowledge on the model were greatly improved.

Table of contents

List of Figures

List of tables

Abbreviations

CRREL	Cold Regions Research and Engineering Laboratory'
CSR	Constant Strain Rate
FRYSIS	Freezing tank at UNIS
g	gram
Hz	Hertz
i.e.	Id est
kg	kilogram
kN	kilonewton
KOMPIS	Mobile compression rig
min	minute
ml	milliliter
mm	millimeter
MPa	megapascal
eV	elektronvolt
N	Newton
nm	nanometer
NTNU	Norwegian University of Science and Technology
ppt	parts per thousand
s	second
t	ton
UNESCO	United Nations Educational Scientific and Cultural Organization
UNIS	University Centre in Svalbard
USA	United States of America
VWR	Van Waters Rogers
µm	micrometer

1. Introduction

The United States Geological Survey estimates that about 30 % of the world's undiscovered gas and 13 % of the world's undiscovered oil is located in the area north of the Arctic circle (Gautier et al., 2009). While many Arctic onshore areas have already been explored, offshore exploration has been scarce so far. Considering that much of these potential gas and oil resources are located on continental shelves beneath less than 500 m of water, Arctic regions could become more prominent areas of (offshore) oil and gas production in the future, depending on technical and economic developments. For natural gas the prospects are interesting in particular, as the estimated energy-equivalents of gas are three times as large as for oil in the Arctic (Gautier et al., 2009). However, due to the decrease in oil and gas prices in recent years in combination with an increased focus of international politics on climate change mitigation policies Arctic resource discovery and development activities have been stalled lately (Gulas et al., 2017), but could possibly be revived with an increase in oil and gas prices, and a shift in global politics back to promoting non-renewable energy carriers.

Even if Arctic offshore oil and gas exploration prove to be less popular than anticipated, it is still necessary to study the technical difficulties potential offshore infrastructures would encounter in these areas, whereby sea ice and its impact on such structures appears to be the biggest challenge of for operations in Arctic waters (Timco and Weeks, 2010). In addition, currently plans to develop wind farms in areas such as the Baltic Sea and the Great Lakes are under development (Hendrikse, 2017), which would also have to be technically prepared for potential confrontations with ice.

The rheological properties of sea ice are poorly understood and very complex, and depend on many factors most importantly the microstructure of the ice. While model developments started by Sinha (1978) that relates stress exerted on the ice to the creep behaviour of the ice, said equations are primarily empirical, and a fundamental mechanistic description of the relationship between the two parameters (i.e. stress and strain) remains elusive. It was only until the late nineties that a study towards the cyclic loading response of sea ice was conducted (Dempsey, 2000).

A more physics based model has been developed by Cole (1995) to relate the stress exerted on ice to the resulting, stress-controlled, deformation of said ice. These efforts were preceded by the findings of Mellor and Cole (1981) on the cyclic loading of ice. The stress-controlled tests on which this model is based are useful for elucidating the constitutive relation between the parameters (i.e. stress and the different types of strain) of sea ice. However, while the

developed equations successfully predict the ice deformation based on a certain (cyclic) stress exerted on the ice, it is not yet confirmed, whether they can be applied to the inverse relationship, i.e. predict the resulting stress when a certain strain is applied (in so-called strain-controlled tests). Therefore, this study tried to apply the model on results obtained from strain-controlled tests, to see if the inverse relationship holds. A reproducible experimental campaign was designed and reviewed

The structure of this thesis is as follows. In chapter 2, a literature study is conducted to review the practical use of the findings of this work, to better understand the material, sea ice, the response of a material to a cyclic loading or strain and the model derived by Cole. In chapter 3, the designed experimental method is elaborated on, from ice specimen production, to the cyclic compression tests, the characterization of the ice specimens and the data processing. The experiment design, the experimental results and the model predictions follow in chapter 4. The conclusions and recommendations are given in the last chapter.

2. Theory of sea ice, viscoelasticity and the model of sea ice

2.1. Sea ice

2.1.1. Ice formation and growth

The specimens used for the experiments were laboratory grown sea ice. An understanding of the sea ice growth as it occurs in nature is important to assess the quality of the laboratory growth method and to interpret the ice characteristics.

Sea ice is mainly composed of solid ice (water ice), brine, gas and several types of solid salts. Different ice structures can result from environmental variations. The three most common structures are distinguished: granular, columnar and skeletal ice. A typical first year sea ice layer consists of an upper layer of granular ice, above a layer of columnar ice, above a skeletal layer (Erland M Schulson and Duval, 2009) as shown in Figure 2.1.

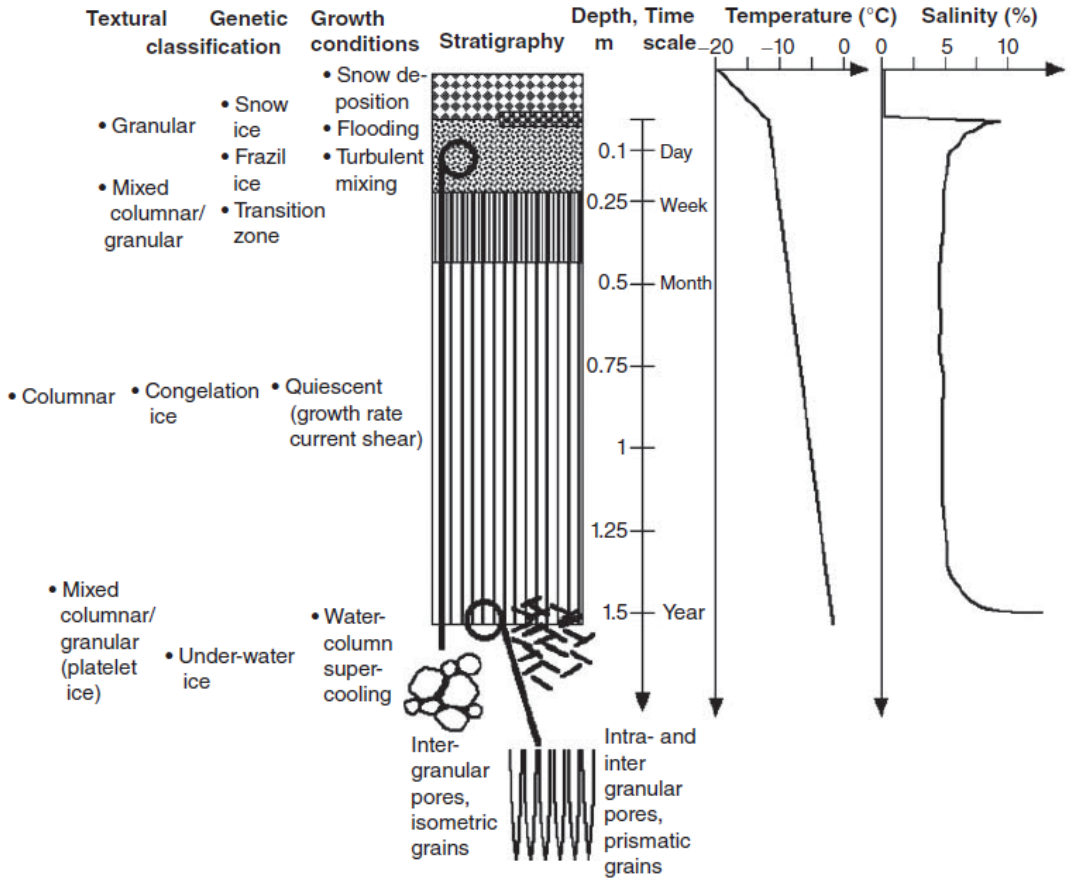

Figure 2.1 Schematic summarizing the main ice textures, growth conditions and timescales and typical winter temperature and salinity profiles for first-year sea ice (Thomas, 2016)

The initial ice formation, the so-called nucleation, occurs in the uppermost layer of the sea, since this process is greatly enhanced at the air-water interface compared to the bulk water (Shaw, Durant and Mi, 2005). Due to the faster transport of heat compared to ions in seawater this layer of the sea will have been lowered to or slightly below the freezing point, thus super cooled. In polar regions snow crystals are continuously deposited on the surface layer, constituting instant nuclei from which the ice crystals start growing (Weeks and Ackley, 1982). In ice tanks the so-called water-spray method is commonly used to replicate this process, whereby water droplets are sprayed into the cold air and frozen before reaching the water surface, as introduced by Lavrov (1971).

The granular layer of the ice is formed at the top and behaves usually uniform in all directions i.e. isotropic. Columnar ice is formed below this granular layer or even at the sea surface when the environmental conditions are calm. Columnar ice consists of columnar crystals located (nearly) over the entire depth of the ice layer. The growth direction of the crystals aligns with the direction of the heat flow, i.e. is vertical and behaves mechanically anisotropic.

The focus of this study lies on the columnar layer. The granular layer and the skeletal layer are therefore not further discussed. The microstructure of the columnar layer is further explained in section 2.1.5.

2.1.2. Ice density

Knowledge of the density of sea ice is important, for the calculation of the porosity, which is explained in section 2.1.4. The density of first-year sea ice was collected and reviewed by multiple studies. The reported values vary over a wide range of $720\ \mathrm{kg/m^3}$ to $940\ \mathrm{kg/m^3}$with an average of $910\ \mathrm{Mg/m^3}$. It was stated that a reasonable estimate for ice specimens of first-year sea ice should be $0.920\ \mathrm{Mg/m^3}$(Timco and Weeks, 2010).

A commonly used method to estimate the ice density is the mass/volume method, where the mass is weighed on a scale and the volume follows from the dimensions measured with a caliper. This method may have a large measuring error so that a method for a more precise density value is required. The best available method to capture the ice density is the hydrostatic weighing method (Pustogvar and Kulyakhtin, 2016). For this method, the weight of the specimen in air is compared to the weight of the submerged specimen, whereby the density of the submerging fluid is known. The method has a 20 times lower measurement uncertainty (0.2 %) in comparison with the mass/volume method for ice specimens with

lengths and diameters of ~70 mm. The ice density in the hydrostatic weighing method is derived from:

$$\rho_{ice} = \frac{M_{air}}{M_{air} - M_{par}} \rho_{par} \tag{2.1}$$

Where M_{air} is the mass of the specimen in air, M_{par} is the mass of the specimen submerged in paraffin and ρ_{par} is the density of the paraffin.

2.1.3. Ice salinity

The bulk ice salinity, is the fraction by weight of the salts contained in a unit mass of ice. It is calculated as the ratio of grams per kilo seawater, yet no unit is assigned to the salinity. To measure bulk salinity, a core of sea ice is quickly contained and melted after its retrieval, after which a conductivity meter is used to calculate the salinity based on temperature and conductivity (Timco and Weeks, 2010).

In first-year sea ice an often-observed ice salinity distribution is the C-shape profile, since the salt in the top layer is often trapped in closed voids due to the fast initial growth of the ice and whereas salts originally located within intermediate layers are transported downwards towards the ice-water interface. The movement of brine is due to the temperature gradient in the pocket. Brine drains through the brine channels, leaves the ice through the skeletal layer and therefore older ice contains less salt.

Since older first-year ice has usually grown for a longer time, the ice thickness of first year sea ice is related to the bulk salinity of the ice. Kovacs (1996) combined thickness data from first-year sea ice and plotted the curve depicted in Figure 2.2. For an increasing ice floe thickness, the bulk salinity goes asymptotically towards a low value of around 5. Low salinity ice is easier to handle during experiments (discussed with Knut Høyland, 2016)

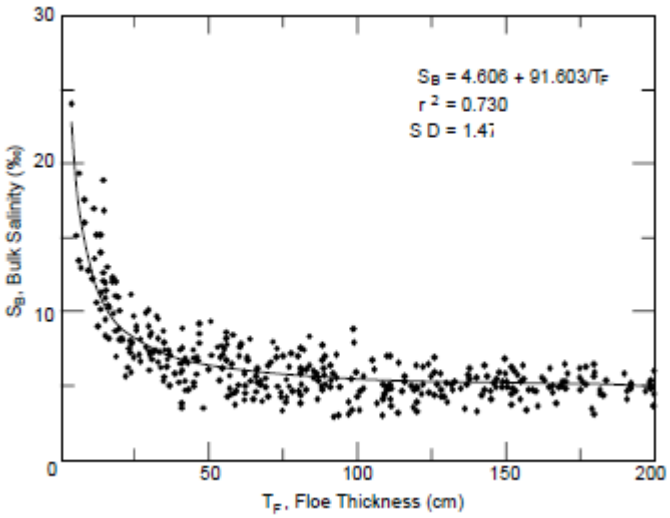

Figure 2.2 All Arctic and Antarctic first-year sea-ice bulk salinity vs. floe thickness data compiled from numerous sources (Kovacs, 1996)

The salinity of sea water in open oceans is typically between 32 and 37 with local variations. Salinities in the Arctic can typically be lower (<30) with an associated sea ice salinity upon formation between 5 and 10 and as visible in Figure 2.2 decreasing in time. The sea water in the Baltic Sea is brackish (<24.7) and highly variable between 8 and 20. In the upper Bay of Bothnia the salinity is low but high enough to produce typical sea ice microstructure with an associated sea ice salinity (<2) (Granskog et al., 2006).

2.1.4. Ice porosity

The sea ice properties have been historically analysed with the brine volume and gas volume present within the ice. The total porosity, ν_T is the sum of the brine porosity,ν_b, i.e. the volume of brine per unit volume, and the gas porosity, ν_g, i.e. the volume of gas per unit volume present in the ice (Timco and Weeks, 2010).

$$\nu_T = \nu_b + \nu_g \text{ [ppt]} \tag{2.2}$$

The knowledge of the total porosity of sea ice is important for interpreting its physical properties. The gas and brine porosities of sea ice, separately considered, are also important parameters, especially in case of low-salinity sea ice (Cox and Weeks, 1983). More specific to this work, the specimen porosities have an important influence on the anelastic behaviour of saline ice. A power law relationship with an exponent ≈ 2 was found during cyclic loading experiments between the later introduced loss compliance and the brine porosity. The brine porosity also has a complex effect on the elastic modulus of saline ice, whereas the effect of gas porosity on the elastic modulus is clear (Cole, 1998) and is not further implemented.

The porosity cannot easily be measured directly, but can be derived from the state parameters temperature, salinity and density, under the assumption that the pure ice, the brine and the solid salts exist in thermal equilibrium.

The calculation of the total, gas and brine porosities of saline ice colder than $-1.9℃$ is described by Cox and Weeks (1983). The following parameters are needed:

- ice density ρ_i: measured
- ice salinity S_i: measured
- Temperature T_i: measured

Other parameters found in the equations are derived from tables and included in the temperature dependent variables F_1 and F_2 for which is referred to the works of Cox and Weeks (1983).

The pure ice density, ρ_{pi} is found in Pounder (1965) as:

$$\rho_{pi} = 0.917 - 1.403 \cdot 10^{-4} T = 0.9168\ (1 - 1.53 \cdot 10^{-4} T) \tag{2.3}$$

Where the temperature, T, is given in ℃. All parameters are unique functions of temperature and therefore the brine (η_b) and gas volume ratio (η_a) can be written as:

$$\eta_b = \frac{\rho_i S_i}{F_1(T)}\ [-] \tag{2.4}$$

and

$$\eta_a = 1 - \frac{\rho_i}{\rho_{pi}} + \rho_i S_i \frac{F_2(T)}{F_1(T)}\ [-] \tag{2.5}$$

where S_i is the bulk salinity of the ice. The porosities are often denoted as $\nu_a = 1000\eta_a$ [ppt] and $\nu_b = 1000\eta_b\ [ppt]$, are often denotes with units as parts per thousand, for readability. The total porosity of the material is $\nu_t = \nu_a + \nu_b$.

2.1.5. Microstructure of sea ice

The microstructure of sea ice has a major influence on the mechanical behaviour of ice and is increasingly studied to understand the its relationship to the flow and fracture of ice (Cole, 2001). In the following, the microstructure of ice grains and dislocations in the lattice, a large contributor to the anelastic behaviour, are explained.

2.1.5.1. Ice grains

The structure of pure ice is hexagonal (classified as Ih) and well established. During ice growth, the water molecules grow in a structure where the oxygen atoms of water molecules

connect with the hydrogen atoms of other water molecules. Due to the angle between the hydrogen atoms in a water molecule, the unit cell of ice has a tetrahedral structure, visible in Figure 2.3. Any type of ice is built from these units. The covalent bonds joining the oxygen atom to hydrogen atoms in a molecule are strong and the hydrogen bonds linking the molecules are weak resulting in a low, in comparison with metals, melting temperature of ice.

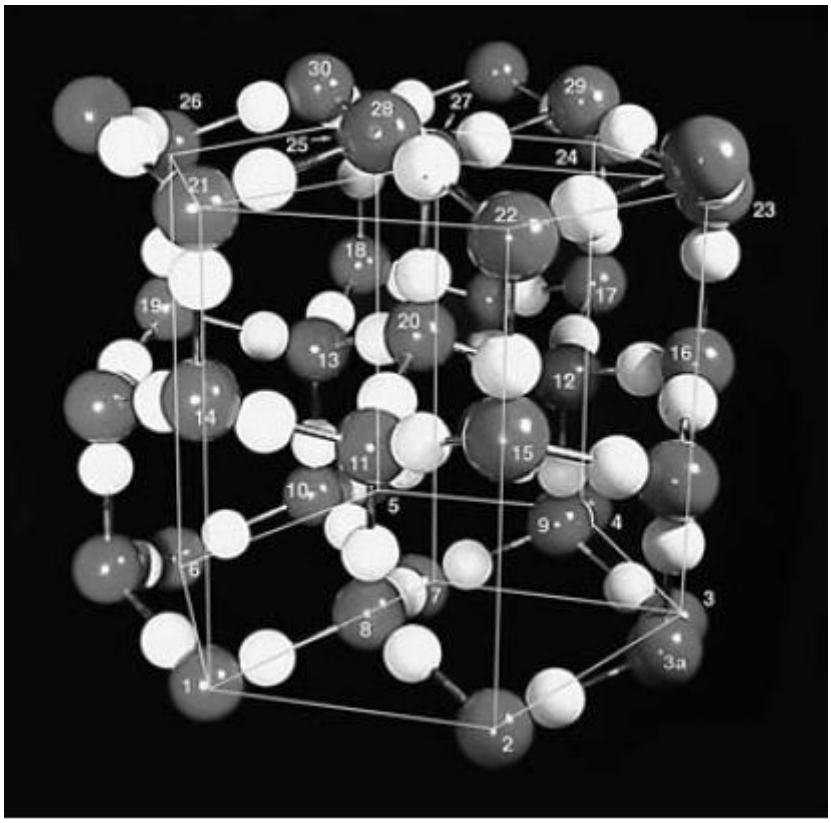

Figure 2.3 Photograph of a ball and stick model of the crystal structure of ice (Ih). The larger balls represent oxygen and the smaller balls, hydrogen. The sticks represent hydrogen bonds between H2O molecules. The corners of the Ih unit cell are delineated by oxygen atoms 1, 2, 3, 7, 21, 22, 23, 27.

A hexagonal structure is characterized by a c-axis, normal to the basal plane (the hexagon). In Figure 2.5, the basal plane is denoted as 0001, the prism faces as 1010, 0110 and 1100 and are characterized as the a-axes. The c-axis is in the direction of 1120. The a-axes are in the basal plane and directed towards the different prism faces, see Figure 2.4. The crystals may grow slowly in the direction of the c-axis (S1 ice) or more rapidly from the prism faces (S2 ice), forming grains. The microstructure of ice floats can be classified with these terms.

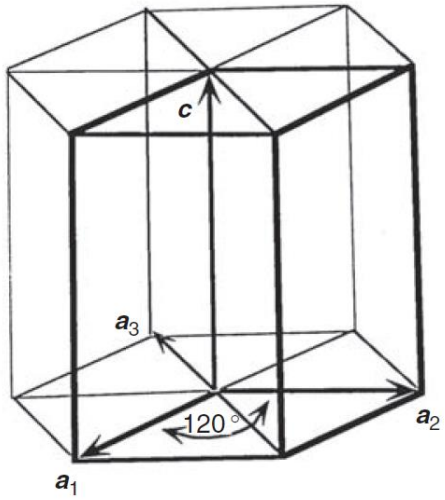

Figure 2.4 C-axis and a-axes (Schulson and Duval, 2009)

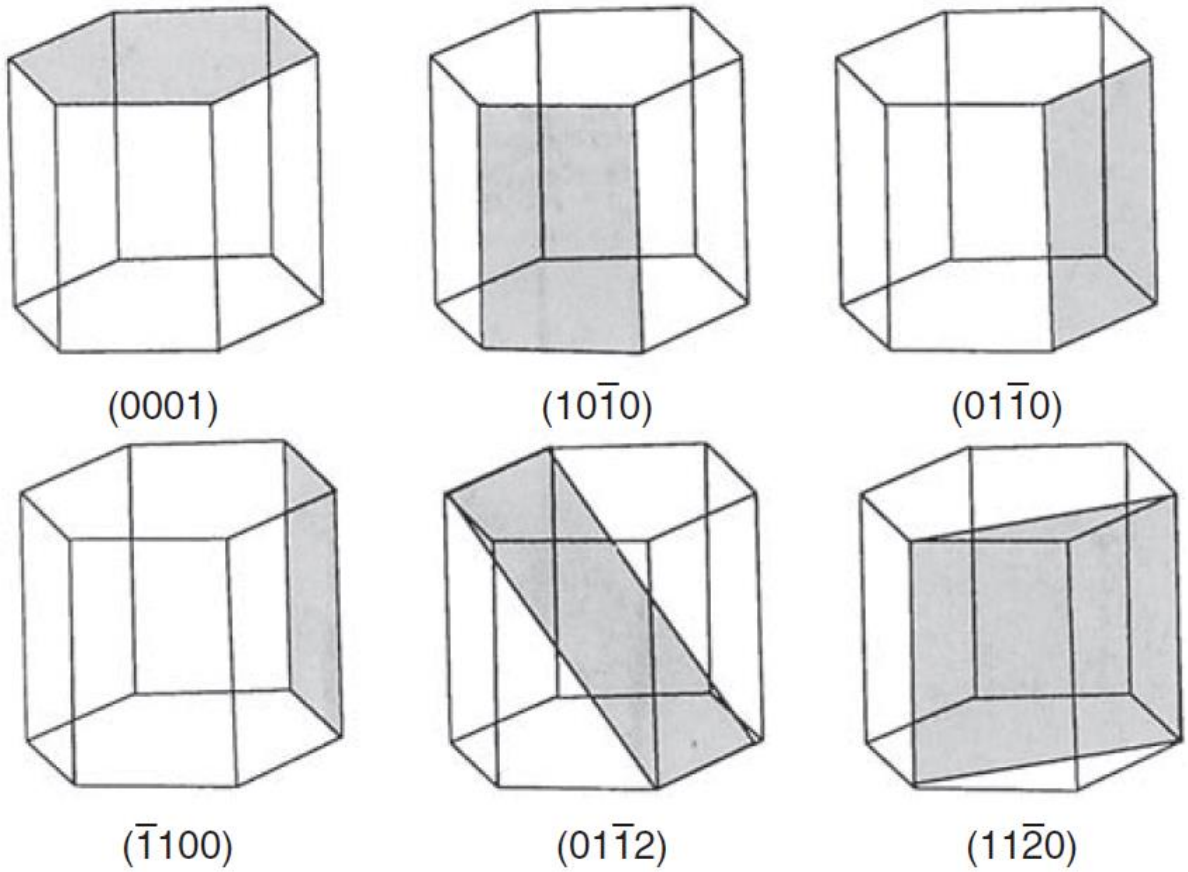

Figure 2.5 Miller-Bravais notation for planes in unit cell (Schulson and Duval, 2009)

The bulk of ice throughout the thickness of the sheet is secondary ice (S). The preferred orientation of the individual grains conveys to the number: 1,2 or 3 and combined three

classes are identified: S1, S2 and S3. For the S1 class the c-axes are oriented mostly vertical, for the S2 class the c-axes are randomly oriented horizontally and for S3 ice the c-axis are oriented horizontal and aligned in a certain direction. The bubbly ice of glaciers and polar ice sheet formed by snow compression is usually the S1 class of ice and can be considered isotropic. Since the ice cover in the Arctic Ocean grows unidirectional, it is composed of columnar shaped grains. Its mechanical behaviour is considered anisotropic.

There are two varieties of columnar ice: unaligned (S2) and aligned (S3). In the former, the ice properties in the horizontal plane are independent of the direction, since the c-axes of the crystals are oriented randomly (but directed horizontally; S2 ice). For the second variety (S3), the c-axes are aligned in one direction and the mechanical properties dependent on this direction (S3 ice). The mean current direction beneath the fast ice is believed to cause the strong c-axis alignment. For both varieties, the ice is mechanically anisotropic. (Timco and Weeks, 2010; Schulson and Duval, 2009; Weeks and Ackley, 1982). The alignment of the c-axis can influence the effective modulus of first-year sea ice (Cole, Johnson and Durell, 1996).

2.1.5.2. Dislocations in ice

A major cause for viscous and anelastic deformation in ice is the plane glide motion of dislocations, which is defined by Hondoh (2000) as: “the motion on a plane (glide plane) parallel to both the Burgers vector and the dislocation line”. The concepts of viscosity and anelasticity are explained in section 2.2.2. A dislocation is “a boundary lone of a region where part of the crystal has been displaced relative to another part” (Glen, 1974). The magnitude and direction of the lattice distortion, resulting from a dislocation in a crystal lattice, is represented by the Burgers vector, i.e. the material above the plane moves relative to the material below by an amount equal to the Burgers vector. One type of dislocations, a so-called edge dislocation, or line dislocation, the lattice and the Burgers vector are displayed in Figure 2.6. An analogy to a dislocation is presented by Nowick and Berry (1972) who state that in principle a dislocation could be created by making a cut in the surface of a crystal, displacing the upper part by a distance b and welding the material back together.

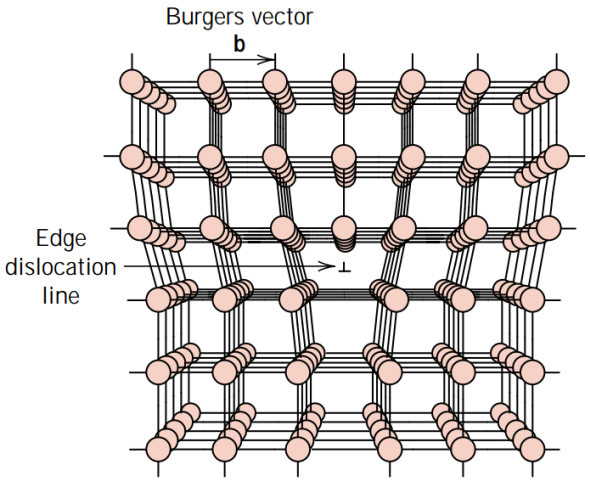

Figure 2.6 Edge dislocation in the lattice (**Callister**, **2001**)

The motion of the line dislocations in ice, allows ice to deform under an applied stress. The lattice of ice consists of oxygen and hydrogen atoms, where for a 'perfect lattice' every oxygen atom is surrounded by four hydrogen atoms. The propagation of the dislocation results in an increase of the number of hydrogen atoms. The protons switch from oxygen atom, which remain in their tetrahedral coordination, with the surrounding oxygen atoms (Wilson and Marmo, 2000).

The method to observe and study dislocations in ice is synchroton X-ray topography (Baker, 2002). This method was first used on ice by R.W. Whitworth's group in 1986 and was later used by Baker et al. (2000) to observe dislocation behaviour in polycrystalline ice under creep conditions. This behaviour was observed in the temperature range of 0 to -15°C, but not at colder temperatures. A frequently occurring load in naturally deforming ice is loading parallel to the basal plane, i.e. in horizontal direction for columnar ice. The grain boundaries were observed to be the only source of lattice dislocations, while nucleation mechanisms inside the grains were not important. Therefore, the dislocation motions were largely occurring at the grain boundaries. A photo of dislocations in ice, using X-ray topography is shown in Figure 2.7.

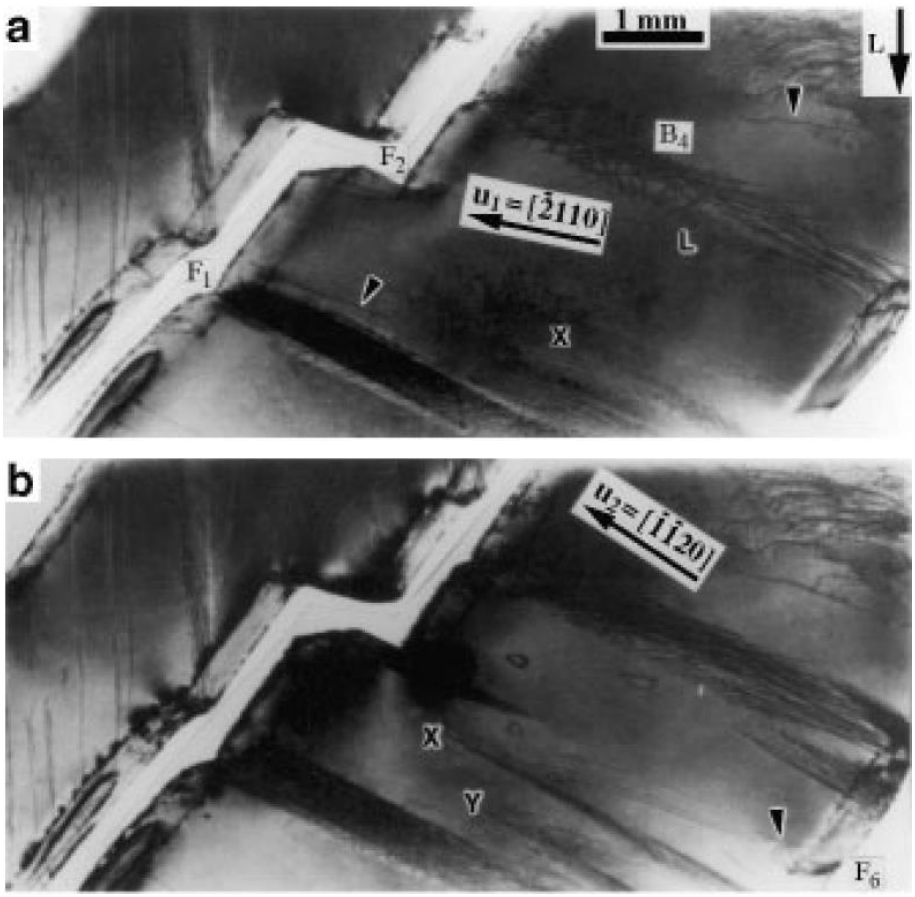

Figure 2.7 Change of dislocations due to creep stress, the blackening from before (a) the creep stress and after (b) is due to an increase in dislocation density (Baker, 2002).

The number of dislocations in a material is called the dislocation density. It is expressed as the total dislocation length per unit volume. The units of the dislocation density are millimeters of dislocation per cubic millimeter. The dislocation densities of carefully solidified metal crystals are found close to 103 mm^{-2} and for heavily deformed metals at an order of 109 to 109 mm^{-2}(Callister, 2001). For the deformation of ice, only the mobile dislocation density, thus the dislocations that move, are considered. For laboratory prepared saline ice this is in the order of 108 mm^{-2}. However, note that this value is the value that is found by either X-ray topography, cyclic tests or a stress relaxation test (Cole, 1998). The dislocation density increases whenever stress is applied higher than approximately 0.3 MPa and is therefore influenced most importantly the stress history on the ice.

In short, edge dislocations are a linear defect in the crystal structure of ice. The resistance to motion supports anelastic (delayed elastic) and viscous (delayed permanent, due to migration of dislocations) straining. The dislocations on basal planes are most important to explain anelastic and viscous behaviour. The dislocations are quantified in terms of dislocation

density: the length of dislocations per unit volume of material $\mathrm{mm/mm^3}$ or shortened to $\mathrm{mm^{-2}}$.

2.2. Viscoelasticity

From experiments, it was shown that sea ice exhibits high levels of anelastic behaviour under a high range of conditions (Cole and Durell, 1995). This section explains the different experiments that can be conducted, the concepts of anelasticity and viscoelasticity and response functions. All concepts are later used for the description of the model.

2.2.1. Stress and strain

The ice is tested for strength and stiffness by applying a cyclic compression to a test specimen. The change in length of the specimen per unit length may be given by the longitudinal strain ε:

$$\varepsilon = \frac{L - l}{L} = \frac{\Delta L}{L} \; [-] \tag{2.6}$$

where L is the initial length of the specimen, l the actual length, ΔL the change in length due to an applied load. The definition in Equation (2.6) is the *engineering strain* and later referred to as the *strain*. For small strains, $\varepsilon < 0.01$, the engineering strain is approximately equal to the true strain. In this work, a positive sign denotes a compressive strain.

The axial force in the test specimen is N [N] and it assumed an evenly distributed force over the cross-sectional area of the specimen. The intensity of the normal force per unit cross-sectional area, A [$\mathrm{mm^2}$], is the normal stress, later referred to as the *stress* σ:

$$\sigma = \frac{N}{A} \; [\mathrm{MPa}] \tag{2.7}$$

Since the focus of this thesis is on the longitudinal change and the change of diameter is neglected, the equation for the nominal normal stress, or engineering stress is used. In this work, a positive sign denotes a compressive stress.

To analyse the behaviour of a material under various levels of loading a stress-strain diagram is created, by plotting the stress on the vertical axis and the strain on the horizontal axis (Irgens, 2008).

2.2.2. Viscoelasticity and anelasticity

Most solid materials are described, for small strains, by Hooke's law of linear elasticity: The strain is proportional to the stress and for one dimension Hooke's law is:

$$\sigma = E\varepsilon \tag{2.8}$$

with E as *Young's*, or *elastic modulus*. Inversely, Hooke's law for elastic materials can be written as:

$$\varepsilon = D\sigma \tag{2.9}$$

where D is the reciprocal of E ($D = E^{-1}$) and called the modulus of compliance, or simply the *compliance* (Nowick and Berry, 1972; Lakes, 2009) as the ratio of the strain to stress, not to be confused with the inverse of stiffness.

A viscous fluid obeys:

$$\sigma = \eta\dot{\varepsilon} \tag{2.10}$$

where the stress is proportional to the strain rate $\dot{\varepsilon}$ through the viscosity η. However, in reality all materials differ from the ideal elastic materials by, for example, both viscous-like and elastic characteristics. For viscoelastic materials, the relationship between stress and strain depends on time and the stress is a function of the strain and the strain rate.

$$\sigma = \eta\dot{\varepsilon} + E\varepsilon \tag{2.11}$$

A subgroup of the viscoelastic materials is the *anelastic solid*: these have a unique equilibrium configuration and recover fully after removal of the load. To explain anelasticity first three postulated defining elastic are explained.

The three postulates defining ideal elastic behaviour are implicit in Equation (2.10) and Equation (2.11):

1. The strain response to each level of applied stress (or vice versa) has a unique equilibrium value.
2. The equilibrium response is achieved *instantaneously.*
3. The response is *linear* (e.g., doubling the stress doubles the strain).

The consequence of condition 1 is the *complete recoverability* of the response upon the release of the applied stress or strain. If each of the conditions is lifted in various combinations, different behaviours result. If all conditions apply ideal elasticity is the case. If the condition of instantaneity is lifted, the behaviour known as anelasticity is produced. Anelasticity is a special case of linear viscosity for which both instantaneity and complete recoverability are lifted. Therefore anelastic behaviour is a type of mechanical behaviour described as 'delayed elastic', thus time dependent (Sinha, 1978), with the following three properties (Nowick and Berry, 1972).

1. For every stress, there is a unique equilibrium value of strain and vice versa.

2. The equilibrium response is achieved only after the passage of sufficient time.
3. The stress-strain relationship is linear.

The stress-strain curve of a linearly elastic material is a straight line with a slope proportional to the elastic modulus. During a constant strain rate, both time and strain increase together, therefore a linearly viscoelastic material shows a curved stress-strain curve (Lakes, 2009).

2.2.3. Mechanical models and anelasticity

The behaviour of a material governed by any differential stress-strain equation can be visualized using mechanical models consisting of Hookean springs and Newtonian dashpots in series or parallel. For an ideal elastic material, the appropriate model is the Hookean spring with the following relationship:

$$F_K = kx \tag{2.12}$$

Where the force F is equivalent to the stress σ, the displacement x to the strain ε and the spring constant k to the modulus E. Such a spring stores energy in a reversible way and returns to zero displacement when the force is removed. The second element, that needed to provide internal friction is the Newtonian dashpot, represented by a piston moving in an ideally viscous fluid, where $\sigma = \eta\dot{\varepsilon}$ where η is the viscosity of the dashpot. A dashpot alone represents a viscous liquid and needs to be combined with springs to describe solids.

To form a model, mechanical elements may be combined either in series or in parallel. In series, the stresses per element (1 and 2) are equal, while the strains are additive.

$$\varepsilon = \varepsilon_1 + \varepsilon_2, \qquad \sigma = \sigma_1 = \sigma_2 \tag{2.13}$$

And for a parallel combination:

$$\varepsilon = \varepsilon_1 = \varepsilon_2\,, \qquad \sigma = \sigma_1 + \sigma_2 \tag{2.14}$$

The simplest models which combine more than one element are a spring and dashpot in parallel, is called the *Kelvin-Voigt model*, and a spring and dashpot in series called a *Maxwell model.* The properties of the Kelvin-Voigt and Maxwell model are shown in Figure 2.8. and Figure 2.9 respectively.

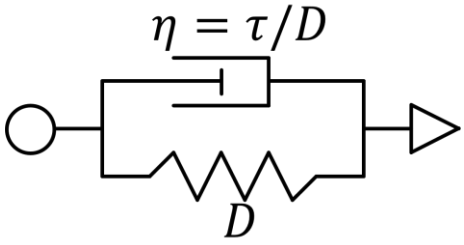

Figure 2.8 Kelvin-Voigt model

Figure 2.9 Maxwell model

2.2.3.1. Kelvin-Voigt model

In the Kelvin-Voigt model the spring is described for convenience by its compliant constant $D = E^{-1}$. The viscosity η is written as τ/D with τ has dimensions of time. The spring and dashpot are placed parallel.

The Kelvin-Voigt model exhibits the following features: no instantaneous deformation upon application of a stress, due to the dashpot, thus at $t = 0$ the stress is sustained by the dashpot only. Over time, the dashpot will dissipate energy until as $t \to \infty$ the velocity is zero and thus the stress is completely taken by the spring. When the stress is released, the dashpot resists a sudden change. The spring maintains the stress, σ_0, and the dashpot must be subjected to a stress $-\sigma_0$. Over time, the dashpot moves back into its original position until the stresses at both elements are zero.

The differential equation for the Kelvin-Voigt model is derived using $\varepsilon_1 = D\sigma_1$ for the spring and $\dot{\varepsilon}_2 = D\sigma_2/\tau$ and the rules for parallel elements. Thus ε_1, ε_2, σ_1 and σ_2 are eliminated to obtain:

$$D\sigma = \varepsilon + \tau\dot{\varepsilon} \tag{2.15}$$

2.2.3.2. Maxwell model

In the Maxwell model, the spring is described by its stiffness or modulus E, and the in series placed dashpot by τE.

The qualitative features of a Maxwell model are as follows. Upon a sudden application of stress, the spring suffers an instantaneous strain. Over time linear viscous creep occurs due to the dashpot. In the case of a sudden application of strain, there will be an instantaneous stress in the spring and the dashpot will dissipate energy over time until full stress relaxation has occurred. The differential equation for the Maxwell model is derived using $\sigma_1 = E\varepsilon_1$ and $\sigma_2 = E\tau\dot{\varepsilon}_2$ resulting in:

$$\tau\dot{\sigma} + \sigma = \tau M\dot{\varepsilon} \tag{2.16}$$

2.2.3.3. Standard Anelastic Solid

These two models do not exactly describe the anelastic behaviour defined by the three conditions. The Kelvin-Voigt model does not respond immediately, whereas the Maxwell model does not return to its initial state after release of the stress or. Therefore, a three-parameter model was considered:

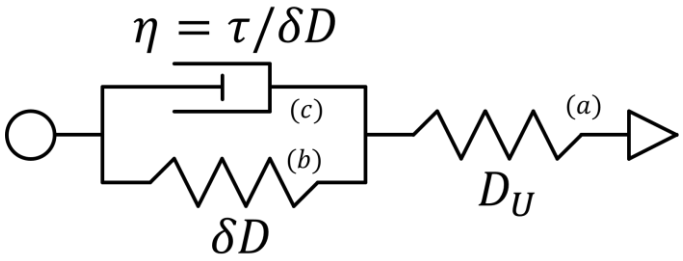

Figure 2.10 Standard Anelastic Solid

The instantaneous elastic response characteristics of a crystal was added to the model by attaching a spring in series to a Kelvin-Voigt model, resulting in the so-called *Standard Anelastic Solid* or *Zener model.* The compliance of the spring in the Voigt unit is called δD, the compliance of the spring in series is called D_U and similarly to the Kelvin-Voigt model, the dashpot is described as function of the relaxation time τ and the compliance of its parallel spring as shown in Figure 2.10.

The qualitative features of this model are as follows: Upon application of a stress at $t = 0$, the extra spring immediately deforms and the Voigt unit remains unchanged due to the dashpot. Over time, the dashpot yields, while transferring stress to the parallel spring until the stress in the dashpot has completely vanished. At this point no further changes to the system occur with time. The strain per unit stress goes from the instantaneous, or un-relaxed, value D_U to a final, or relaxed, value of D_R. The compliance of the in-series spring is D_U and the combined compliance of both springs must be D_R. If compliance of the spring in parallel is called δD, the relaxed D_R is given by $D_U - \delta D$.

Upon application of a strain ε_0, the spring in parallel will be extended and over time the dashpot will start to move until the stress in the dashpot is zero. The stress in the dashpot will move from ε_0/D_U to a final value of $\varepsilon_0/(D_U + \delta D)$.

This model is capable of stress relaxation and creep behaviour. Its differential stress-strain equations follow from the relations $\varepsilon_a = D_U\sigma_a, \varepsilon_b = \delta D\sigma_b$ and $\dot{\varepsilon}_c = \delta D\ \sigma_c/\tau$ and the rules for placing elements in series or parallel:

$$\varepsilon = \varepsilon_a + \varepsilon_b, \qquad \varepsilon_b = \varepsilon_c$$
$$\sigma = \sigma_a = D_U^{-1}\varepsilon_a = \sigma_b + \sigma_c = \delta D^{-1}(\varepsilon_b + \tau\dot{\varepsilon}_c) \tag{2.17}$$

Where the stress and strains per element can be eliminated leading to:

$$D_R\sigma + \tau D_U\dot{\sigma} = \varepsilon + \tau\dot{\varepsilon} \tag{2.18}$$

Where $D_R = D_U + \delta D$. Both Figure 2.10 and Equation (2.18) represent the Standard Anelastic Solid (Nowick and Berry, 1972) .

2.2.4. Quasi-static response functions

Viscoelastic behaviour may be represented mathematically by a variety of functions of time and frequency. The dynamic modulus $E^*(\nu)$[1] and dynamic compliance $D^*(\nu)$; the relaxation function $E(t)$ and the creep function D(t) Since the dynamic functions are regarded as most closely related to direct perception, these are useful to derive from the viscoelastic model to describe the behaviour (Lakes, 2009).

An experiment for which the applied stress or strain is held for a period of time is termed quasi-static. For viscoelastic materials, the phenomena, among others, of creep and stress relaxation occur. Two phases, loading and recovery.

2.2.4.1. Creep and stress relaxation

In the creep experiment a constant stress σ_0 is applied abruptly at $t = 0$ and held constant while the strain ε is observed. The experiment is mathematically described by:

$$\sigma(t) = \sigma_0 H(t) \tag{2.19}$$

Where $H(t)$ is the unit step function, or *Heaviside function* defined as zero for t less than zero and one for t greater than zero. Different definitions for $H(t)$ exist (which include the jump discontinuity at $t = 0$), but the given one explains its behaviour well enough for the timescale of this work:

$$H(t) = \begin{cases} 0, t < 0 \\ 1, t > 0 \end{cases} \tag{2.20}$$

The strain, $\varepsilon(t)$, of the viscoelastic material will increase over time with the following ratio:

$$D(t) = \frac{\varepsilon(t)}{\sigma_0} \tag{2.21}$$

where $D(t)$ is called the *creep compliance* or simply the creep function. The stress input and strain response for several types of materials are shown in Figure 2.11. The release of the load

[1] Different symbols for E and J are used in the literature. Since a notable part of this work refers to the work of Cole, the repective symbols of M and D are used for mentions of modulus and compliance.

is included in this figure and explained later. The intercept of the creep curve on the strain axis is ascribed to instantaneous elasticity. The anelastic response would be similar to the viscoelastic curve, but during the recovery after enough passage of time the material goes back to its initial state, thus, when the strain response reaches zero.

The stress history is the cause whereas the strain is the effect. The corresponding form of the strain response $D(t) = d(t)H(t)$ with $d(t)$ as a function over the entire time scale. The physical concept of causality, where the effect does not precede the cause, leads to the functional form for $D(t)$.

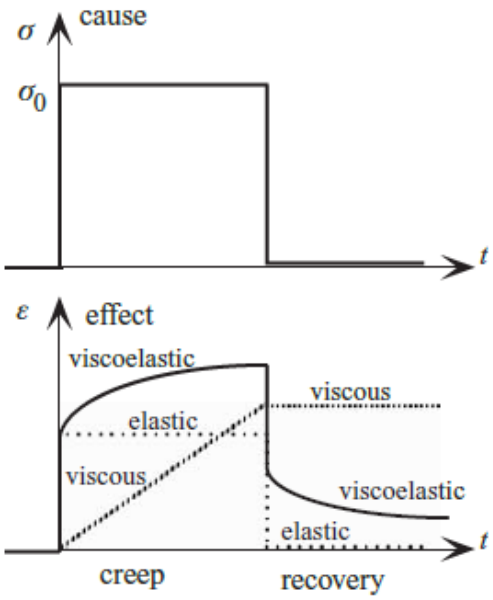

Figure 2.11 Creep and recovery. Stress σ and strain ε versus time t. Elastic aftereffect is included (Lakes, 2009)

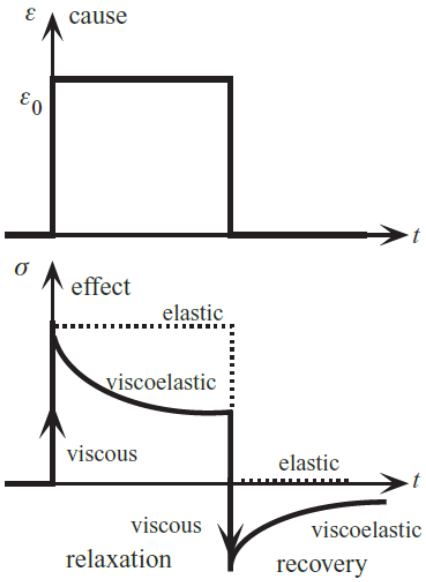

Figure 2.12 Stress relaxation and recovery (Lakes, 2009)

In a stress relaxation test, the stress gradually decreases while the strain is held constant at ε_0. Thus, for a strain history:

$$\varepsilon(t) = \varepsilon_0 H(t) \tag{2.22}$$

the stress in a viscoelastic material will decrease with the ratio:

$$E(t) = \frac{\sigma(t)}{\varepsilon_0} \tag{2.23}$$

where $E(t)$ is called the relaxation modulus. For linear materials, this ratio is independent of the strain level, thus, $E(t)$ is a function of time alone. Figure 2.12 shows a stress relaxation test and the recovery phase.

2.2.4.2. Prediction of recovery from relaxation $E(t)$

The creep and relaxation tests describe the response of the material under a step signal. For the response to any stress or strain history, the Boltzmann superposition principle is used where the effect of a combination of causes is the summation of individual causes. Therefore, first the recovery response, following the removal of the stress or strain, is elaborated on.

The removal of the stress or strain can be mathematically defined by a *unit box function.* This function is described in terms of Heaviside functions below. The response of a material to an arbitrary load or strain history is required. The *constitutive equations* incorporate all possible responses.

For an arbitrary time at which a jump occurs the Heaviside function can be described as:

$$H(t-a) = \begin{cases} 0, t < a \\ 1, t > a \end{cases} \tag{2.24}$$

The Heaviside function can be used to describe a box function $u(t)$ by superposition of a step up at time a followed by a step down at time b:

$$H_{ab}(t) = \begin{cases} 0, & t < a \\ 1, & a < t < b \\ 0, & t > b \end{cases} \tag{2.25}$$

And expressed in Heaviside functions:

$$H_{ab}(t) = H(t-a) - H(t-b) \tag{2.26}$$

Thus, for an assumed strain history of ε_0 from $t = 0$ until $t = t_1$ may be written as:

$$\varepsilon(t) = \varepsilon_0[H(t) - H(t-t_1)] \tag{2.27}$$

The response, from the Boltzmann superposition principle is as shown Figure 2.11,

$$\sigma(t) = \varepsilon_0[E(t) - E(t-t_1)] \tag{2.28}$$

2.2.5. Prediction of response to arbitrary strain history

For a stress relaxation test the strain response is thus $\sigma(t) = M(t)H(t)$. Recovery, the response following the removal of the strain, leads to a step down in the strain. For a stress relaxation where the constant strain is ε_0 at $t = 0$ and the strain is removed at $t = \tau$ described as:

$$\varepsilon(t) = \varepsilon_0[H(t) - H(t-t_1) \tag{2.29}$$

The stress response is:

$$\sigma(t) = \varepsilon_0[E(t) - E(t-t_1)] \tag{2.30}$$

Now for an arbitrary strain history the response to a time segment can be computed. The segment runs from $t-\tau$ to time $t-\tau+\Delta t$, where τ is the same as t_1. This segment of strain history can be written as:

$$\varepsilon(t) = \varepsilon(\tau)[H(t-\tau) - H(t-\tau+\Delta\tau]$$

The change in stress at time t due to the strain pulse is:

$$d\sigma(t) = \varepsilon(\tau)[E(t-\tau) - E(t-\tau+\Delta\tau)] \tag{2.31}$$

Since $\frac{dE(t-\tau)}{d\tau} = \lim_{\Delta\tau\to 0}[E(t-\tau) - E(t-\tau+\Delta\tau)]$ and the entire strain history can be decomposed in these pulses the stress at any time t is the sum of the effects of these pulses. Due to causality principle, only the influence of the pulses before the present time are included. With the limit applied the summation of the stress responses converges to an integral, the Boltzmann superposition integral:

$$\sigma(t) = \int_{-\infty}^{t} E(t-\tau)\frac{d\varepsilon(t)}{d\tau}d\tau \tag{2.32}$$

and similarly, for a given stress history the strain response is:

$$\varepsilon(t) = \int_{-\infty}^{t} D(t-\tau)\frac{d\sigma(t)}{d\tau}d\tau \tag{2.33}$$

These integrals are considered the mathematical description of linear viscoelastic behaviour. They can be used to derive the dynamic functions.

2.2.6. Dynamic response functions

The response of a viscoelastic material to a sinusoidal load is referred to as *dynamic*. The dynamic behaviour of saline ice is of interest in this work. The oscillatory stress and strain histories are represented by sinusoid functions. For example, a stress history denotes as:

$$\sigma(t) = \sigma_0 \sin(\omega t) \tag{2.34}$$

in which σ_0 is the amplitude, ω is the angular frequency and t is time. Since the sine function repeats every 2π radians, the time required to complete a cycle is obtained from $\omega T = 2\pi$, where T is the *period* ($T = 2\pi/\omega$). The inverse of the period, the number of cycles per second (or Hertz) is called the *frequency* denoted as f. Similarly, a cyclic strain history is represented as:

$$\varepsilon(t) = \varepsilon_0 \sin(\omega t) \tag{2.35}$$

where ε_0 is the strain amplitude.

In a viscoelastic material, stress and strain have the same period, but may be out of phase. The representation of the phase shift is through the *phase angle* ϕ. Thus, for a sinusoid $\sin(\omega t)$ the phase shifted sinusoid is $\sin(\omega t + \phi)$. A different notation of the sinusoidal functions is the *complex exponential notation* with a history defined as $\exp(i\omega t)$ and a response of $\exp(i(\omega t - \phi))$.

2.2.6.1. Phase lag and amplitude

The dynamic response functions can be derived from the requirement of linearity of the stress-strain relations. If a stress, periodic in time, is imposed on the system, the phase lag and amplitude of the strain behind the stress is determined. The stress is written as:

$$\sigma(t) = \sigma_0 \exp(i\omega t) \tag{2.36}$$

where

$$\varepsilon(t) = \varepsilon_0 \exp(i(\omega t - \phi)) \tag{2.37}$$

ratio $\varepsilon(t)/\sigma(t)$ is a complex quantity, which is now called *dynamic compliance* $D^*(\omega)$, also known as the *frequency response function*, with dynamic referring to the sinusoidal load and compliance to the ratio between the strain and the stress. For an ideal elastic material, the ratio ε_0/σ_0 gives the elastic compliance D. For a purely viscous material the phase angle is $\pi/2$ and the ratio ε_0/σ_0 gives the viscosity. However, for a viscoelastic material, the ϕ is neither zero nor $\pi/2$, such that the ratio is a complex quantity called the *complex compliance* or *dynamic compliance* $D^*(\omega)$, a function of ω, thus,

$$D^*(\omega) \equiv \frac{\varepsilon(t)}{\sigma(t)} = |D|(\omega) \exp(-i\phi(\omega) \tag{2.38}$$

Where $|D|(\omega) = \varepsilon_0/\sigma_0$ is the *absolute dynamic compliance.*

2.2.6.2. In-phase and out-of-phase component

Rewriting the strain response in Equation (2.37) gives:

$$\varepsilon(t) = (\varepsilon_1 - i\varepsilon_2) \exp(i\omega t) \tag{2.39}$$

where ε_1 is the amplitude of the component of ε_1 in phase with the stress and ε_2 the component out-of-phase. The ratio $\sigma(t)/\varepsilon(t)$ is now calculated and two new terms are introduced:

$$\varepsilon_1 = \varepsilon_0 \cos\phi \tag{2.40}$$

$$\varepsilon_2 = \varepsilon_0 \sin\phi \tag{2.41}$$

$$D^*(\omega) \equiv \frac{\varepsilon(t)}{\sigma(t)} = \frac{\varepsilon_1}{\sigma_0} - i\frac{\varepsilon_2}{\sigma_0} = D_1(\omega) - iD_2(\omega) \tag{2.42}$$

Where $D_1(\omega)$ is called the storage compliance and $D_2(\omega)$ is the loss compliance for reasons later explained. The two equations for the dynamic compliance in Equation and Equation are equivalent for the following properties of the compliances:

$$D_1(\omega) = |D| \cos(\phi) \tag{2.43}$$

$$D_2(\omega) = |D| \sin(\phi) \tag{2.44}$$

The relationship between the different forms is given below:

$$|D|^2 = D_1^2 + D_2^2 \tag{2.45}$$

$$\tan \phi = D_2/D_1 \tag{2.46}$$

$$\cos \phi = D_1/|D| \tag{2.47}$$

$$\sin \phi = D2/|D| \tag{2.48}$$

A visual representation of the parameters above is given in Figure 2.13.

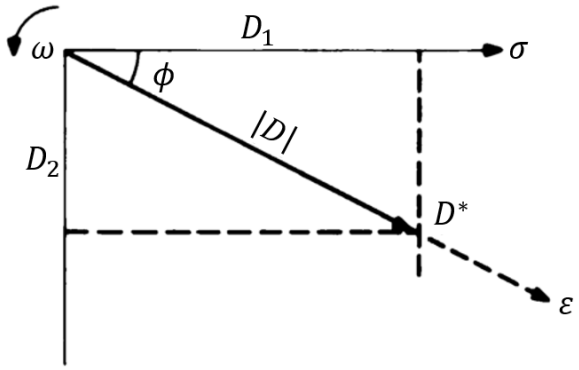

Figure 2.13 The phase relationships between the stress, strain and complex compliance. (Nowick and Berry, 1972)

and the strain response to a stress history is:

$$\varepsilon(t) = \sigma_0(D_1 \sin(\omega t) - D_2 \cos(\omega t)) \tag{2.49}$$

or in complex notation

$$\varepsilon(t) = \sigma_0(D_1 - iD_2) \exp(i\omega t) \tag{2.50}$$

In a similar way for moduli:

$$M^*(\omega) \equiv \frac{\sigma}{\varepsilon} = |M|(\omega) \exp(i\phi(\omega)) \tag{2.51}$$

$$M^*(\omega) \equiv \frac{\sigma}{\varepsilon} = M_1(\omega) + iM_2(\omega) \tag{2.52}$$

Thus the complex compliance $D^*(\omega)$ and $M^*(\omega)$ are reciprocals:

$$M^*(\omega) = [D^*(\omega)]^{-1} \qquad |M|(\omega) = [|D|(\omega)]^{-1} \tag{2.53}$$

2.2.6.3. Dynamic response derivation

Properties of dynamic functions can be derived from the stress history:

$$\sigma = \sigma_0 \exp(i\omega t) \tag{2.54}$$

using the Boltzman superposition integral:

$$\varepsilon(t) = \int_{-\infty}^{t} D(t-\tau)\frac{d\sigma(\tau)}{d\tau}\,d\tau \tag{2.55}$$

The creep function, $D(t)$ is decomposed into the instantaneous modulus, or unrelaxed compliance D_U and the equilibrium compliance $\widehat{D}(t) = D(t) - D(\infty)$.

$$D(t) = D_U + \widehat{D}(t) \tag{2.56}$$

The stress history is substituted in the Boltzmann superposition integral and the decomposed creep functions:

$$\varepsilon(t) = D_U\sigma_0 \exp(i\omega t) + i\omega\sigma_0 \int_{-\infty}^{t} \widehat{D}(t-\tau)\exp(i\omega t)\,d\tau \tag{2.57}$$

A new time variable $t' = t - \tau$ is substituted and Eulers formula is applied leading to:

$$\begin{aligned}\varepsilon(t) = \sigma_0 \exp(i\omega t)\Bigg(D_U + \omega\int_0^{\infty}\widehat{D}(t')\sin(\omega t')dt' + \\ + i\omega\int_0^{\infty}\widehat{D}(t')\cos(\omega t')\,dt'\Bigg)\end{aligned} \tag{2.58}$$

Thus, if the stress is sinusoidal in time the strain is as well, but they are no longer in phase. If we choose to rewrite the stress strain relationship $\varepsilon(t)$ as:

$$\varepsilon(t) = D^*(\omega)\sigma(t) = (D_1 + iD_2)\sigma(t) \tag{2.59}$$

we find D_1 and D_2 as:

$$D_1(\omega) = \Re\big(D^*(\omega)\big) = D_U + \omega\int_0^{\infty}\widehat{D}(t')\sin(\omega t')dt' \tag{2.60}$$

$$D_2(\omega) = \Im(D^*(\omega) = \omega\int_0^{\infty}\widehat{D}(t')\cos(\omega t')\,dt' \tag{2.61}$$

2.2.6.4. Interrelation between storage and loss compliance

A relation between the storage and loss compliance is proposed by Kronig and Kramer and known as the Kramers-Kronig relations (Lakes, 2009):

$$D_1(\omega) - D_U = \frac{2}{\pi}\int_0^{\infty} D_2(\alpha)\frac{\alpha d\alpha}{\alpha^2 - \omega^2} \tag{2.62}$$

and

$$D_2(\omega) = \frac{2\omega}{\pi}\int_0^{\omega}[D_1(\alpha) - D_U]\frac{d\alpha}{\omega^2 - \alpha^2} \tag{2.63}$$

2.2.7. Stress-strain curves of dynamic experiments

The relation between $\sigma(t)$ and $\varepsilon(t)$, based on a strain history of $\varepsilon(t) = \varepsilon_0 \sin(\omega t)$ and a stress response of $\sigma(t) = \varepsilon_0(E_1 \sin(\omega t) + E_2 \cos(\omega t)$, is represented by an ellipse equation (Irgens, 2008). The strain history and stress response are changed to:

$$E_2\varepsilon(t) = E_2\varepsilon_0 \sin(\omega t)\,, (\sigma(t) - E_1) = E_2\varepsilon(t) \tag{2.64}$$

When the two equations are squared and summed up the following ellipse equation is the result:

$$(\sigma(t) - E_1\varepsilon(t))^2 + (E_2\varepsilon(t))^2 = (E_2\varepsilon_0)^2 \tag{2.65}$$

The resulting curve is presented in Figure 2.14. The area inside the curve represents the dissipation of mechanical energy per unit volume and during one period. The width at the mean stress, $D_2\varepsilon_0$, and the height at the mean strain are equivalent to the energy dissipation. The following relations are used to calculate the loss compliance and storage from the loops.

$$height = E_2\varepsilon_0 \tag{2.66}$$

$$width = D_2\sigma_0 \tag{2.67}$$

And the equations for the loss and storage compliance are:

$$D_1 = \frac{\varepsilon_0}{\sigma_0}\cos\phi = \frac{\varepsilon_0}{\sigma_0}\frac{E_1}{|E|} \tag{2.68}$$

$$D_2 = \frac{\varepsilon_0}{\sigma_0}\sin\phi = \frac{\varepsilon_0}{\sigma_0}\frac{E_2}{|E|} \tag{2.69}$$

The loop width, height and amplitudes and equations are displayed in Figure 2.14.

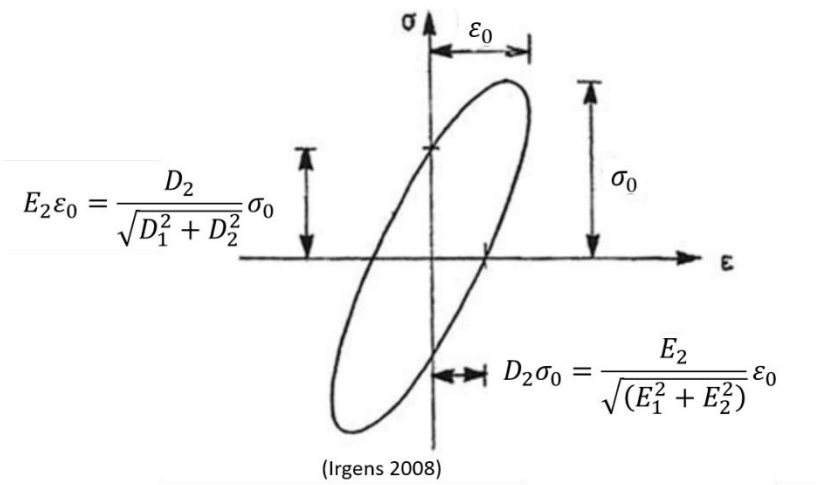

Figure 2.14 Stress-strain curve (Irgens, 2008)

2.3. Model of saline ice subjected to cyclic loading

The constitutive behaviour of saline ice was shown to be composed of largely elastic and anelastic components by Cole and Durell (1995). For the high levels of anelasticity a model was developed by Cole (1995) to completely describe the anelastic component of strain when a cyclic stress is applied. The dominant deformation mechanisms in the regime where creep occurs, but without microcracking, are the dislocation relaxations and grain boundary relaxations. The influence of the dislocation relaxation is largest for the frequency range of interest in this study (Cole and Durell, 1995). Therefore, this study focusses on the dislocation relaxations.

Dislocation science of metals have received a lot of attention. Since the 1970s some of this knowledge is applied to ice by Weertman, Traetteberg, Duval and others. First the single crystals were researched and then also polycrystalline ice. For saline water the first efforts into a physics based model for the anelastic straining was made by Cole (1991).

2.3.1. Grain boundary anelasticity

Grain boundary anelasticity was observed in laboratory prepared fresh water ice and saline ice (Cole and Durell, 1995) and in field obtained glacier cores . The associated internal friction peak occurs under a 1 Hz forced oscillation, thus for this frequency the anelasticity is most notable. The grain size seems to affect the internal friction. Using dynamic experiments, this peak was not shown for single grain experiments, thus it was concluded the relaxation peak occurs at grain boundaries (Nakamure and Abe, 1979).

2.3.2. Dislocation-based anelasticity

Creep recovery tests showed a large anelastic component in the strain response of fresh-water polycrystalline ice, with the ratio of anelastic to elastic strain ranging from 10 (Cole 1991) to 60 (Duval, 1978). The rise of the internal friction, causing an anelastic component, of fresh-water single crystals was linked by Vaissoille, Mai and Perez (1978) to the increase of the measured dislocation density. The experiments of Cole and Durell (1995) quantified the activation energy, a measure for the threshold energy to engage a of groups of dislocations to influence the anelastic behaviour.

A method to quickly identify the anelastic component is by applying a cyclic load and measuring the strain. The observations of these experiments showed that the activation energy of the process in saline and fresh water ice are approximately the same.

2.3.3. Dislocations under quasi-static stress conditions

From dislocation mechanics, it is known that the total strain, ε^d in a single grain due to displacement of the dislocation depends on the orientation factor, which relates the displacement direction compared to the microstructure of the specimen:

$$\varepsilon^d = \rho \Omega b x^d \; [-] \tag{2.70}$$

where ρ is the mobile dislocation density in reciprocal square meters, Ω is an orientation factor that converts the background normal stress to the average resolved shear stress on the basal plane ($\Omega = 1/\pi \approx 0.32$ for a horizontal specimen from S2 ice), b is the magnitude of the Burgers vector (4.52×10^{-10} m). The Burgers vector represents both the direction and length of a dislocation, as shown in Figure 2.6. The distance, x^d travelled by one dislocation under a quasi-static stress σ is:

$$x^d = \frac{b}{K}\sigma \tag{2.71}$$

where K is the restoring stress constant (0.07 Pa). The strain in Equation (2.70) with Equation (2.71) substituted can be divided by the quasi-static stress, which results in:

$$\frac{\varepsilon^d}{\sigma} = \frac{\rho \Omega b^2}{K} = \delta D^d \tag{2.72}$$

where δD^d is called the strength of the dislocation relaxation and is later used in the derivation of the response to a cyclic loading (Cole, 1995).

2.3.4. Motion of dislocation under sinusoidal stress

The movement of dislocations from one low energy position to another was described by Nowick and Berry (1972) as a hysteresis phenomenon, the dependence of the state of the system on its history. An analytical expression for the oscillation of a dislocation in ice is developed by Cole and Durell (1995). This expression is similar to the works of Weertman, (1955) for metal single crystals of Kressel and Brown, (1967) for lattice defects in nickel. Joncich, (1976) links the formulas of Weertman to dislocations in predeformed ice.

The oscillation of the dislocation under a certain applied stress, subjected to lattice drag and a restoring stress component is expressed as:

$$B\dot{x} + Kx = b\sigma_0 \sin(\omega t) \tag{2.73}$$

where x is the displacement of one dislocation (superscript d is not included for readability), C the temperature dependent dislocation drag (i.e. damping), K is the restoring stress acting in opposition to the dislocation (i.e. stiffness), b is the Burgers vector, σ_0 is the maximum cyclic shear stress resolved on the slip plane (with the subscript 0 denoting an amplitude), ω is the angular frequency and t is the time (Cole, 1995).

The drag term B was estimated from the velocity of dislocations determined by Whitworth (1978) . An estimate of temperature dependence of the drag term B is

$$B = B(T) = B_0 \exp\left(\frac{Q}{kT}\right) \text{ [s}^{-1}\text{]} \tag{2.74}$$

With k is the Boltzmann constant ($8{,}617\,343 \times 10^{-5}$ eV/K), and the activation energy Q [eV] and the term B_0 [Pa s] derived from experiments on single ice crystals. This equation pertains to basal slip in pure ice and is expected to be independent of the microstructure (Cole, 1995). For dislocation relaxation the values of $B_0 = 1.205 \times 10^{-9}$ Pa s and $Q = 0.55$ eV are used.

This drag term is relates to basal slip in pure ice and is independent of the microstructure. It is dependent of the temperature and the activation energy of the mechanism:

The restoring stress term K, which relates the stress to the displacement, lumps together the effects of several physical processes: dislocation-dislocation interactions, dislocation-obstacle interactions, elastic anisotropy and line tension. An independent assessment of K is not possible, but can be found from an experimental campaign, which the following section describes.

The solution to the homogeneous solution $B\dot{x} + Kx = 0$, may be be derived as:

$$x_h(t) = Xe^{-\frac{K}{C}t} \tag{2.75}$$

For the derivation of particular solution Equation (2.73) is rewritten as:

$$\dot{x} + \frac{K}{B}x = \frac{b\sigma_0}{B}\sin(\omega t) \tag{2.76}$$

and a particular solution of the form assumed as:

$$\begin{aligned} x_p(t) &= X_C\cos(\omega t) + X_S\sin(\omega t) \\ \dot{x}(t) &= -\omega X_C\sin(\omega t) + \omega X_S\cos(\omega t) \end{aligned} \tag{2.77}$$

in which X_C and X_S are constants, multipliers of respectively the cosine and sine function (as denoted with the subscripts). The particular solution represents the steady forced vibrations. To determine these constants, equation (2.77) is substituted in the differential equation (2.76), leading to:

$$X_C = -\frac{b\sigma_0}{K^2 + B^2\omega^2}B\omega \tag{2.78}$$

and

$$X_S = \frac{b\sigma_0}{K^2 + B^2\omega^2}K \tag{2.79}$$

The general solution of Equation (2.76), is the sum of the solution of the homogeneous equation and the particular solution:

$$x(t) = x_h(t) + x_p(t) \tag{2.80}$$

which results in:

$$x(t) = Xe^{-\frac{K}{B}t} + \frac{b\sigma_0}{K^2 + B^2\omega^2}(K\sin(\omega t) - B\omega\cos(\omega t)) \tag{2.81}$$

The initial conditions of $x = 0$ at $t = 0$ give:

$$X = \frac{b\sigma_0}{K^2 + B^2\omega^2}B\omega \tag{2.82}$$

In Equation (2.81), the first term is the transient term due to the homogeneous equation, thus, a property of the system and the second term the steady-state term due to the particular solution, thus, to the load applied. The steady-state term consists of a sine and cosine function, of which the coefficients are respectively proportional to the stiffness and the dampening of the system. The cosine coefficient, X_c, when plotted as a function of ω describes a peak. The frequency at which the peak occurs, i.e. the central frequency, depends on the ratio between K and B. Two peaks for two trivial ratios between K and B are plotted in Figure 2.15.

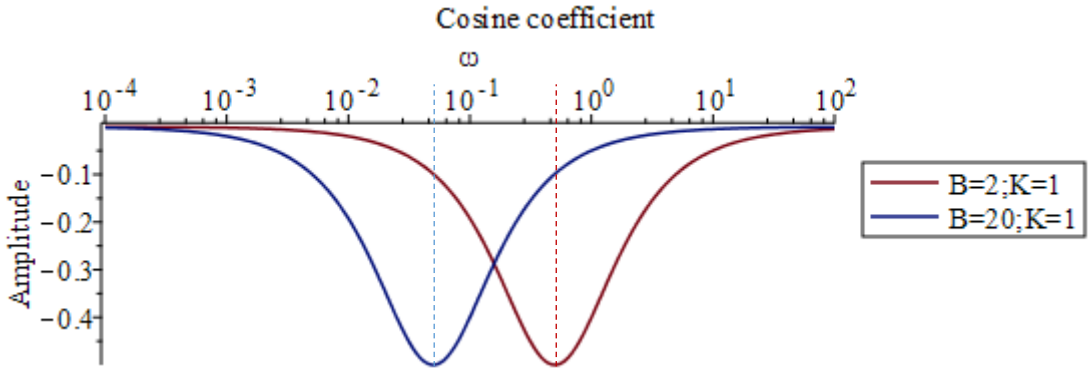

Figure 2.15 Two peaks for two combinations of B and K. The central frequency of the left peak equals $\omega_0 = \frac{K}{B} = \frac{1}{20} = 5 \times 10^{-2}$ rad/s and of the right peak $\omega_0 = \frac{K}{B} = \frac{1}{2} = 5 \times 10^{-1}$ rad/s

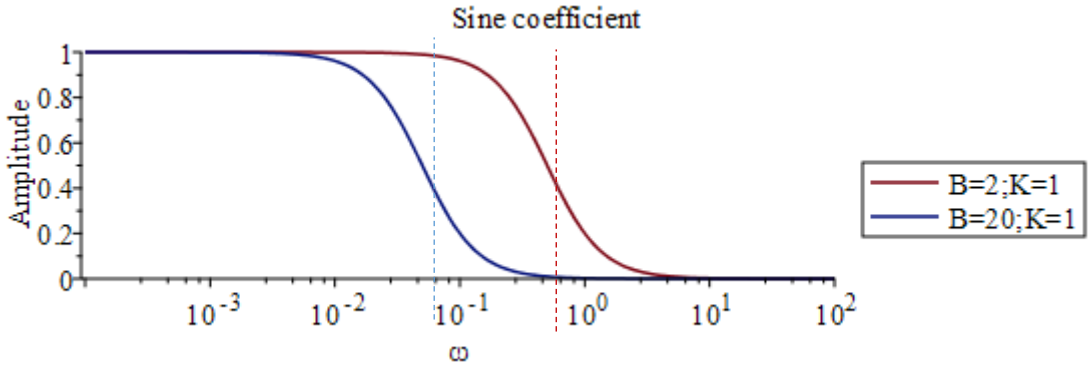

Figure 2.16 Two sine coefficients for two combinations of B and K.

The ratio between K and B can be expressed as the relaxation time $\tau = B/K$, which is compliant to the central frequency of the peak. For clarity, the sine coefficient is plotted in Figure 2.16 and the stress-displacement curves of the central frequency of the right-hand peak for both ratios are plotted in Figure 2.17. The stress signal given is $\sigma = \sin(\omega t)$, the resulting displacements are described as: $x = 0.5\sin(\omega t) - 0.5\cos(\omega t)$ and $x = -0.1\cos(\omega t)$. The following remarks can be made:

- For frequencies, much lower than the central frequency, damping of system has a very small influence and the steady-state response is in-phase
- For the central frequency, the loop width of the stress-strain curve is the largest
- For frequencies above the central frequency the phase difference is 90° and has a smaller amplitude.

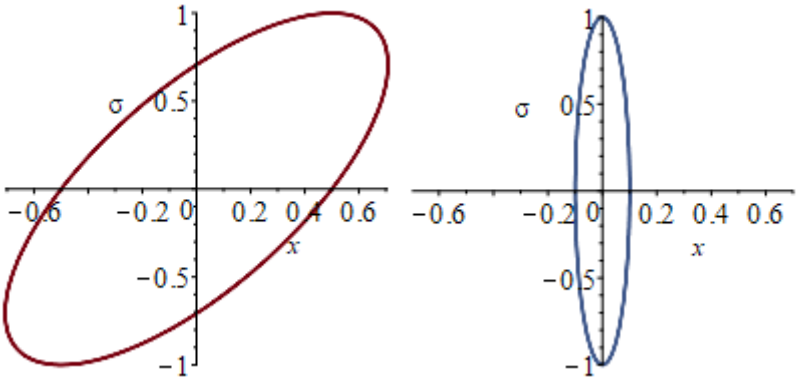

Figure 2.17 Stress-displacement curves for central frequency of the right-hand peak of the cosine coefficient

Substitution of the relaxation time into Equations (2.81) and (2.82) leads to:

$$x = X \exp\left(-\frac{t}{\tau}\right) + \frac{b\sigma}{K}\frac{(\sin(\omega t) - \tau\omega\cos(\omega t))}{1 + (\tau\omega)^2} \tag{2.83}$$

$$X = \frac{b\sigma}{K}\frac{\tau\omega}{1 + (\tau\omega)^2} \tag{2.84}$$

where $\tau\omega/(1 + (\tau\omega)^2$, the so-called Debye term, can be recognized in the transient term and the cosine coefficient, which will prove useful later.

The term $b\sigma/K$ can be also recognized, which was used in Equation (2.72) to relate the motion of a dislocation under a quasi-static stress to the strain, through the dislocation density. An interim expression for the steady-state strain response in an ice specimen, due to cyclic loading, with Equation (2.72) substituted in equation (2.83) leads is:

$$\begin{aligned}\varepsilon_{d,interim} &= \rho\Omega b\frac{b\sigma}{K}\frac{(\sin(\omega t) - \tau\omega\cos(\omega t))}{1 + (\tau\omega)^2} \\ &= \delta D\frac{(\sin(\omega t) - \tau\omega\cos(\omega t))}{1 + (\tau\omega)^2}\end{aligned} \tag{2.85}$$

Provided that B is found from independent experiments and the central frequency of the relaxation peak is found through the cyclic experimental campaign, K can be found subsequently. The experimental campaign by Cole and Durell (1995) found a value for K of 0.07, from the central frequency of their loss compliance found in the experiments.

2.3.5. Aggregate behaviour of dislocations in a large number of grains and loss compliance

With the above derived equations for the dislocation relaxation in a single grain and grain boundary, the polycrystalline material behaviour is not yet completely described, apart from the central relaxation frequency. The material consists of a large number of grains that are all physically attached to each other and interact with each other in the specimen. This is referred

to as a coupled relaxation problem, the relaxation of each grain is influenced by the speed of its neighbours. The loss function derived in Equation (2.78) arrives at the so-called Debye relaxation, which employs a single relaxation time. To account for the relaxation time of each grain and thereby find a loss compliance that reflect the experimental observations a peak broadening term α^d is introduced (Cole, 1995). A similar approach is used by Lakki *et al.* (1993) to model the internal friction of another polycrystallic material. The peak broadened, is the loss compliance as described by Equation (2.78). The term is used by replacing the Debye term, $\tau\omega/(1+(\tau\omega)^2)$ in Equation (2.78) with:

$$\frac{\alpha}{2}\operatorname{sech}(\alpha\ln(\tau\omega)) = \frac{\alpha}{2}\cdot\frac{2}{\exp\alpha\ln(\tau\omega)+\exp(-\alpha\ln(\tau\omega))} \tag{2.86}$$

The peak broadening effect of α^d is shown in Figure 2.18. For a value of $\alpha^d = 1$, Equation (2.86) reduces to the Debye term. However, for a lower value of α^d, the integral value of the function remains the same, but the described peak broadens hence α^d is called the peak broadening term.

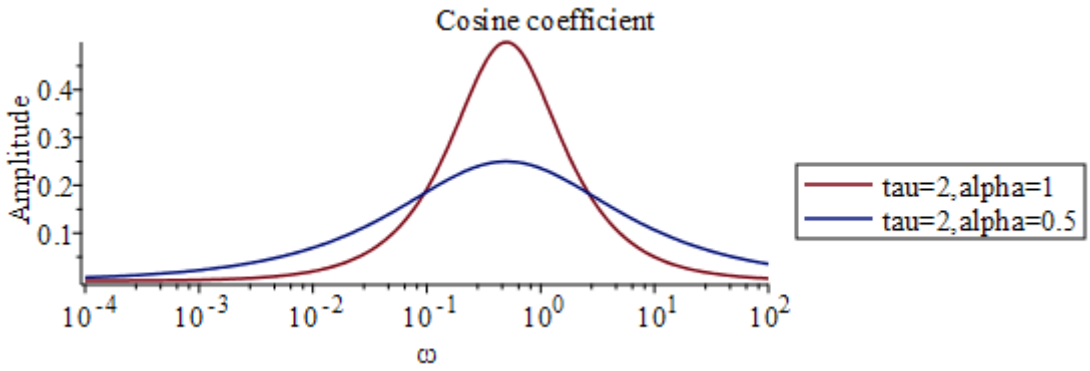

Figure 2.18 The cosine coefficients, described by Equation (2.78) and Equation (2.79)

When the above described replacement of the Debye term, or peak broadening is applied to Equation (2.78), the cosine coefficient of the steady-state strain due to the dislocation relaxation D_2^d, or loss compliance due to dislocation relaxation, is:

$$D_2^d = \alpha^d\delta D^d\frac{1}{\exp(\alpha^d s)+\exp(-\alpha^d s)} \tag{2.87}$$

Where α^d is the peak broadening factor, found from experiments, $s = \ln(\tau^d\omega)$ and δD^d sets the magnitude of the dislocation relaxation.

To find the value of α^d Equation (2.87) is compared to the loss compliance as function of ω found in the experiments by Cole and Durell (1995). The value of α resulted from a least-

square analysis. An example of this analysis is shown in Figure 2.19 where $\delta D^d = 1.4 \times 10^{-9}$ Pa^{-1}, $\alpha^d = 0.53$ $K^d = 0.07$ Pa.

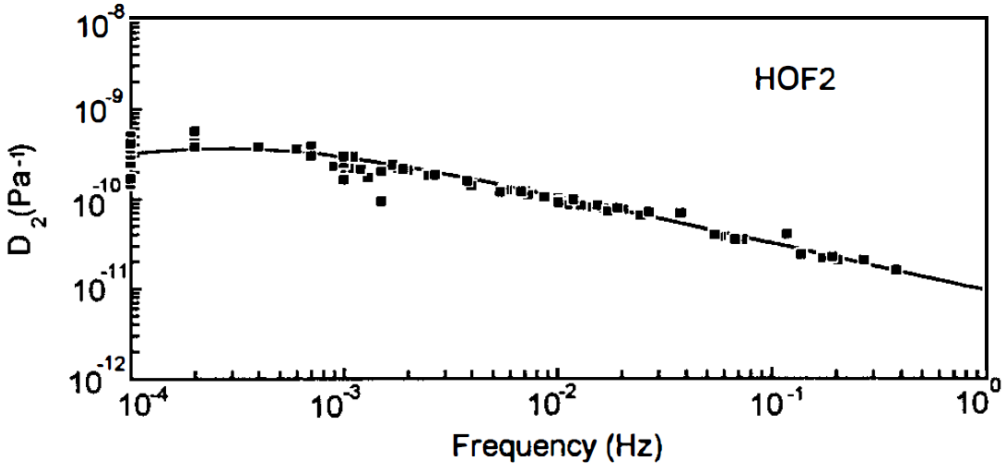

Figure 2.19 Loss compliance as function of frequency including data points (Cole, 1995)

The equation for the loss compliance takes the polycrystalline material into account. As described in Section 2.2.6.3, the loss compliance is only the imaginary part of the complex compliance, $D^*(\omega) = D_1(\omega) - iD_2(\omega)$. The storage compliance for an anelastic solid can be derived from the loss compliance, using the Kramers-Kronig relations, as shown in section 2.2.6.4. These relations were employed in (Cole, 1995) to obtain the following storage compliance:

$$D_1^d(\omega) = D_U^d + \frac{2}{\pi}\int_{\ln(\tau\omega)}^{+\infty} D_2^d \, d[\ln(\tau^d\omega)] \tag{2.88}$$

$$D_1^d(\omega) = D_u^d + \delta D^d\left(1 - \frac{2}{\pi}\tan^{-1}[\exp(\alpha^d \ln(\tau^d\omega))]\right), \tag{2.89}$$

Where D_U^d is the unrelaxed compliance of the elastic modulus, a value of 9.0 GPa is employed for ice. The contribution of D_1^d relates to the steady-state response proportional to the total amount of stiffness in the material.

2.3.6. Loss and storage compliance

The above derivation lead to the loss and storage compliance of the dislocation relaxation. The grain boundary relaxation is implemented as well and both relaxation mechanisms are expected to operate simultaneously, so $D_1 = D_1^d + D_1^{gb}$ and $D_2 = D_2^d + D_2^{gb}$ where:

$$\begin{aligned} D_1^d(\omega) &= D_u^d + \delta D^d\left(1 - \frac{2}{\pi}\tan^{-1}[\exp(\alpha^d s^d)]\right), \\ D_1^{gb}(\omega) &= D_u^{gb} + \delta D^{gb}\left(1 - \frac{2}{\pi}\tan^{-1}[\exp(\alpha^{gb} s^{gb})]\right), \end{aligned} \tag{2.90}$$

$$D_2^d(\omega) = \alpha^d \delta D^d \frac{1}{\exp(\alpha^d s^d) + \exp(-\alpha^d s^d)}$$
$$D_2^{gb}(\omega) = \alpha^{gb} \delta D^{gb} \frac{1}{\exp(\alpha^{gb} s^{gb}) + \exp(-\alpha^{gb} s^{gb})}$$

where $s^{gb} = \ln(\tau^{gb}\omega)$, α^{gb} is the peak broadening term of the grain boundary relaxation, δD^{gb} is the relaxation strength of the grain boundary relaxation. D_U^{gb} is the unrelaxed compliance of the elastic modulus, shown here so that the derivation is correct in case only grain boundary relaxation occurs. However, in the model, this contribution can be accounted for only once.

The storage and loss compliance are used for the steady-state strain response, ε:

$$\varepsilon = \sigma_0(D_1 \sin(\omega t) - D_2 \cos(\omega t)) \tag{2.91}$$

for a given cyclic stress history.

The values for the parameters of the grain boundary relaxation were given by (Cole, 1995). These values are used in the model of this work, but have a very small contribution since the frequencies tested are an order lower the central relaxation frequency for this mechanism. Thus, the strain related to this relaxation mechanism is small and primarily in phase with the applied stress. The pre-exponential term of the central relaxation time $\tau^{gb} = B^{gb}/K^{gb}$ was identified as 8×10^{-28}, the activation energy Q^{gb} is 1.32 eV, the peak broadening factor α^{gb} is 0.6 and δD^{gb} is 3×10^{-11} Pa^{-1}. An overview of the all equations used in the model, the parameters and implementation of these to compare the model predictions to the experiments are explained in Section 4.4.

3. Experimental methods of ice production, characterization, cyclic tests and data processing

The experiments were conducted in the Cold Laboratory at the University Centre in Svalbard, UNIS. The ice production method is based upon the experiments of Wu, Chang, & Schwarz(1976) and the experiments by Bueide (2014), which were conducted in the same cold laboratory as this study. The cyclic compression test method and test matrix were based upon the method of Cole & Durell (1995).

3.1. Ice specimen production

The specimen production is visualized in fig FF. Room temperature in the UNIS cold laboratory can be maintained within the range of $-20℃$ to $+5℃$ ($\pm 1℃$) (but below $-15℃$ the temperature was less stable ($\pm 3℃$)). Ice was grown on four occasions up to a thickness of 25 cm at minimum and 44 undamaged cores were retrieved 11 of which were drilled horizontally.

3.1.1. Production of cores

The production of horizontal and vertical cores from a laboratory grown sheet of ice is illustrated in Figure 3.1. The ice was made from a mix of ¼ filtered local sea water (retrieved from Adventfjorden, Svalbard) and ¾ tap water (retrieved from a local meltwater lake) in a 500 mm wide, 1000 mm long and 1250 mm deep, cleaned tank, see Figure 3.2. The bulk salinity of the water in the tank was approximately 8, measured with a conductivity meter (Cond 3210 SET 1 incl. Tetracon® 325 manufactured by WTW, Germany).

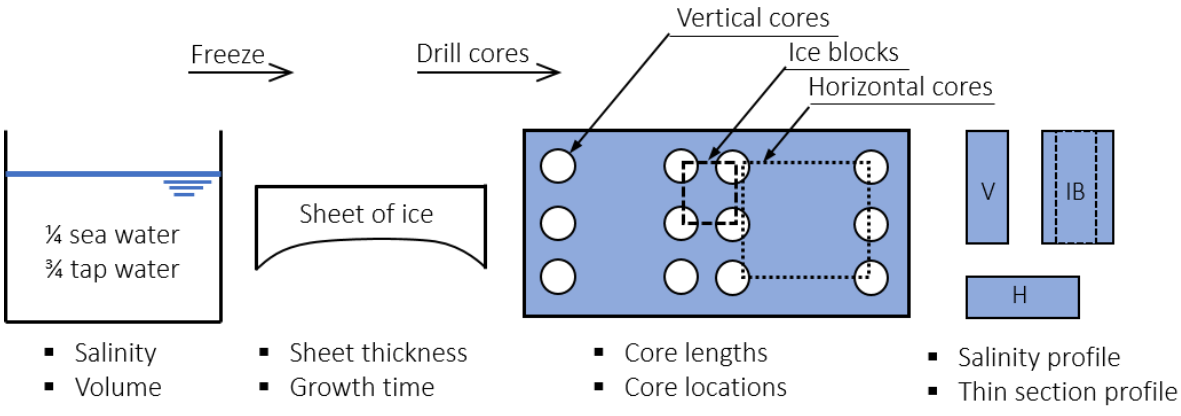

Figure 3.1 Methods for producing ice cores , resulting in horizontal (H) and vertical (V) cores

The tank is the FRYSIS, built by the Fellesverkstedet NTNU, Norway. The inside walls and floor of the tank are made of steel are insulated. To prevent ice growth from the walls, inside the steel walls and at the bottom three groups of heating cables, again two in the walls and

one in the bottom, warm the water. Three thermometers are installed in the tank walls to measure water temperature, two in the walls and one in the bottom (Myklebust, 2014). The heaters are controlled with an on-off feedback control system, located in the control room. When the temperature measured per thermometer goes below the set point, the corresponding heater is turned on. The set points were the freezing temperature of the water. The top heating element was partly exposed to air and not able to maintain the temperature.

Figure 3.2 FRYSIS tank during filling phase

The air temperature was gradually reduced from room temperature to -20 ℃. Nucleation was induced by seeding (the water-spray method), a now commonly used method to simulate natural growing conditions. All the water in the tank was regularly stirred and the temperature was measured using a handheld thermometer (the TFX 410-1 Pt1000, manufactured by Ebro, Germany) until the whole water column reached the freezing temperature, which was calculated from salinity using the UNESCO formula. The top layer of newly-formed slush was removed to clean the surface of ice and the water surface was seeded with ice crystals using a spray bottle filled with 0 ℃ distilled water. The tank was covered for 12 hours to prevent influence of the wind generated by the air conditioning units until a thin sheet of ice was formed. Afterwards the cover was removed and the sheet of ice was directly exposed to the air temperature. The room temperature varied between -20 ℃ and -15 ℃ due to the defrost cycles of the air conditioning units for 7-10 days (the air conditioning units were repaired at a later stage and the temperature was more stable afterwards). The produced ice

was later classified as S2 columnar ice by visual inspection of the thin sections produced from the sheet of ice.

Figure 3.3 Cavities in sheet of ice in tank after drilling cores

After the desired ice thickness was reached, cores were drilled using a Kovacs Mark III Coring system with an inner diameter of 7.5 cm powered by an electrical drill. To ease the start of drilling by softening the top layer the cold lab temperature was increased to -10 ℃. For the vertical cores, see Figure 3.3, a pre-cut in the surface was carved with a knife before using the core barrel to drill and take out the ice cores. The pre-cut prevented the core barrel to change the initial drilling location. The distance to the walls and the length of the vertical cores were measured with a folding rule. The ice blocks in between the outer and center vertical cores were cut out with a manual ice saw. The cut was prepared by drilling holes along the line, to ease the manual cutting. The ice block was lifted from the sheet of ice and horizontal cores were drilled in the original length direction of the tank. Subsequently, the lengths of the horizontal cores and the depths within the ice at which they were retrieved were measured. This method was also used to retrieve cores from the sea ice near Svea, Svalbard, as shown in Figure 3.4. These cores can be used to compare the response of laboratory prepared specimens to field obtained specimens, but were not used for this thesis.

All cores were photographed, wrapped in plastic foil, put into a Ziploc bag, labelled and stored in Zarges boxes in the cold storage room at UNIS (room temperature: -20℃). Lab and field observations of ice with salinities are rarely in excess of a salinity of 20 has shown to effectively exclude gravity drainage of brine (Cox and Weeks, 1986). It is therefore safe to assume that for these cores with salinities of maximum 4, gravity drainage did not occur. To further prevent brine drainage of the specimens, the horizontal cores were stored vertically and the vertical cores were stored horizontally, a method commonly applied at UNIS. All cores were named as follows:

$$IS0a - Sbb - c$$

With a indicating the sheet of ice the core originated from (IS), bb the number of the specimen (S) and c whether it was a horizontal (H) or vertical (V) specimen.

Figure 3.4 Coring system and retrieved blocks of sea ice (Svea, Svalbard) from which horizontal cores were drilled

The ice blocks in between the drill holes in the centre were cut out and used to make indicative salinity profiles and thin sections. The ice block for the salinity profile was cut in slices of 5 cm thickness with a hand saw, melted and measured with the conductivity meter. The ice blocks intended for thin sections were stored and thin sections were produced at a later stage.

3.1.2. Specimen preparation

After storage of the cores in the cold storage the specimens were prepared in the cold lab as illustrated in Figure 3.5.

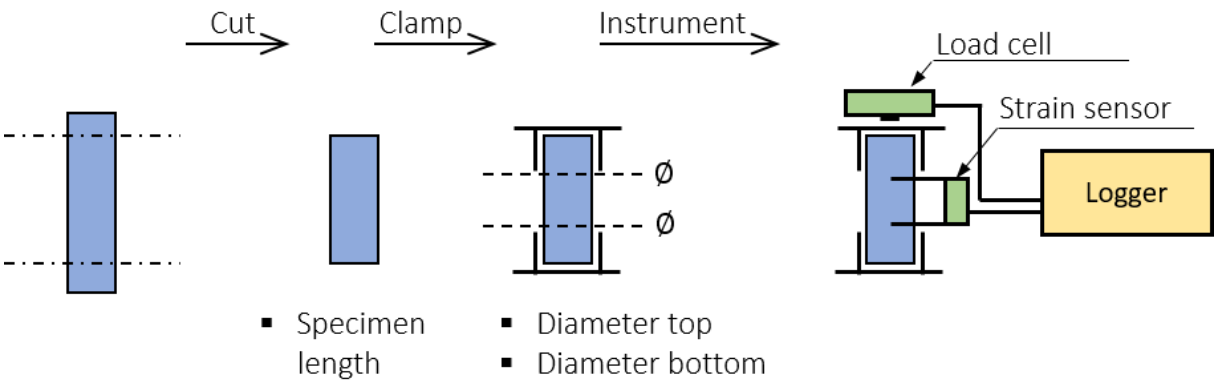

Figure 3.5 Method for preparing the instrumented ice specimens from the cores

To cut all the cores into specimens with the same length, the cores were cut in a custom saw box, see Figure 3.6. This box which employs two connected circular saws at a fixed distance (175 mm) which is operated manually by rotating a steering wheel knob connected to a flywheel.

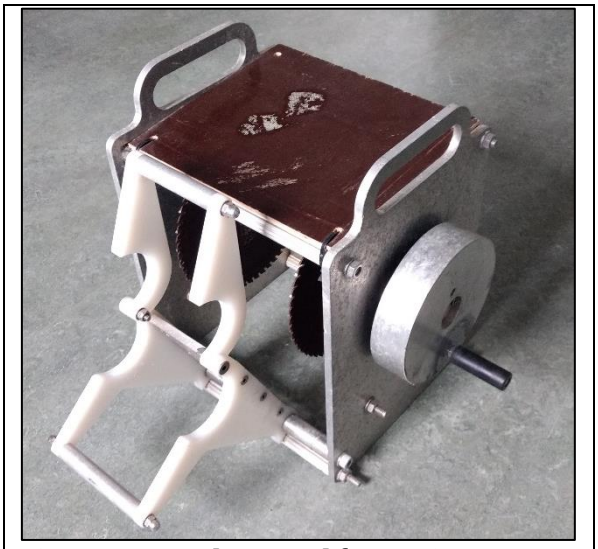

Figure 3.6 Saw box used for cutting specimens with parallel faces and normal to the longitudinal axis

The remaining top and bottom parts were used to make thin sections. Each specimen was placed into a system of custom steel clamps, see Figure 3.7, consisting of two end caps and a Teflon lined mantle (the center piece). The specimen was frozen to the clamps, by adding fresh water to each end and placing the specimen in the end cap. The mantle supports the upper end cap and aligns the specimen vertically until the specimen was fixed to the end caps. The inside height between the bottom and upper clamp, with the mantle in place, is 182 mm.

Figure 3.7 Two end caps and one mantle showing the inside of the system. During operation two mantles were applied

Upon removal from the cold storage the cores had a temperature of $-20℃$ and all compression tests were conducted at a temperature of $-10\ ℃$, so the specimens were put in the clamp system fifteen hours before the compression tests started to equilibrate to the set temperature. The mantle of the clamps was removed two hours before the cyclic compression tests. Specimens for which the compression tests lasted longer than a day were put in a plastic bag to minimize sublimation of the ice. Prior to the compression tests the diameter of the specimen below and above respectively the upper and lower end cap were measured using a caliper.

3.2. Cyclic compression tests

Five prepared specimens were used for cyclic compression tests. First, some triangular cyclic loading experiments were conducted with the field compression rig KOMPIS (built by Fellesverkstedet NTNU, Norway), a custom build mobile uni-axial compression test machine. To increase control and sensor accuracy, the laboratory loading frame, KNEKKIS (built by Fellesverkstedet NTNU, Norway) was used for the main set of experiments.

3.2.1. Triangular cyclic loading experiments

KOMPIS consists of a fixed top plate and a movable bottom plate. An electric motor, with an adjustable number of rotations per minute, moves the lower plate through a gearbox with a fixed gear ratio. The system, see Figure 3.8., is built into a metal box that allows for transportation, therefore used as a mobile compression rig.

Figure 3.8 KOMPIS , with clockwise from the specimen: draw wire sensor, control box, electrical engine, load cell and newly installed strain sensor.

The driving system is designed to compress ice cores to failure, with a length of 175 mm, at a strain rate of $10^{-3}\ s^{-1}$ (an important strain rate since it governs the transition of ductile to brittle behaviour (Schulson, 1990). A lower rate is possible, but the gear system does typically not deliver enough force to compress a specimen. The loading direction of KOMPIS is controlled by a manual switch. The three settings are moving up, not or down. The distance of the bottom to the top plate is measured with a draw-wire displacement sensor. The load is measured with a load cell in the bottom plate. The voltages of the displacement sensor and load cell are logged with an external datalogger and stored directly on an attached computer. The calibration factors for the sensors are $-0{,}05015\ mm/mV$ and $49{,}425\ kN/mV$, respectively. The maximum sampling frequency of this logger is 52 Hz.

3.2.2. Sinusoidal compression experiments

KNEKKIS is the fixed uni-axial compression machine (10 ton maximum load) with a built-in load cell in the cold lab. An external set of sensors was used for measuring the strain and load on the specimen. The fine control of the compression allows for a sinusoidal compression of the specimen.

3.2.2.1. Loading frame

KNEKKIS, shown in Figure 3.9 consists of a fixed top plate and a moveable bottom plate placed inside a frame. A stepper motor moves the bottom plate. The stepper motor can be

controlled without a feedback sensor, but a load can be used as feedback. The ratio of steps to the nominal (predicted value without other factors influencing it) displacement of the bottom plate is $7015\ steps/mm$. Due to the discrete number of motor steps the resolution of the nominal displacement, $d_{nominal}$ is $143\ nm$. Control software is written in LabView.

The stiffness of the loading frame was last tested in-house in 2013, by compressing a steel bar. Under the assumption that the steel bar was incompressible, the deformation of the frame was approximated by the curve as a function of the force F represented by eqn (3.1).

$$d_{frame} = 0.06 * F^{0.6} \tag{3.1}$$

The stiffness of this loading frame is approximately $109\ kN/mm$, which is stiffer than regular test machines used in rock mechanics (Kolari, 2016). The non-linear stiffness was discussed in the theory.

The measured parameter is the force through the load cell. The load cell, with a loading range and maximum load capacity of $100\ kN$, is located in the bottom plate and the calibration factor is $9.81\ N/V$. Both the motor steps and the load were recorded in LabView. The non-linear stiffness of the loading frame was taken into account by subtracting the frame displacement from the nominal displacement. To calculate the strain in a specimen, the initial nominal displacement at the moment of starting a test must be set to zero. Practically, this correction leads to difficulties measuring small strains. Strain in the sample was not directly measured by KNEKKIS.

Figure 3.9 KNEKKIS

3.2.2.2. External sensors

The external set of sensors include a strain sensor, the Averaging Axial Extensometer, manufactured by Epsilon technology corp, and a 10 t transducer (or load cell), manufactured by Nordisk Transducer Teknik. The datalogger, manufactured by Campbell Scientific, is built into a PeliCase 1600, manufactured by Peli Products. The software was programmed in-house using the PC200W datalogger software, by Campbell Scientific.

The strain sensor has a gauge length of 50.00 mm and a travel of +/- 6.00 mm and can be used in temperatures ranging from -40°C to 100°C. The strain sensor is mounted on a specimen and for ice specimens a drop of fresh water is used to secure the contact points of the sensor to the specimen. The contact points were on the centre line of the specimen. When the sensor is mounted the Zero Pins were removed and strain data was logged continuously. The load cell was placed on top of the specimen. The datalogger stores the signals of the sensors, battery voltage and time stamp of every record with a sampling frequency of 50 Hz, for which an hour of data can be stored on the internal memory card, before a transfer to a computer is necessary. An ice specimen placed intro KNEKKIS with installed external sensor is shown in Figure 3.10.

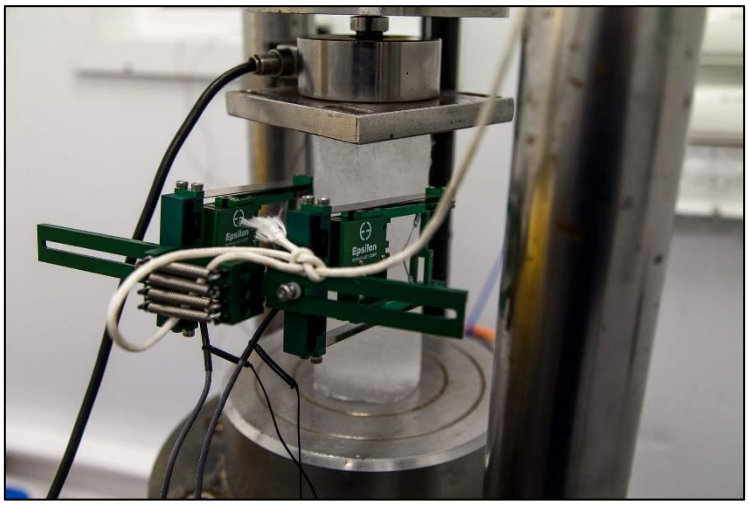

Figure 3.10 Ice specimen placed in KNEKKIS with installed strain sensor and load cell (E. Salganik)

3.2.2.3. Control of stepper engine

The control software can execute different loading profiles, or *modes*. The following modes were used:

- Manual mode: A slider defines the up- or downwards velocity of the bottom plate, ranging from -35 to 35 mm/min.
- Constant Strain Rate: The velocity of the bottom plate is defined as well as the deformation or force limit which leads to a stop of this mode or a switch to the cyclic mode.
- Cyclic mode: The peak-to-peak amplitude and the period of a cosine function are defined. The cosine function starts when the test is started ($t = 0$). The mean of the cosine function is the force limit defined plus the amplitude. This signal is then the input for the stepper engine.

For a typical cyclic experiment, consecutively the constant strain rate and cyclic mode were used. The constant strain rate and the force limit were defined after which cyclic mode was executed. An example of the stepper signal send to KNEKKIS is shown in Figure 3.11. All used experiment parameters (the test matrix) are explained in the following section. The cyclic mode developed for this experimental campaign and the performance of this system is discussed later.

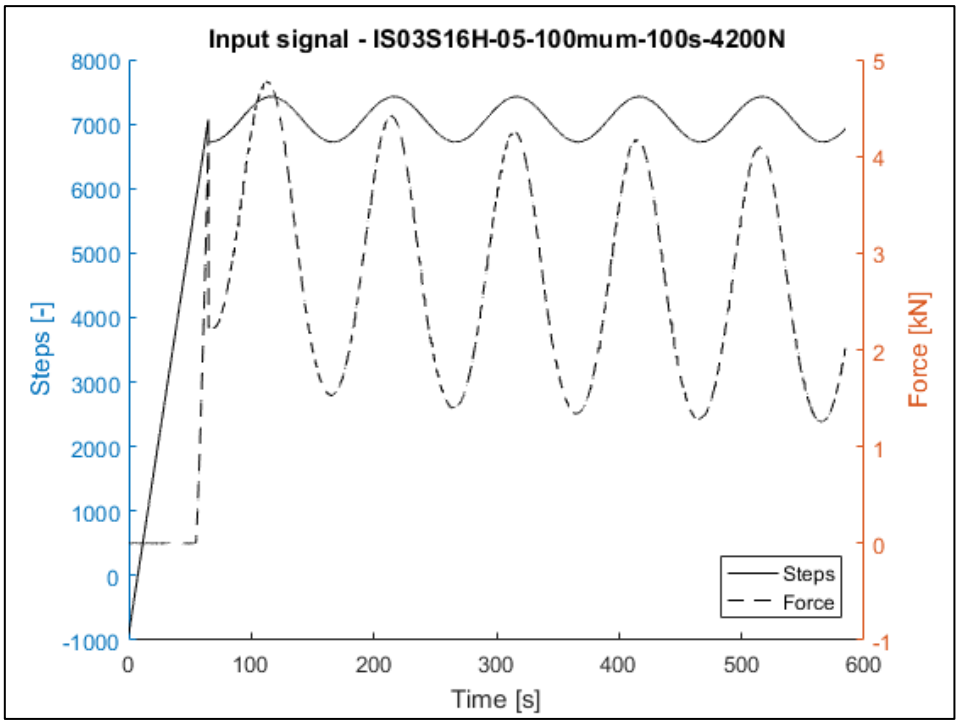

Figure 3.11 Input signal and force , the constant rate mode is the diagonal from t=0 until the force limit (4.2 kN) is reached. The cyclic mode is started subsequently with a peak to peak amplitude of 100 μm (701 steps) and a period of 100 seconds. Note the delay in the system to switch between modes.

The input signal of the cyclic mode is defined by two experiment parameters: the peak-to-peak amplitude, A_{p2p} $[\mu m]$, and the period, T $[s]$. The nominal displacement, d, of the piston as a function of these parameters is:

$$d = \frac{A_{p2p}}{2} \sin\left(\frac{2\pi t}{T}\right) \; [mm] \tag{3.2}$$

With t is time in seconds. Note that no displacement and time offset are defined. The displacement offset is defined by the initial load and the time offset depends on the time passed since movement of the plate was initiated. The velocity, $\dot{d}$, of the plate is this function is:

$$\dot{d} = \frac{\pi A_{p2p}}{T} \cos\left(\frac{2\pi t}{T}\right) \; [\frac{mm}{s}] \tag{3.3}$$

The amplitude of the velocity is the maximum velocity of the plate:

$$\dot{d}_{max} = \frac{\pi A_{p2p}}{T} \; [\frac{mm}{s}] \tag{3.4}$$

The maximum strain rate as a function of the cyclic mode parameters is:

$$\dot{\varepsilon}_{max} = \frac{\dot{d}_{max}}{L_0} \; [s^{-1}] \tag{3.5}$$

3.2.3. Experimental parameters

Two main types of experiments were conducted in KNEKKIS, mostly cyclic compression tests and a few stress-relaxation tests per specimen. Before these tests per specimen and per day were conducted the prepared specimen was placed in KNEKKIS and strain data was recorded. To measure the influence of the load cell it was placed on top of the specimen after fifteen minutes and was not removed until end of all experiments during a day. In between days (periods in which tests were performed) the load cell was removed from the specimen.

Both horizontal and vertical cores were tested. Emphasis is put onto the research on horizontal cores, due to the dislocation motion is in this direction.

Two types of cyclic tests were conducted. The regular cyclic tests, for which the frequency and amplitude were changed per test and the observation test, for a lower initial load and a fixed amplitude and period. The observation test was used to check whether the dislocation density had changed, without influencing this parameter of the ice. The constant strain rate and cyclic mode of KNEKKIS were subsequently used for each cyclic test. The constant strain rate was set to 1,05 mm/min, corresponding to a strain rate of $10^{-4}\ s^{-1}$ of the specimen. The force limit, after which the cyclic mode was initiated, was set to 4.2 kN for the regular tests and 0.8 kN for specimen observation tests, corresponding to stresses of 1.0 MPa and 0.2 MPa, respectively.

The peak-to-peak amplitude and the frequency were changed per regular cyclic test. The requirement for the amplitudes was to not loose contact of the specimen and the upper plate of KNEKKIS, given an initial stress of 1.0 MPa in the specimen. The requirement that dictates the lower limit was the measurability of the strain. The range of periods was chosen to compare the results with existing literature on the frequency dependence with a slight focus on the higher frequencies. For each combination of the amplitude and period the number of cycles were defined. The test matrices per core direction are listed in Figure 3.12 and Figure 3.13. All entries were attempted, but not necessarily successfully. Before and after every row, thus, amplitude, a specimen observation test, with a small amplitude of 0,02 mm and a period of 10 seconds was performed. After every experiment, the specimen is relaxed for twenty minutes before a new test starts.

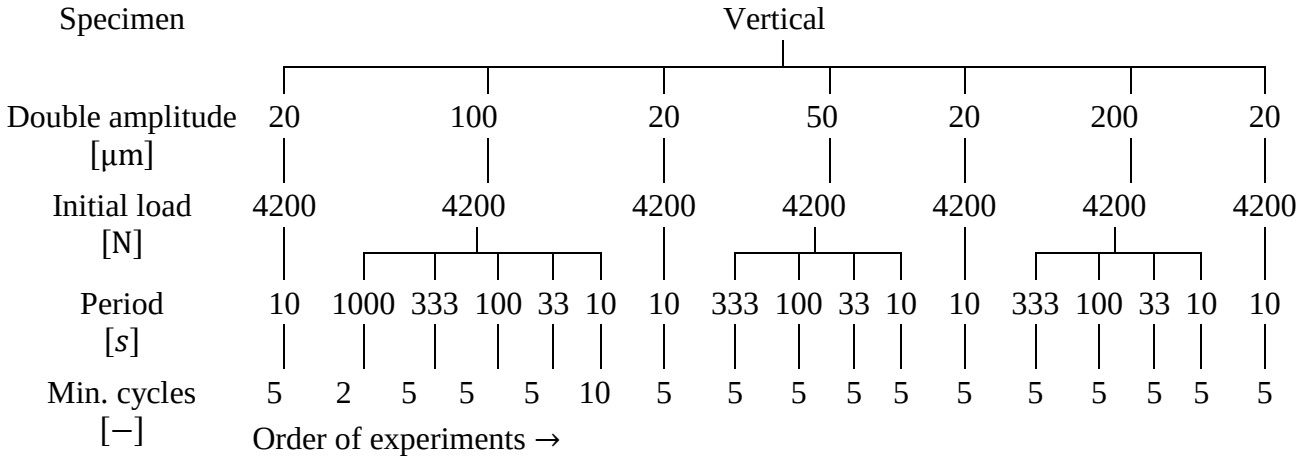

Figure 3.12 Test matrix for cyclic compression experiments on specimens from the vertical cores

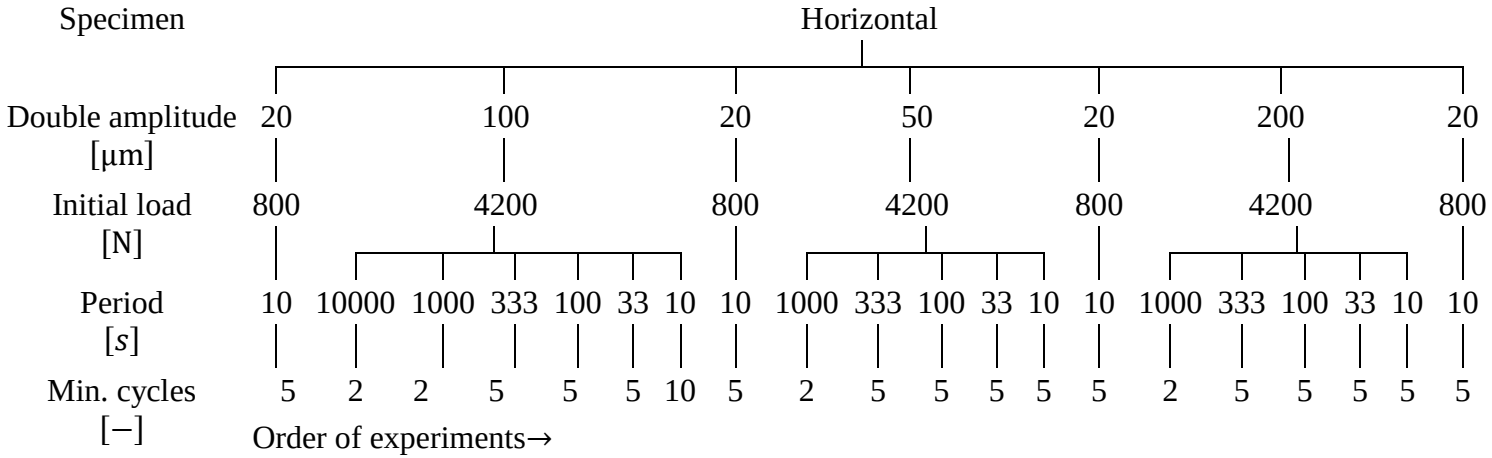

Figure 3.13 Test matrix for cyclic compression experiments on specimens from the horizontal cores

For every specimen stress relaxation tests were performed at different initial stress levels and durations. The same constant rate mode was used, but the cyclic amplitude was set to zero. After release of the specimen, it was relaxed for half an hour before commencing the next test.

After every test, during the relaxation period, the data from the external datalogger was collected from the laboratory. During the tests, the laboratory was not entered. The name of the data was named with the main variables: specimen name and direction (H for horizontal and V for vertical), test number, amplitude [μm], period [s] and switch force [N]. This name is later used for data processing and to refer to tests performed. An example of the test name is shown below.

$$IS02S06H - 02 - 100mum - 10000s - 4200N$$

All tests that were performed are listed in Table 4.6. Starting times were logged independently and can be found in Appendix A.

To assess the stiffness and compliance of KNEKKIS, the cyclic tests were also carried out using an aluminium specimen. The aluminium specimen is a 175 mm tall tube. An important assumption is that the specimen responds linear in the same range of force applied as on the ice specimen. The test matrix for the aluminium is shown in Figure 3.14.

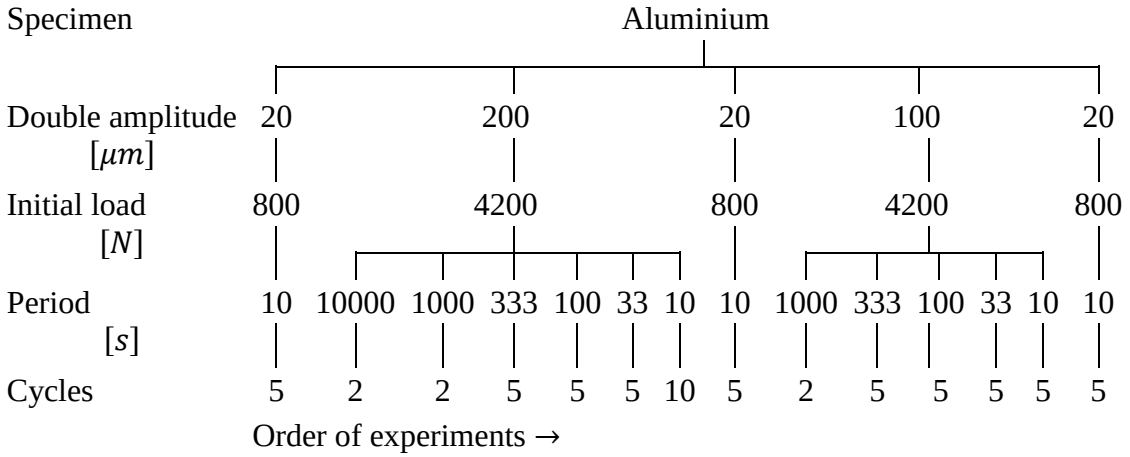

Figure 3.14 Test matrix for aluminium specimen

3.3. Ice specimen characterization

After the cyclic compression tests, the specimens were characterized by measuring their density, salinity and by preparing thin sections. The mid-section of each specimen was cut from the clamps and these properties were subsequently retrieved. The process for the specimen characterization is illustrated in Figure 3.15.

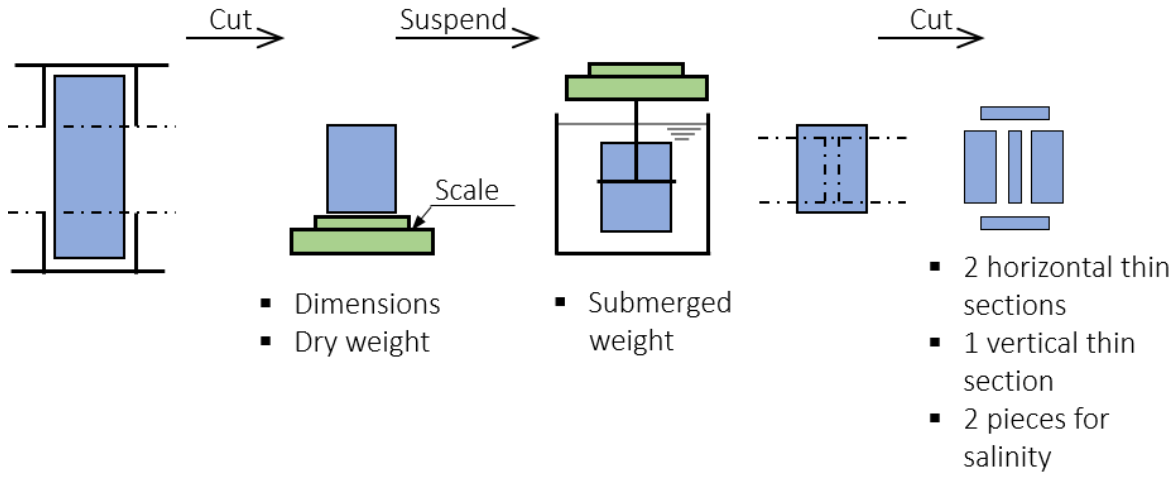

Figure 3.15 Visualization of process to characterize the ice specimens

3.3.1. Temperature, Salinity and Density

Early tests showed that a period of 12 hours is sufficient for the specimen to equilibrate from the storage temperature of $-20℃$ to the temperature in the cold lab of $-10℃$. The common method to measure temperature in a specimen is to drill a hole and measure the temperature inside the specimen with a handheld thermometer. Since each specimen was tested for a timespan ranging from about 12 hours to multiple days in an environment with a constant temperature, this method was not applied, due to the changes of the specimen. Instead, it was assumed that the temperature of the specimen would remain constant at $-10℃$.

The dimensions of the specimens were measured with a caliper. The weight was measured with a scale with a precision of 0,1 g. The scale allows for both weighing on top or hanging a specimen from the device. The volume of the mid-section of the specimen was measured using the hydrostatic weighing method described by (Pustogvar and Kulyakhtin, 2016). The mid-section was subsequently weighed dry and hanging below the scale, submerged. The submersion liquid of choice was paraffin with $\rho = 823\ kg/m^3$. The density of the paraffin at the lab temperature was assessed by weighing 250 ml of paraffin.

After cutting the slices used for thin sections from the mid-section, the residual pieces of ice for the production of thin sections were used to measure the salinity. The pieces were melted. The conductivity meter was cleaned consecutively with tap water and demineralized water, before measuring the specimen.

The three parameters temperature, bulk salinity, and density were used to calculate the brine porosity, air porosity and total porosity, using the equations in Section 2.1.4

3.3.2. Crystallography

A method to assess the crystallography is to make thin sections. A method to do so was suggested and discussed with David M. Cole (CRREL, USA), and adapted to the equipment available at UNIS. Square glass plates, sanding paper, an electrical heating pad (the VMS-A, manufactured by VWR), a mobile band saw, water bottle, microtome (manufactured by Leitz Wetzlar) and a polarizer (type 010195, manufactured by W. Ludolph, Germany) were used in the process.

Thin sections of both the original ice and the tested specimens were made to classify the ice structure to determine the grain sizes. The here applied method to produce thin sections described below was modified from Sinha's method (Sinha, 1977), to produce sections at a higher rate, and was assumed to be adequate for the purpose of this study, since the sections were not inspected by microscope. The thin sections were prepared at -20 °C as the increased hardness of the ice at this colder temperature facilitates the procedure.

A slice, horizontal or vertical, was cut, after which the saw marks were sanded off the cleanest looking face. The glass plate was heated on the heater and the sanded face of the slice was frozen onto the glass plate. Saline meltwater formed around the specimen was removed using a paper tissue and a freshwater dam was applied, using the water bottle, around the specimen to prevent radial brine drainage from the specimen. The freezing process of the slice to the glass plate was accelerated by placing the glass on a solid piece of cold steel (the tank). The glass plate was attached to the microtome by creating a vacuum under the plate. Excess ice was shaved off until a thin layer of ice, i.e. the resulting thin section, was left on the glass plate. The thin section was examined and photographed under cross-polarized light. The alignment of the c-axis was assessed by rotating the specimen and comparing the darkness of the grains, i.e. the darkness of the grains was used as an indicator for the direction of the c-axis. The order of grain size was calculated by dividing the section area by the number of grains.

3.4. Data processing

The force and strain recorded with the external sensors were used to analyze the compliances and moduli of the ice. To analyze the loops the time series were filtered. The performance of the control system was analyzed using the motor steps and force recorded with KNEKKIS.

3.4.1. Initial processing

The stress was calculated by dividing the load onto the specimen by the average area of the specimen, calculated from the mean diameter of the specimen. The stress signal was used to

define the intervals of the constant rate mode and the cyclic mode. The constant interval was defined from the start of the stress until a sudden change in stress. The interval in which the jump or drop of the controlled stepper signal (and thereby stress) occurred was excluded from the processed data file. The cyclic interval was bracketed by the end of this jump and the release of the specimen at the end of the test. Three time series datasets were constructed using stress and strain data processed using three different filtering methods.

3.4.2. Filter external sensor data

The stress and especially the strain signal contained instrumental noise, which was smoothened using a third order Butterworth type filter with a low pass frequency. Slower trends in the stress and strain signals were filtered with a high pass filter.

The focus of this work lies with the response of the material to the controlled frequencies. Therefore, the low pass filter frequency was scaled with the loading frequency. The scale factor was determined by visually assessment of the resulting smoothened signal. This filter was applied to the full dataset for each experiment (i.e. set of parameters) and, for a second dataset, to the cyclic interval separately. The method described by the manual of the strain sensor, to remove the initial offset of the strain sensor was not accurate enough for the low strains applied, so the low pass-filtered strain data was corrected to the strain recorded at the time right before the load was applied to the specimen.

3.4.3. Gauge length influence

Early tests showed a trend in the strain measured by the external strain sensor. This trend resembles the strain of a creep tests. Assuming the stepper signal provides a sinusoidal motion to the bottom plate (this assumption was justified by performing the same experiments on a linear, homogeneous material, see results), the specimen should undergo a similar straining profile. The external sensor measures just the centre section of the ice. A strain signal removed from this creep, which still has the same phase lag (essential to elucidate the anelastic behaviour), can be simulated to represent the full height of the specimen by applying a high-pass filter. The high-pass filter frequency was similarly scaled with the loading frequency, applied on the cyclic interval and included in the third data file

3.4.4. Loop analysis

Each loop of the smoothed cyclic data was analysed separately, i.e. the width (ε_w) and height (σ_h) of each loop was determined, and subsequently used to calculate the loss and storage compliance. Furthermore, the effective modulus was calculated for each loop.

To obtain the separate loops, the time series data had to be split up after each period (i.e. cycle). The first quarter of the first cycle of each experiment was thereby not used, since the filtering of the data led to an artificial jump in that part of the time series.

Subsequently, the maximum, minimum and mean stress and strain values were determined for each loop. From these values, the width and height of the loop were determined. For the loop width, the strain values closest to the mean stress were determined for each half of the loop, for the loop height the stress values closest to the mean strain.

The loss compliance (D_2) was calculated from the loop width and stress amplitude as shown in Equation (3.6). The storage compliance (D_1) was calculated from the loop width, stress (σ_0) and strain amplitude (ε_0) as shown below:

$$D_2 = \frac{\varepsilon_w}{\sigma_0} \tag{3.6}$$

$$D_1 = \sqrt{\left(\frac{D_2\sigma_0}{M_2\varepsilon_0}\right)^2 - (D_2)^2} \tag{3.7}$$

And similarly, for the loss and storage modulus:

$$M_2 = \frac{\sigma_h}{\varepsilon_0} \tag{3.8}$$

$$M_1 = \sqrt{\left(\frac{M_2\varepsilon_0}{D_2\sigma_0}\right)^2 - (M_2)^2} \tag{3.9}$$

The effective modulus was determined from the tangent to the curve at the point of the mean stress, an adaptation of the formula used by Cole, Johnson and Durell (1998). Since each loop passes the mean stress twice, the mean of the tangents was determined to be the effective modulus of the whole loop.

4. Experimental results, model predictions and discussion

The results of the specimen production, the experiments review and the compression tests are presented in this section. The results are interpreted and discussed and the model results are compared to the experimental results.

4.1. Specimen production

In this section the results of the specimen production experiments are presented. First the production of the ice sheets is elaborated on, then the extraction of cores, the choice of specimens and their parameters.

4.1.1. Characteristics of ice sheet

Four ice sheets were produced in the FRYSIS. Each tank was filled with approximately 100 litre of tap sea water with a salinity of 33 and 300 litre of tap water, resulting in a water mixture with a measured salinity of $8.2 \pm .2$. The sheet thickness and growth time of each sheet are shown in Table 4.1.

Table 4.1 Thickness and growth time f each sheet, thickness measurement based on the shortest core length, growth time recorded from moment of seeding to drilling

Ice sheet	**Thickness** [cm]	**Growth time** [days]
IS01	21	9
IS02	23	8
IS03	25	10
IS04	28	10

The temperature in the cold laboratory was not very stable. For each ice sheet the growth conditions were therefore slightly different, resulting in the different growth times per sheet thickness. A difference of the set temperatures of the heating walls compared to the water temperatures was also present. For more control of the growth conditions, these thermometers should be calibrated with the water temperatures. However, in this work, focus was put on growing ice with a S2 structure and not on the exact same growth conditions. The thin sections of IS01, showed no clear S2 structure, as visible in Figure 4.1. This ice sheet and the cores drilled are therefore excluded from further analysis. The other ice sheets have shown a S2 structure.

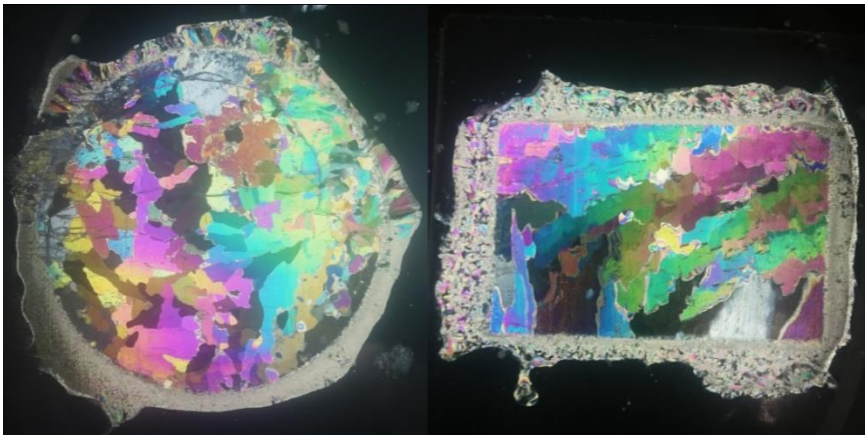

Figure 4.1 Thin sections from first sheet of ice with a horizontal (left) thin section and vertical (right) thin section. The vertical thin section was taken near the top of the ice layer. A columnar structure is recognized in the vertical thin section

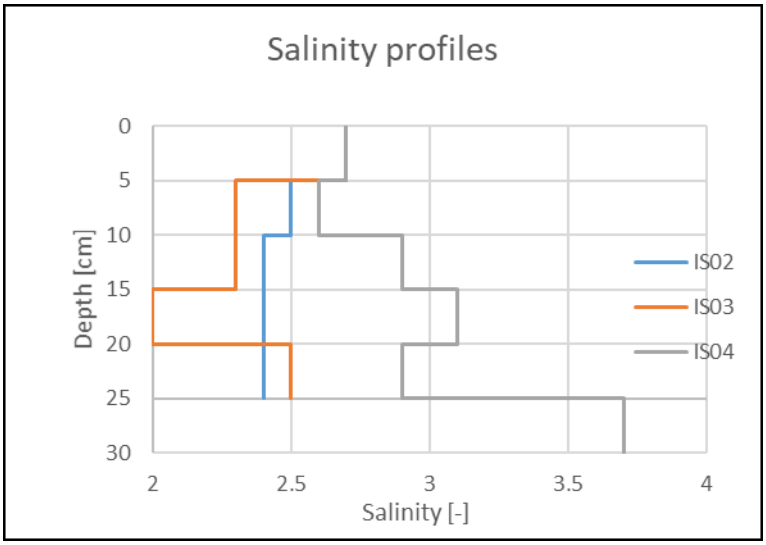

Figure 4.2 Salinity profiles three sheets of ice . Top layer has the same salinity for each sheet

For the sheets 2,3 and 4, salinity profiles were made from the block cut in between the core cavities, shown in Figure 4.2. The average salinity throughout the height of the salinity profile was respectively 2.5, 2.4 and 3.0. Compared to regular sea ice found in the Arctic this is relatively low, but the values compare well to the sea ice found in the Baltic Sea. Especially in IS03 a typical C-shape profile can be recognized, most likely caused by brine drainage to the bottom and brine capture in the top layer. This is an indication that the production of columnar sea is comparable to naturally occurring sea ice growth. Further research with thin sections can confirm this. The salinity in the top layer of all sheets of ice was 2.7.

4.1.2. Extracted cores

A total of 48 cores were drilled from the 3 sheets of ice. A small number of cores was severely damaged during the process as shown inTable 4.2. The damaged cores were excluded from further analysis.

Table 4.2 Number of cores and their condition

		IS02	IS03	IS04	Total
Good samples no flaws	Horizontal	3	4	4	11
	Vertical	11	12	10	33
Samples with flaws	Horizontal	0	1	1	2
	Vertical	1	0	1	2

The distance from the walls of each cores was measured and is visualized in Figure 4.3. The larger blocks of ice in between the core locations were used for horizontal specimens. The choice of drilling locations improved towards the later sheets of ice. The main challenge that drove this development was cutting the blocks of ice used for the horizontal specimens. Working in a relatively narrow tank with steel walls does not allow the use of mechanical cutting, so all cutting was done by hand. The duration of cutting one block was approximately three hours.

The setup of core locations for IS02 was sufficient for the collection of vertical cores. Cutting the horizontal block took approximately five hours. The block (approximately 40 kg) was lifted from the sheet of ice using a combination of levers, support beams and ratchet straps. Due to the size and weight of the block, it was jammed during the lift operation. For IS03 and IS04 the size of the horizontal block was reduced by dividing it in two blocks weighing each less than 20 kg. Cutting of these blocks took each approximately two hours. For IS03 and IS04 the ratio between the clearance at the sides of the blocks and the dimensions of the block was increased. Due to this and the reduced weight, the blocks were not jammed in the sheet of ice and were easier to remove. The double column of cores in the centre of IS04 allowed for thin sections and salinity profiles taken from the centre of the sheet of ice.

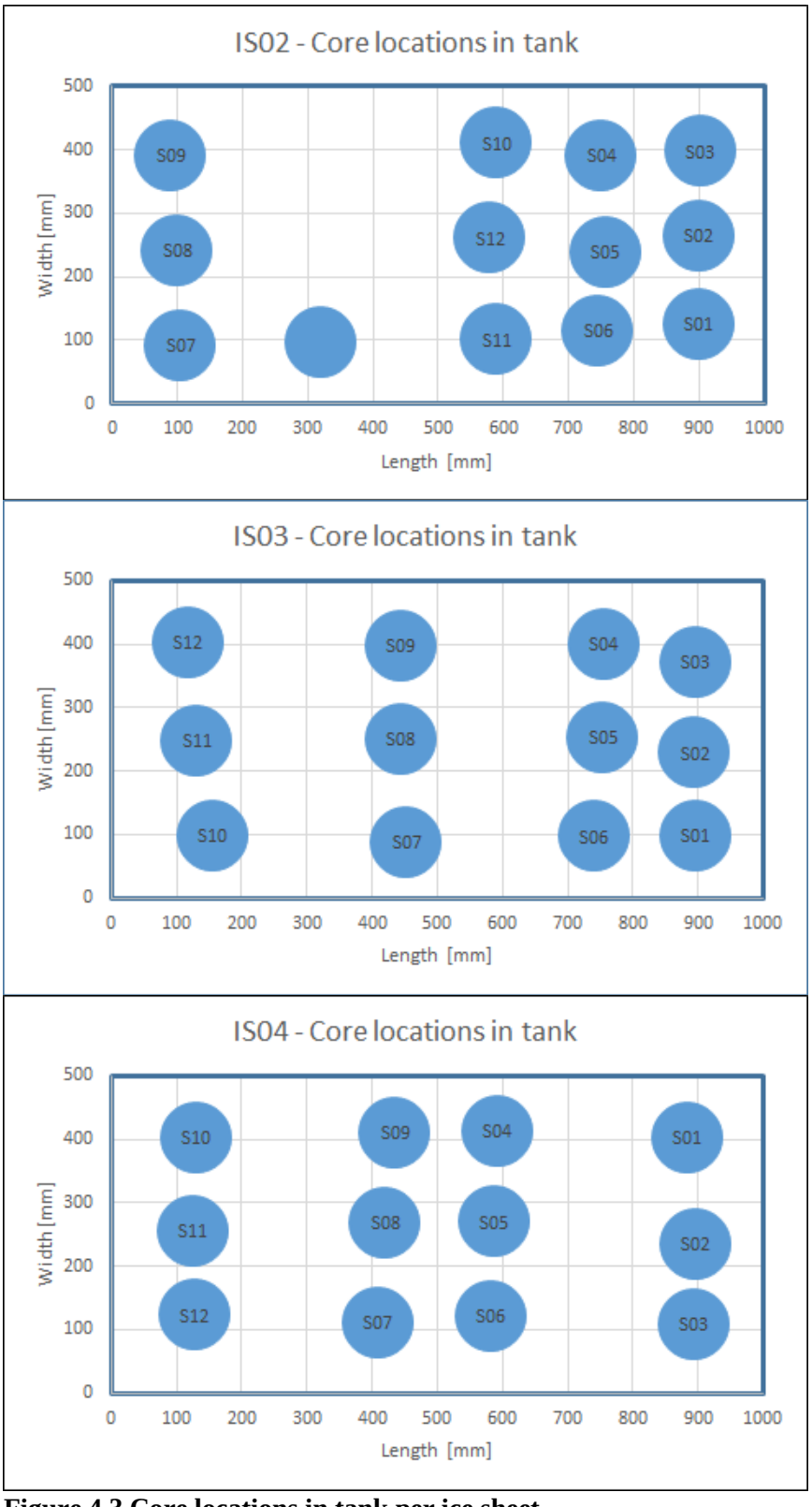

Figure 4.3 Core locations in tank per ice sheet

4.1.3. Specimen characteristics

4.1.3.1. Dimensions specimens

During the final phase of production of cores, it was decided to reuse the cores per cyclic experiment based on reports in literature (Cole and Durell, 1995), thus a surplus of cores was

drilled. Five cores were selected to use for cyclic compression tests. The substantial number of cores produced allowed for a careful selection of cores. Thde selection criterion was the straightness of the core. The coring method often resulted in bent cores. The straightness of the cores was visually estimated and the straightest specimens were chosen. The dimensions of the specimens are listed in Table 4.3.

Table 4.3 Specimen dimensions

Specimen	Length [mm]	Diameter top [mm]	Diameter Center [mm]	Diameter bottom [mm]	Area** [mm2]
IS02S05V	173	73.5	-	75.8	4377
IS02S06V	174	73.5	73.7	77.0	4387
IS03S03V	172	73.9	-	74.7	4336
IS03S15H***	174*	73.3/71.4	-	73.1/70.5	4208/3953
IS03S16H	174*	72.3	-	72.5	4117
ALU	155	82.0****	-	90.0****	1081

* Not measured, but assumed from saw box dimensions

** Calculated from average diameter

*** First diameter measured on 8/12/2016, second diameter on 13/12/2016

**** Inner or outer diameter of aluminium tube

The diameters of the specimens differ slightly from each other, due to the measurement method and because the specimens were not milled to a fixed diameter. The changing diameter of specimen IS03S15H is probably caused by sublimation of the ice over the five days in between the measurements. The diameter of IS02S06V is slightly larger than the inner diameter of the core, which might be a result of ice freezing to the side after the sample had fallen through the hole in the tank. The variation in diameters results in a 10% difference between the largest and smallest area. The area influences the applied stress on the specimen, i.e. the switch load. To apply the same stress for all specimens, a constant area for all specimens can be important. However, since these tests are strain controlled, it is not of utmost importance.

The different diameters of sample IS03S15H are the result of the longer test period for this sample. After storing the sample wrapped in the cold laboratory for a weekend, the diameter was reduced by a few mm. Since this reduction resulted in an area change of 3.1%, the new measurements are included in the processed data.

The ratio of the cross-sectional areas of the aluminium tube to the average cross-sectional area of the ice specimens is approximately 4.0. This ratio can be used to compare the stresses of the aluminium to the ice specimen, since the same input parameters (force) were used.

4.1.3.2. Temperature, Salinity, Density and porosities

The temperature of the cold lab, the density and salinity of the specimens were measured. The porosities were computed. The results are listed in Table 4.4.

Table 4.4 Density, salinity and porosities

Specimen	Tests	Density [kg/m3]	Specimen salinity [−]	Porosities measured at −10℃ [%]		
				air	brine	total
IS02S06V	All	910.2	2.4	1.2	1.3	2.5
IS03S03V	All	910.3	1.9	1.1	1.0	2.2
IS02S05V	All	909.3	1.9	1.2	1.0	2.3
IS03S15H	01-18	903.1	2.2	2.0[1]	0.7[1]	2.8[1]
IS03S15H	18-41	903.1	2.2	1.9	1.2	3.1
IS03S16H	All	903.2	2.6	2.0	1.4	3.4

[1] Temperature during tests was −20℃

[2] Calculated for the mean diameter

The available height between the top and bottom plate of the clamps is 186 mm. However, no exact height measurement was possible for the different specimen. The external strain sensor measures the strain for an original height of 50.0 mm. The clamps are filled with fresh water to freeze the samples to them. Therefore, the contributing height to the total strain in the ice is not defined.

The temperature was accidentally set to -20°C for two days, resulting in a change of the porosity.

4.1.3.3. Microstructure

Four thin sections are presented in Figure 4.4. All originate from ice sheet 3, of which the horizontal cores were used for the cyclic experiments

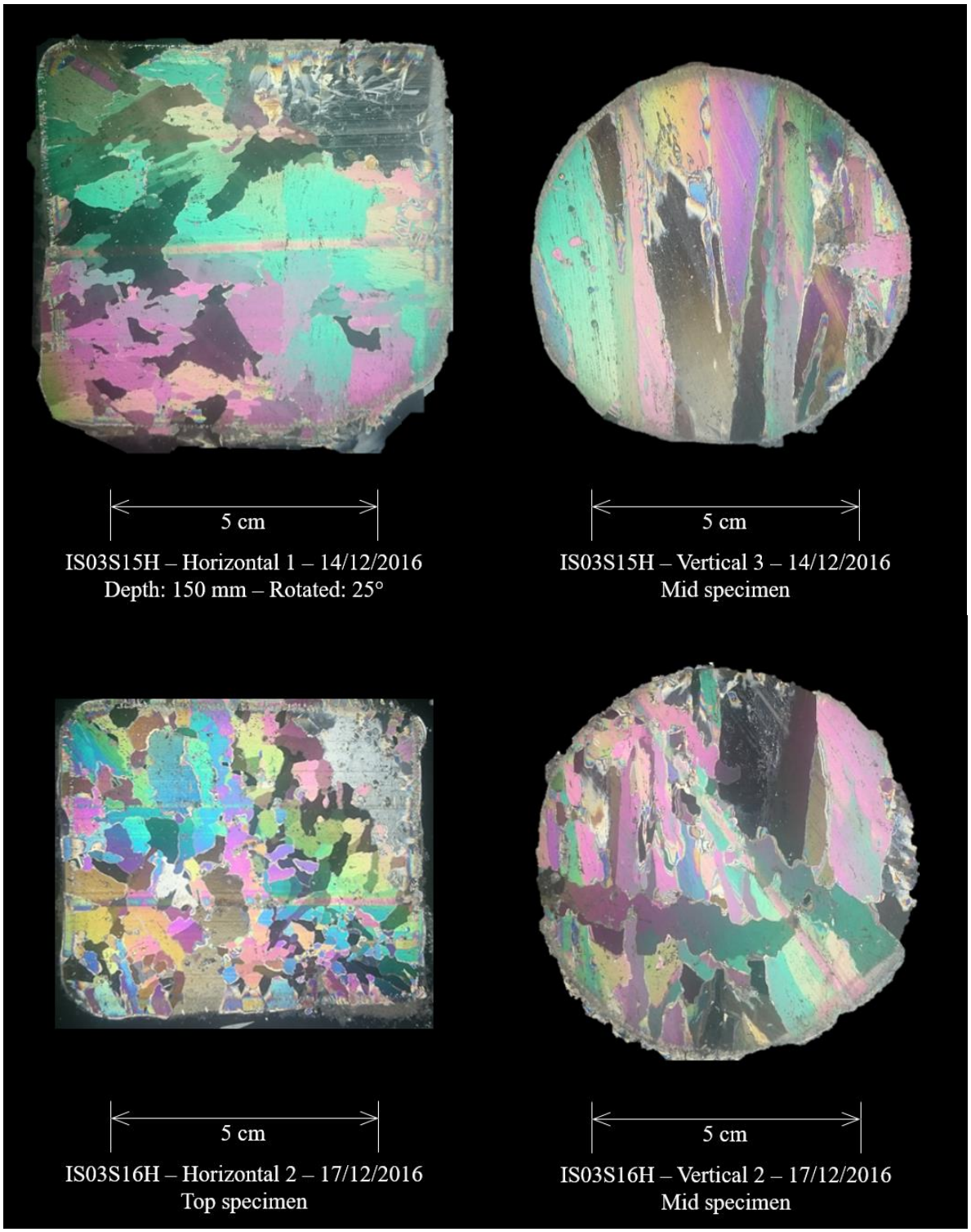

Figure 4.4 Thin sections of ice sheet 3

The structure of the specimens is classified as S2 ice. The direction of the grains, thus the basal planes are oriented vertical. The basal dislocations have the largest influence on the orientation factor. The c-axes of the specimens were unaligned. The grain sizes are in the order for which the model was validated.

4.2. Materials and methods review

4.2.1. Methods

The experimental method was refined during the campaign and all improvements implemented were described in section 3. More improvements were identified after the experimental campaign.

4.2.1.1. Mode switch jump

The mode switch jump describes an observed phenomenon, where the load or displacement jumped to another value when the mode was switched from CSR to Cyclic. The displacement that is used as input was defined by the initial load, initial velocity, displacement amplitude and the period. However, the time offset of the signal was variable with the current control system, since the time between the start of movement of the plates and the contact with the specimen is not specified. This has led to jumps in the input signal and force when changing modes. As the material cannot adjust its strain instantaneous, the resulting strain offset is not known.

4.2.1.2. Displacement profiles

The displacement profiles applied could be improved. Several combinations of experimental parameters prove not to be practical.

The external strain sensor used, was not able to identify the strain when the double amplitude was smaller than 50 μm, further explained in Section 4.2.2.4. The test matrix was followed regardless, resulting in a number of tests which were not possible to process properly. For all experiments, filters were applied to reduce the noise of the stress and strain measurements.

The tests that combine a high amplitude and a low period, proved to be useless as well. The specimen would not relax fast enough to maintain a load; thus, the specimen was released every cycle. These experiments have not been included in the analysis.

The compressive experiments include stress relaxation of the specimen, which must be either subtracted or filtered, to analyse the steady state behaviour. For an easier assessment of the steady state behaviour a cyclic compression-tension experiments can be conducted. With these experiments, the viscous deformation can be identified.

4.2.1.3. Temperature measurement

The temperature of the specimen was not measured, but assumed based on the room temperature. This was justified for this work. The commonly used method (drilling a hole in the specimen and measuring the inside temperature with a thermometer) destroys the specimen and it makes them useless for more experiments. A suggested method to measure

the temperature is by the use of a thermal imaging sensor. Using this method, the temperature of a specimen can be measured at any given time, however it is uncertain if these sensors can measure the temperature inside the specimen.

4.2.1.4. KOMPIS cyclic loading method

The triangular compression tests were conducted using KOMPIS. The preliminary results made evident that the available equipment was not suitable to obtain results that could be straightforwardly compared to the model predictions.

A structural issue of KOMPIS was the low range of loading rates that could be applied to the ice sample. KOMPIS is designed to move the plate on 1500 rotations per minute (rpm), which resulted in a strain rate of the specimen of 10. The gearbox could not provide enough force to strain the specimen on a lower rpm. Because of the low range of velocities, the obtained low range of frequencies could not be applied while remaining in a low-stress regime.

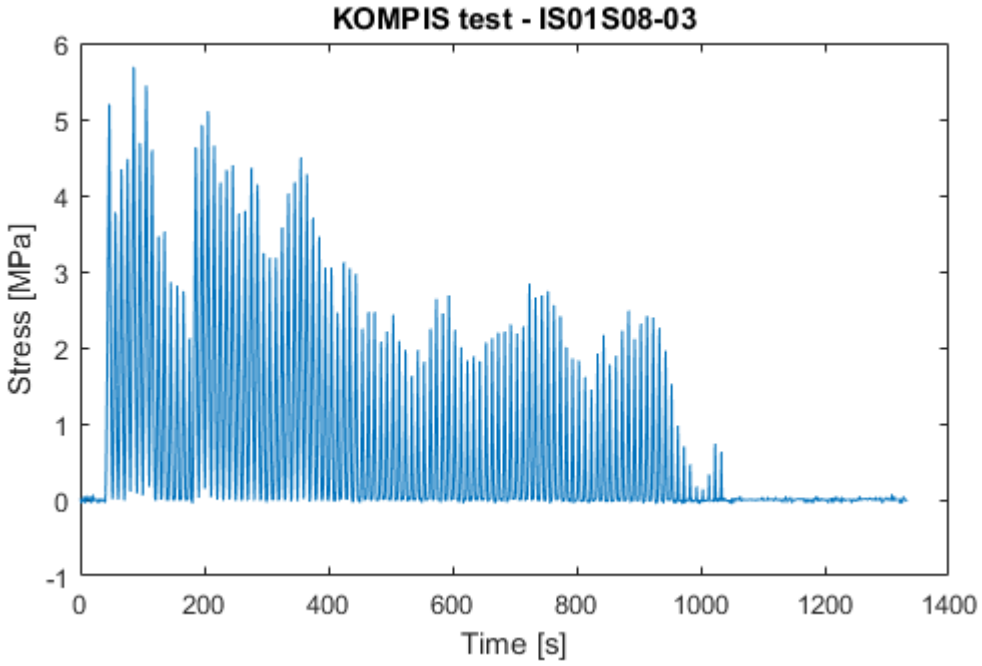

Figure 4.5 Recorded stress for triangular load on specimen IS1S08-03

The frequency was controlled by manually operating the control switch and lead to a release of the specimen and irregular cyclic per2.7iods as shown in Figure 4.5. As a result, the peak loads per cycle changed from cycle to cycle as shown in Figure 4.6

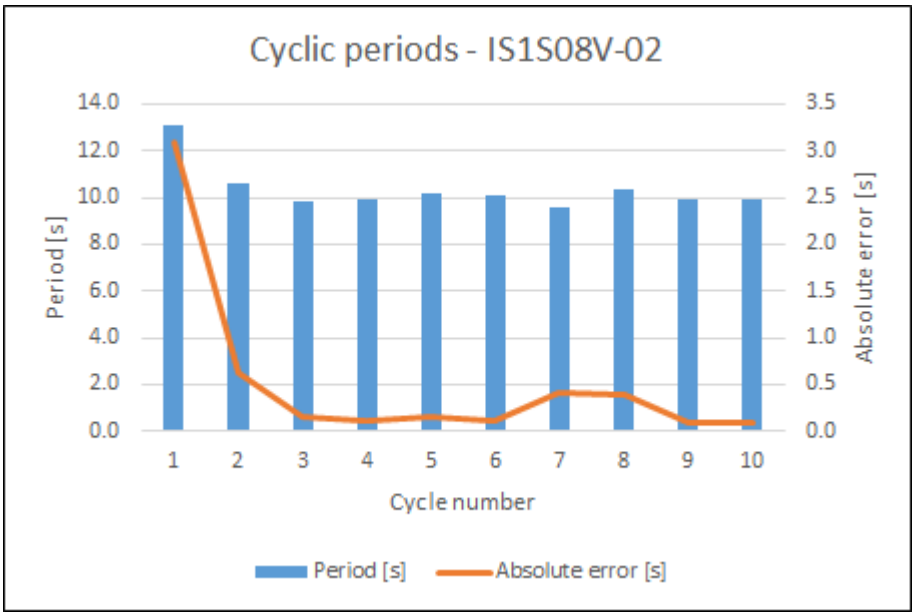

Figure 4.6 Period per cycle by manual operation of KOMPIS

The strain of the whole specimen was measured with the draw wire. This direct measurement of the strain can be very useful, as discussed in Section 4.2.1.2. However, the resolution of the draw wire was too low to measure the strain in the specimen (see Figure 4.7), which rendered this strain sensor useless. An improvement to the strain measurement was applied after the experimental campaign of this work, by installing a linear variable differential transformer (LVDT).

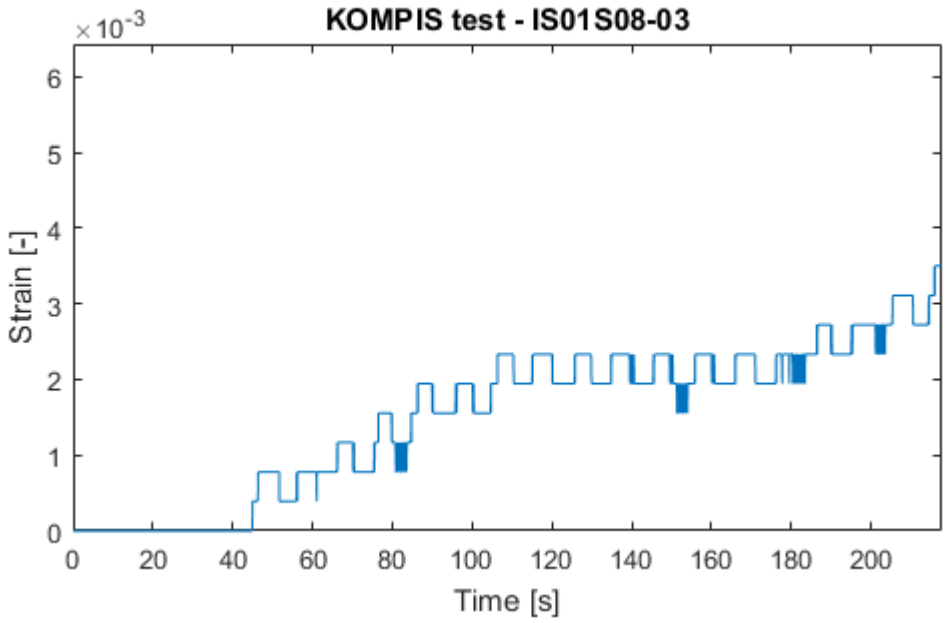

Figure 4.7 Strain for KOMPIS test

The triangular cyclic loading method might prove valuable for future cyclic loading experiments, if the problems concerning the control and the gearbox are addressed. The ease-of-use and mobility of the method are valuable qualities for field applications.

4.2.1.5. Thin section production

The adopted method to produce thin sections reduced the production time significantly. The method is recommended to use for quick production of thin section, when the thin sections are not analysed by microscope. This method provided good enough thin sections to assess the columnar structure and grain sizes.

4.2.1.6. Filters

The low pass frequency filter performed well to reduce noise from the cyclic part of the tests. However, they could not handle sudden changes, such as mode switches or tests where the upper plate lost contact with the specimen. The low-pass frequency was dependent on the natural frequency and the performance of this frequency was visually assessed from the stress.

The start of the cyclic part is problematic for using the low-pass filter. Low-pass filters appeared to be not suitable for the higher periods (1000 and 333 seconds) due to their inability to smoothen parts with creep. Calculations based on test with low-pass filters exclude therefore the first ten percent of the cycle. Problems occurred also in the very last part, again especially for the higher periods (1000 and 333 seconds). However, this part is usually not part of any cycles anymore and thus negligible. For lower periods, the switch from constant rate mode to cyclic mode is more fluent in comparison to the input period as shown in Figure 4.8.

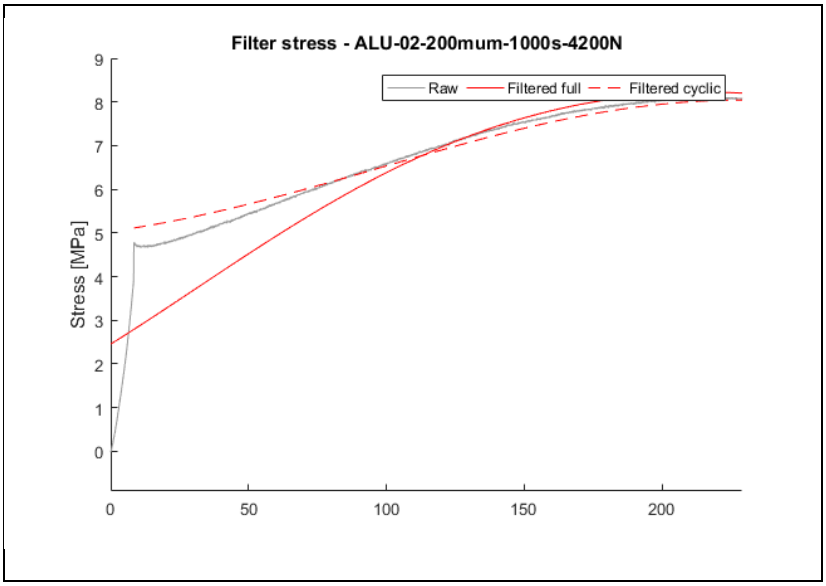

Figure 4.8 Filter performance for first 10% of the first cycle

The low pass filter frequency scaled with the frequency at which the cyclic test was performed. For the tests with an initial load of 4.2 kN, a scale factor of 5 provided smooth results. Smoothness was determined by visual observation, was determined visually, but a least-square analysis could be conducted to further improve the results. The low pass filter frequency for the observation tests with a low amplitude (20 μm) and at an initial load of 0.8 kN was scaled with a factor 2. A significant amount of information was lost, thus the findings with regards to these filtered files are treated carefully.

A scaling factor of $1/3$ was applied to the loading frequency to obtain the high pass filter frequency.

4.2.2. Materials

4.2.2.1. Loading frame

When the stepper engine, the controlled parameter, applies a load not just the specimen is loaded. The frame, the load cell and the endcaps are also compressed. For the experiments, the load cell and the end caps were assumed to be incompressible since only relatively low forces were applied (not higher than 10 kN). The frame however has shown some self-deformation in previous tests. It is also not known if the frame has a frequency dependent stiffness.

To predict the stresses resulting from a strain input with any model, it is important to know what the input strain is. The input strain amplitude results from the peak to peak amplitude for the stepper engine used for the experiment. Two types of experiment can be used to compare the input parameters to the resulting strain in the specimen:

1. Compression of incompressible steel beam, conducted in 2013
2. Compression of aluminium specimen, assumed the material behaves linear homogeneous elastic over its length under the load conditions applied

The compression tests on ice cannot be used for the stiffness of KNEKKIS, since the strain contributing height of the specimen is not well defined due to the use of end caps.

With the self-deformation of KNEKKIS as a function of the load and the load - a result of the stiffness of KNEKKIS - the stiffness of KNEKKIS is non-linear, thus the resulting input strain for a material (that is not assumed infinitely stiff) cannot be predicted by just this knowledge. The self-deformation is often included for tests, if the self-deformation is much lower than the deformation of the specimen. The displacement is than corrected by substituting the self-deformation. Since the self-deformation for the low loads is relatively

high for the amplitudes used as input (see Table 4.5), this approach was not applicable for this work.

With the current setup, where the strain sensor measures the center section of the material, no definite answer on the stiffness of KNEKKIS can be given. However, when using the strain measured in the strain sensor a stress should be possible to predict with a model.

The measured strain double amplitude can be compared to the respective input parameter. Major assumption: homogeneous elastic material, thus, strain measured in the middle can be used to calculate strain over the full length of the specimen:

$$d_{kne} = A_{p2p} - d_{ext} = A_{p2p} - \varepsilon_{ext} l_{spec} \tag{4.1}$$

where d_{kne} is the displacement of the bottom plate, A_{p2p} the double amplitude used as the input, d_{ext} the projected displacement of the bottom plate, ε_{ext} the strain measured by the external sensor and l_{spec} the length of the specimen. With the given assumptions, the approximately 90% of the input strain is lost due to the stiffness of the frame. For the validation of the model it is therefore important not to use the input parameter, but the measured parameter.

Table 4.5 Frame deformation

Experiment	**peak-to-peak amplitude strain** $\varepsilon_{p2p,ext}$ [-]	**Ratio** $\frac{\varepsilon_{p2p,ext}}{\varepsilon_{p2p,in}}$ [%]	**Assumed specimen deformation** $\boldsymbol{d_{ext}}$ $[\boldsymbol{\mu m}]$	**Frame deformation** $\boldsymbol{d_{kne}}$ $[\boldsymbol{\mu m}]$
ALU-02-200mum-1000s-4200N	9.31E-05	7.2%	14.4	185.6
ALU-03-200mum-333s-4200N	1.04E-04	8.0%	16.1	183.9
ALU-04-200mum-100s-4200N	1.04E-04	8.1%	16.2	183.8
ALU-05-200mum-33s-4200N	1.59E-04	12.4%	24.7	175.3
ALU-10-100mum-333s-4200N	5.41E-05	8.4%	8.4	91.6
ALU-11-100mum-100s-4200N	5.18E-05	8.0%	8.0	92.0
ALU-12-100mum-33s-4200N	5.00E-05	7.8%	7.8	92.2
ALU-13-100mum-10s-4200N	4.61E-05	7.1%	7.1	92.9

The main problem is the self-deformation of the frame and not well known for these relatively low stresses. To avoid the problem only strain in the specimen itself was measured, which was the focus of this work anyways.

To allow for a better controlled strain input several solutions are suggested.

The deformation between plates can be measures as well as the plate deformation. Tests on similar specimens of ice can be performed to retrieve a new calibration factor, i.e. number of steps compared to plate deformation. Since the stiffness of the frame is nonlinear load dependent, this calibration factor should be tested for the load range applied. Therefore, multiple calibration tests per experimental campaign recommended

A more permanent solution, without the need for calibrations, might be to expand the control system in a way that the measured deformation can be used as a new input, providing a closed feedback loop.

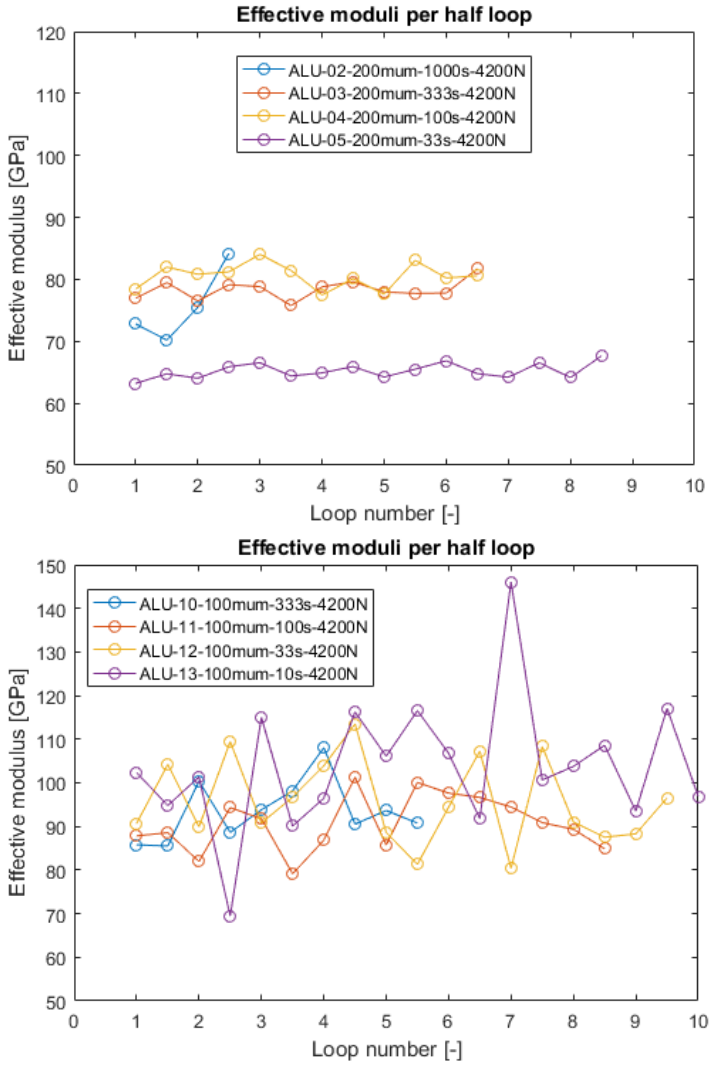

Figure 4.9 Effective modulus per half loop, calculated at mean stress of the loop

The stiffness of the aluminium specimen is relatively stable per strain amplitude as shown in Figure 4.9.

The stress plot, see Figure 4.8, is a typical result from the tests on aluminium since the system is strain controlled as described in and no stress reduction occurs during the different tests.

For the 10 seconds period a bit of creep is visible in the first cycle. It is not clear whether this creep results from creep in the frame or creep in the specimen.

Stress relaxation tests at different initial stresses can provide an answer to whether this influences the duration and intensity of the creep.

4.2.2.2. End caps

The end caps were a valuable piece of new equipment for compression tests under low stresses. A slow stress increase was observed when a small displacement was applied to the

specimen. The specimen was less than half an hour prior to this test clamped. The fresh water applied to freeze the specimen to the clamp was not frozen yet. To prevent this from having an influence on the actual experiments, a specimen must be frozen into end caps well before compression test commences.

The end caps provided a proper alignment of the specimen, relatively independent of the quality (parallel faces and normal to the longitudinal axis) of the cuts. Another advantage of the end caps is the range of specimen heights that can be used. Within a reasonable range the operational height between the plates of KNEKKIS remained the same.

Disadvantages of the end caps were the following. The fastening system (water in the end caps) caused a variable height of fresh water ice between the specimen and the specimen. The interference of this extra connection to the end caps is unknown. The strain measurement was not influenced, but it is unknown what happens to the sample between the sensor and the end of the sample.

A more practical disadvantage is the removal of the specimen from the end caps. A significant amount of height is lost when the specimen is cut from the end caps. A reduction of the height of the end caps, while maintaining the height of the mantle might solve this. Top and bottom of specimen cannot be retrieved without warming up end caps. Irregularities in the diameter of the specimen can influence alignment of specimen.

4.2.2.3. Load cells

Two load cells are used to measure the applied force, one built into Knekkis, one external load cell. The performance of the two varies slightly.

The signal of the Knekkis and external load cell, without a load applied, vary respectively with +/- 2 N around -1 N and with +/- 40 N around +10 N. With the peak load of an order of 5 kN, resulting in a 0.2% error, no corrections are made to the mean values of the load cells.

A low-pass filter is applied to remove the noise in the signal of the external load cell. The load cell was however precise enough to

The precision of the Knekkis load cell is high enough to identify the steps of the Knekkis engine, as visible in Figure 4.10.

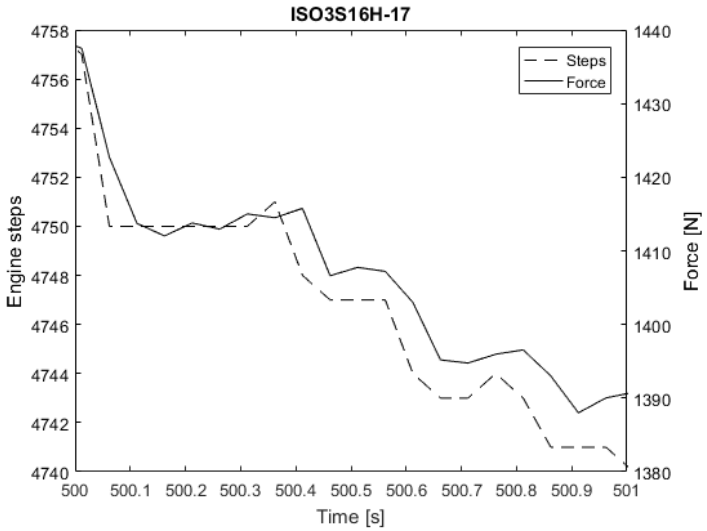

Figure 4.10 Stepper input and load measurement

4.2.2.4. Strain sensor

A significant amount of noise was visible in the strain signals. The noise proved to be too large to analyse the observation test. However, for larger amplitudes the used sensor provided good results. The difference is shown in Figure 4.11 and Figure 4.12.

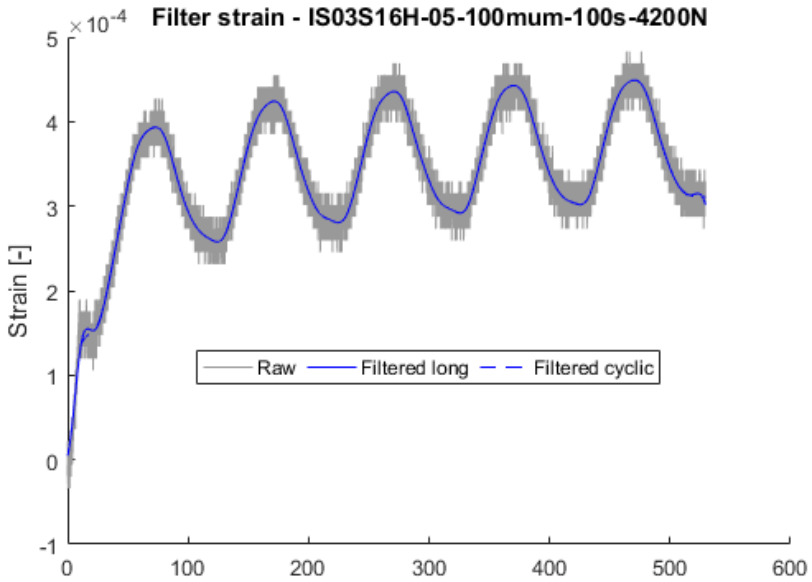

Figure 4.11 Raw strain of cyclic loading test, with filtered signals

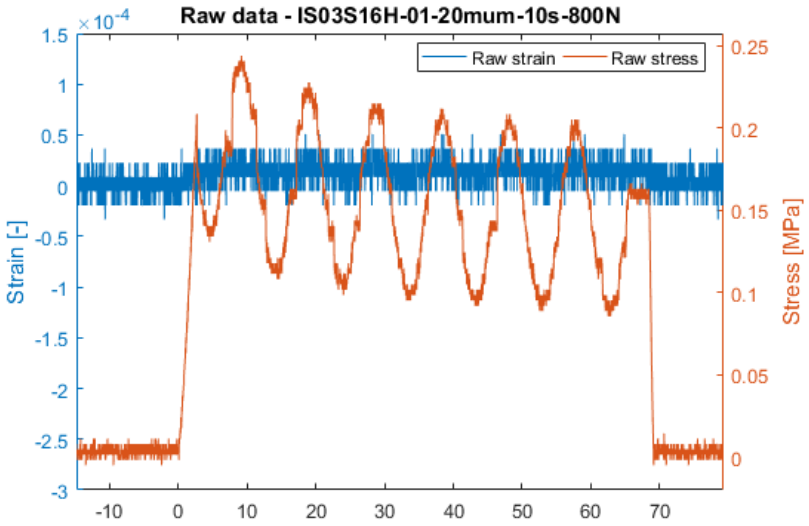

Figure 4.12 Unfiltered stress and strain measured in observation test

4.3. Compression experiments

In total 121 compression experiments in KNEKKIS were performed, of which 74 were executed on vertical specimens and 60 on horizontal specimens. The complete list of experiments, with their relative experimental parameters, is shown in Table 4.6.

Not all specimens are further discussed in this study as earlier specimen were used to improve the experimental set-up. The experiments on specimen IS03S16H were analysed. The anelastic component due to dislocation relaxation was expected to be larger for horizontal specimens, since the orientation factor is larger (see section 2.3.3). The first 18 experiments on the other horizontal specimen, IS03S15H were performed either without external strain sensor or at a different temperature than $-10℃$. The subsequent tests were conducted according to the test matrix. For these experiments, the stress history on the specimens was not completely known and the influence of this on the dislocation density is unclear. It is therefore not further analysed.

First the general characteristics of a cyclic loading experiment are analysed. The cyclic compression tests on specimen IS03S16H are then qualitatively analysed, whether they can be used to analyse the loss compliance. The frequency dependence of the loss compliance is compared to the model prediction.

Table 4.6 All compression experiments performed in KNEKKIS. The label

IS02S06V	IS03S03V	IS02S05V	IS03S15H	IS03S16H
IS02S06V-01-100mum-10s-4200N	IS03S03V-01-20mum-10s-4200N	IS02S05V-1-0mum-s-100N	IS03S15H-1-0mum-s-1000N	IS03S16H-01-20mum-10s-800N
IS02S06V-02-100mum-30s-4200N	IS03S03V-02-100mum-1000s-4200N	IS02S05V-2-20mum-10s-4200N	IS03S15H-2-0mum-s-2100N	IS03S16H-02-100mum-10000s-4200N
IS02S06V-03-100mum-10s-4200N	IS03S03V-03-100mum-333s-4200N	IS02S05V-3-100mum-1000s-4200N	IS03S15H-3-0mum-s-4200N	IS03S16H-03-100mum-1000s-4200N
IS02S06V-04-100mum-30s-4200N	IS03S03V-04-100mum-100s-4200N	IS02S05V-4-100mum-333s-4200N	IS03S15H-4-20mum-10s-800N	IS03S16H-04-100mum-333s-4200N
IS02S06V-05-100mum-100s-4200N	IS03S03V-05-100mum-33s-4200N	IS02S05V-5-100mum-100s-4200N	IS03S15H-5-50mum-1000s-4200N	IS03S16H-05-100mum-100s-4200N
IS02S06V-06-100mum-333s-4200N	IS03S03V-06-100mum-10s-4200N	IS02S05V-6-100mum-33s-4200N	IS03S15H-6-50mum-333s-4200N	IS03S16H-06-100mum-33s-4200N
IS02S06V-07-100mum-1000s-4200N	IS03S03V-07-20mum-10s-4200N	IS02S05V-7-100mum-10s-4200N	IS03S15H-7-50mum-100s-4200N	IS03S16H-07-100mum-10s-4200N
IS02S06V-08-20mum-10s-4200N	IS03S03V-08-50mum-333s-4200N	IS02S05V-8-20mum-10s-4200N	IS03S15H-8-50mum-33s-4200N	IS03S16H-08-20mum-10s-800N
IS02S06V-09-50mum-333s-4200N	IS03S03V-09-50mum-100s-4200N	IS02S05V-9-50mum-333s-4200N	IS03S15H-9-50mum-10s-4200N	IS03S16H-09-20mum-10s-800N
IS02S06V-10-50mum-100s-4200N	IS03S03V-10-50mum-33s-4200N	IS02S05V-10-50mum-100s-4200N	IS03S15H-10-20mum-10s-4200N	IS03S16H-10-50mum-1000s-4200N
IS02S06V-11-50mum-33s-4200N	IS03S03V-11-50mum-10s-4200N	IS02S05V-11-50mum-33s-4200N	IS03S15H-11-0mum-s-500N	IS03S16H-11-50mum-333s-4200N
IS02S06V-12-50mum-10s-4200N	IS03S03V-12-20mum-333s-4200N	IS02S05V-12-50mum-10s-4200N	IS03S15H-12-20mum-10s-4200N	IS03S16H-12-50mum-100s-4200N
IS02S06V-13-20mum-10s-4200N	IS03S03V-13-20mum-100s-4200N	IS02S05V-13-20mum-10s-4200N	IS03S15H-13-20mum-333s-4200N	IS03S16H-13-50mum-33s-4200N
IS02S06V-14-0mum-s-4200N	IS03S03V-14-20mum-33s-4200N	IS02S05V-14-20mum-333s-4200N	IS03S15H-14-20mum-100s-4200N	IS03S16H-14-50mum-10s-4200N
IS02S06V-15-20mum-10s-4200N	IS03S03V-15-20mum-10s-4200N	IS02S05V-15-20mum-100s-4200N	IS03S15H-15-20mum-33s-4200N	IS03S16H-15-20mum-10s-800N
IS02S06V-16-20mum-333s-4200N	IS03S03V-16-200mum-333s-4200N	IS02S05V-16-20mum-33s-4200N	IS03S15H-16-20mum-10s-4200N	IS03S16H-16-200mum-1000s-4200N
IS02S06V-17-20mum-100s-4200N	IS03S03V-17-100mum-10s-4200N	IS02S05V-17-20mum-10s-4200N	IS03S15H-17-100mum-1000s-4200N	IS03S16H-17-200mum-333s-4200N
IS02S06V-18-20mum-33s-4200N	IS03S03V-18-0mum-0s-4200N	IS02S05V-18-200mum-333s-4200N	IS03S15H-18-100mum-333s-4200N	IS03S16H-18-200mum-100s-4200N
IS02S06V-19-20mum-10s-4200N		IS02S05V-19-200mum-100s-4200N	IS03S15H-19-20mum-10s-4200N	IS03S16H-19-0mum-s-4200N
IS02S06V-20-500mum-333s-4200N		IS02S05V-20-200mum-33s-4200N	IS03S15H-20-20mum-10s-800N	
IS02S06V-21-200mum-333s-4200N		IS02S05V-21-0mum-s-4200N	IS03S15H-21-50mum-1000s-4200N	
IS02S06V-22-200mum-100s-4200N		IS02S05V-22-0mum-s-2100N	IS03S15H-22-50mum-333s-4200N	
IS02S06V-23-20mum-10s-4200N		IS02S05V-23-0mum-s-1000N	IS03S15H-23-20mum-10s-800N	
			IS03S15H-24-50mum-1000s-4200N	
			IS03S15H-25-20mum-10s-800N	
			IS03S15H-26-50mum-1000s-4200N	
			IS03S15H-27-50mum-333s-4200N	
			IS03S15H-28-50mum-100s-4200N	
			IS03S15H-29-50mum-33s-4200N	
			IS03S15H-30-50mum-10s-4200N	
			IS03S15H-31-20mum-10s-800N	
			IS03S15H-32-100mum-1000s-4200N	
			IS03S15H-33-100mum-333s-4200N	
			IS03S15H-34-100mum-100s-4200N	
			IS03S15H-35-100mum-33s-4200N	
			IS03S15H-36-100mum-10s-4200N	
			IS03S15H-37-20mum-10s-800N	
			IS03S15H-38-0mum-s-0N	
			IS03S15H-39-20mum-10s-800N	
			IS03S15H-40-200mum-1000s-4200N	
			IS03S15H-41-0mum-s-4200N	

4.3.1. General characteristics of the cyclic straining experiments

The result of a cyclic compression experiment is shown in Figure 4.13. The stress and strain are noise filtered. The strain shows a slow increase during the test. This may be explained by the creep of the specimen and the control mode. The stepper signal is the controlled value and during the experiment creep of the specimen occurs. This creep behaviour is filtered with the low-pass filter, as shown in section 4.2.1.6. The stress is slowly decreasing over time, showing stress relaxation. The stress relaxation is explained by the compression of the specimen. To reduce the creep and stress relaxation behaviour a different displacement profile could be used. A cyclic displacement in which the mean displacement is zero, thus compression and tension alternate.

The stress-strain curve is plotted in Figure 4.14. The shift of the loops to the right is caused by the creep and the shift downwards by the stress relaxation. The loop width and height are clearly visible and can be estimated to obtain the loss function.

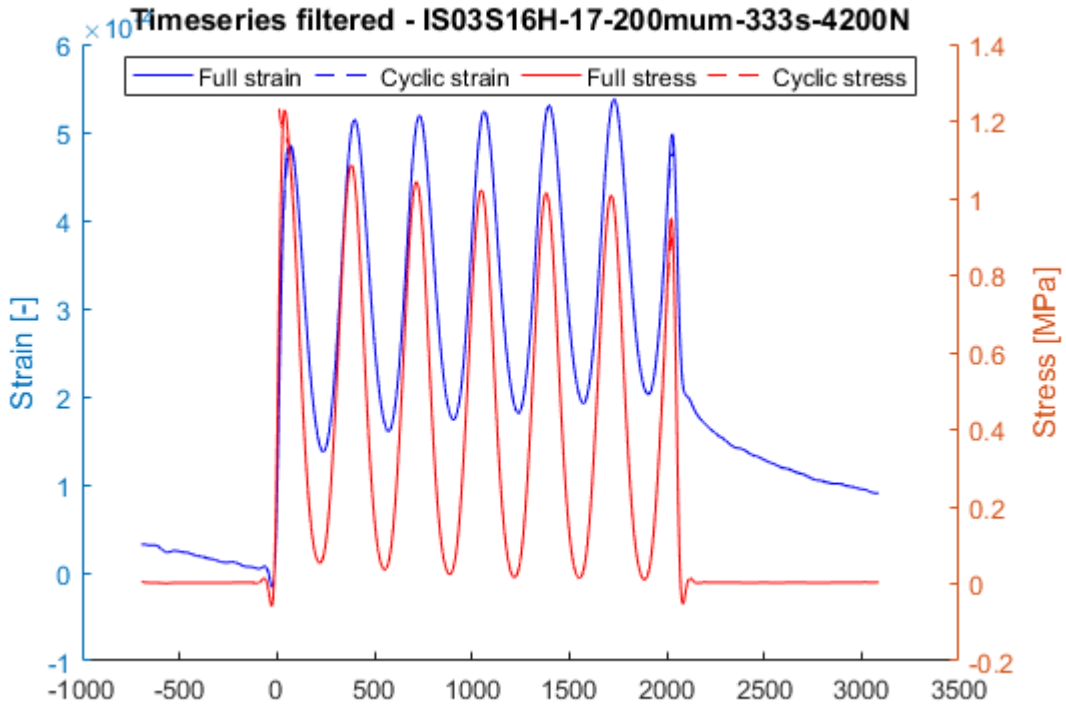

Figure 4.13 Noise filtered stress and strain time series for test IS03S16H-17

a

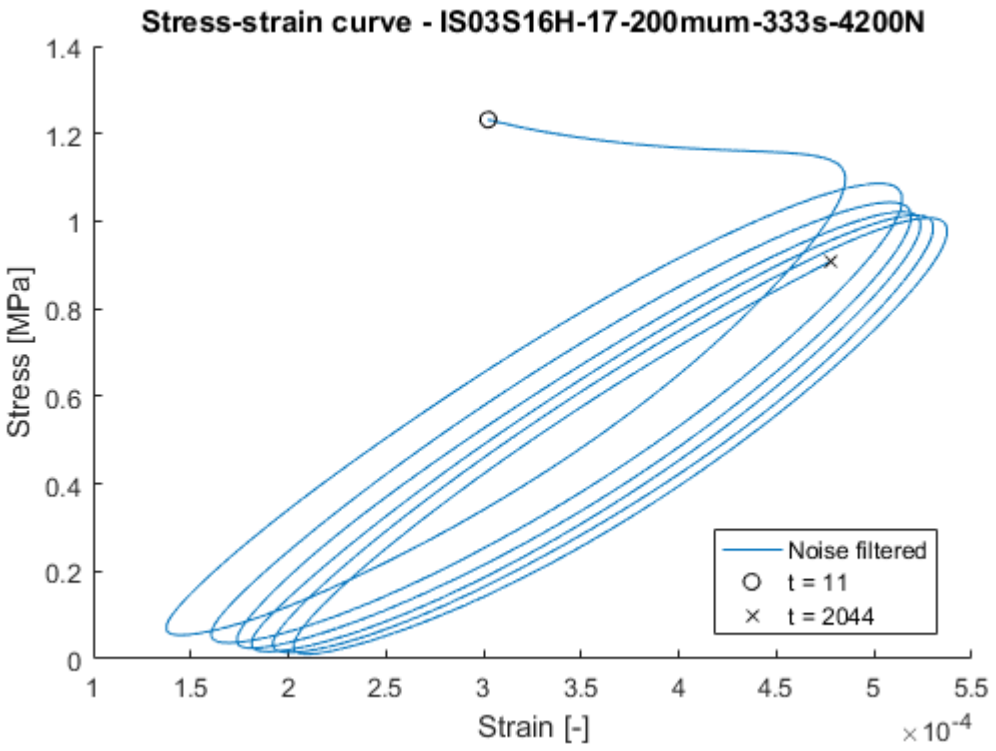

Figure 4.14 Loops for experiment IS03S16H-17

4.3.2. Qualitative analysis of experiments

Not all experiments proved to be meaningful to estimate the loop characteristics. The loops of each experiment are reviewed and marked whether they are further analysed in Table 4.7. All loops of specimen IS03S16H can be found in Appendix C

Table 4.7 Qualitative analysis of the compression tests on specimen IS03S16H

Experiment name	Used	Explanation
IS03S16H-01-20mum-10s-800N	no	Too small strain for loop analysis
IS03S16H-02-100mum-10000s-4200N	yes	Creep dominated
IS03S16H-03-100mum-1000s-4200N	yes	Fast unloading, clear loops
IS03S16H-04-100mum-333s-4200N	yes	Drop in force, clear loops
IS03S16H-05-100mum-100s-4200N	yes	Drop in force, clear loops
IS03S16H-06-100mum-33s-4200N	yes	Clear loops
IS03S16H-07-100mum-10s-4200N	yes	Clear loops
IS03S16H-08-20mum-10s-800N	no	No strain measurement
IS03S16H-09-20mum-10s-800N	no	Too small strain for loop analysis
IS03S16H-10-50mum-1000s-4200N	yes	Clear loops
IS03S16H-11-50mum-333s-4200N	yes	Clear loops
IS03S16H-12-50mum-100s-4200N	yes	Large relaxation in first cycle
IS03S16H-13-50mum-33s-4200N	yes	Stress and strain reached steady-state (asymptotic)
IS03S16H-14-50mum-10s-4200N	yes	Clear loops
IS03S16H-15-20mum-10s-800N	no	Too small strain for loop analysis
IS03S16H-16-200mum-1000s-4200N	yes	Clear loops
IS03S16H-17-200mum-333s-4200N	yes	Clear loops

IS03S16H-18-200mum-100s-4200N	yes	Release of specimen
IS03S16H-19-0mum-0s-4200N	yes	Stress relaxation test

Furthermore, a jump in force was noticed during the mode switch. At lower frequencies, these appeared as a stress relaxation test, but whereas for higher frequencies the stress relaxation is more of a direct drop of force. The cause remains unclear, but has an influence on the shape of the first loop. Since the focus is on the steady state behaviour of the material, the first loop is ignored in the further analysis.

4.3.3. Effect of number of cycles on anelastic behaviour

It is not yet known if the number of loops has an influence on the effective modulus or the loss compliance. The number of loops can be of importance for the choice of the loop to analyse. The effective modulus was determined from the noise filtered data file.

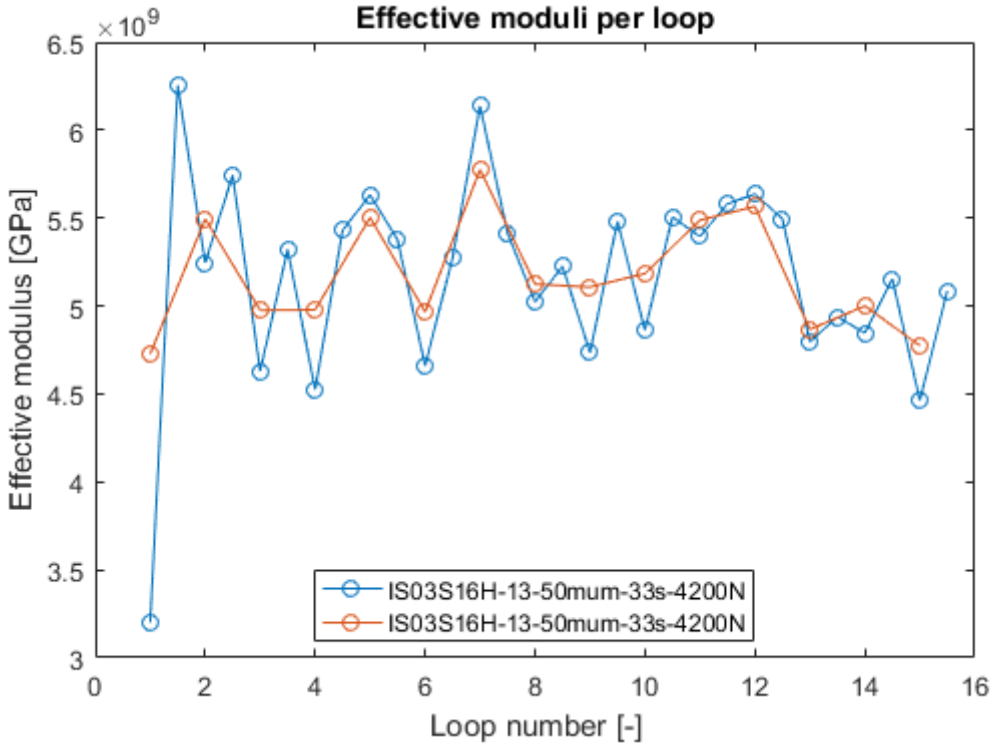

Figure 4.15 Effective moduli determined per half loop

The effective modulus was determined for each crossing of the mean stress, hence two moduli per loop were determined. As shown in Figure 4.15, a difference between consecutive half loop moduli is visible. However, the effective modulus was relatively stable over time, after the first loop.

The loss compliances were derived from the detrended data files and are shown as a function of the loop number in Figure 4.16. The loss compliances are relatively stable for loop numbers greater than 3.

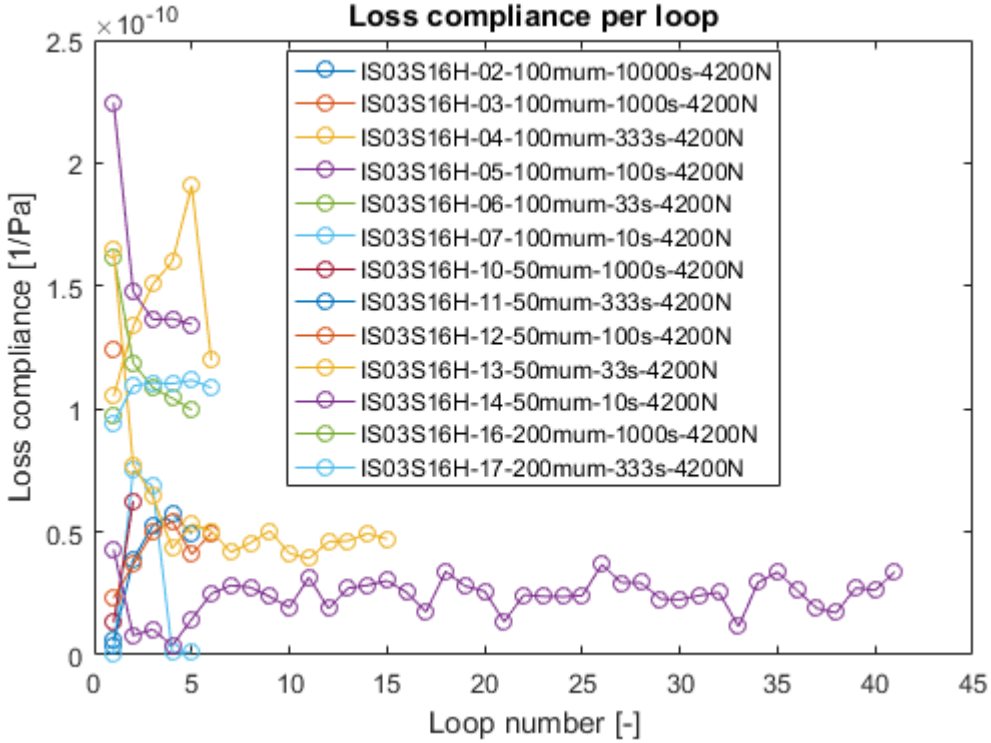

Figure 4.16 Loss compliance as function of loop number

4.4. Model predictions compared to experimental results

This work employs a model for the anelastic response of saline ice based on grain boundary relaxation. The parameters referring to this relaxation are denoted with a gb in superscript and dislocation relaxation with d in superscript. The latter dominates the behaviour for the experiments conducted, due to the strength of the relaxation being an order of magnitude higher. Here an overview of the input parameters required and model equations. The model is written in MATLAB and the code is found in Appendix B.

4.4.1. Input parameters

The required parameters to run the model are the experimental parameters, see Table 4.8, and the specimen parameters. Both the strain response to a cyclic stress history or the stress response to a cyclic strain history can be computed with this model.

Table 4.8 Experimental parameters

Symbol	Name		Unit	
$1/f$	Period		[Hz]	
σ_0	Stress amplitude		[MPa]	
n	Number of loops		$[-]$	
ε_0	Strain amplitude		$[-]$	

The model evaluates the stress response when zero is assigned to σ_0. In Table 4.9 the specimen specific parameters are listed. The values assigned to the dislocation relaxation parameters are based on (Cole, 1995). The temperature was for this experimental campaign not changed.

Table 4.9 Specimen parameters

Symbol	Name	Value	Unit
T	Temperature	-10	℃
α^d	Peak broadening factor dislocation relaxation	0.53	$-$
K^d	Stress restoring term	0.07	Pa
δD^d	Strength of dislocation relaxation	1.4×10^{-9}	Pa^{-1}
α^{gb}	Peak broadening factor grain boundary relaxation	0.6	$-$
B_0/K^{gb}	Pre-exponential term	8×10^{-28}	s^{-1}
Q^d	Activation energy dislocation relaxation	eV	eV

In Table 4.10 the specimen parameters that should remain constant are given.

Table 4.10 Constants

Symbol	Name	Value	Unit
b	Burgers vector	4.52×10^{-9}	$[-]$
E_U	Elastic modulus ice	9.0	GPa
B_0	Constant in drag term	1.205×10^{-9}	Pa s
Q	Activation energy grain boundary	1.32	eV
k	Boltzmann constant	8.617×10^{-5}	$\mathrm{eV\,K}^{-1}$

4.4.2. Implementation of model

The input parameters are all used in the equations. A cyclic stress or strain history is applied to the model. The loss, D_2 and storage compliance D_1 are calculated regardless of the type of input. When a stress history is given, D_1 and D_2 are used to calculate the strain response. However, the compliant complex modulus is derived, for a given strain history is given, the stress response is calculated.

For the comparison of the model predictions with the experimental data the strain amplitude measured by the external strain sensor is used.

4.4.3. Comparison of stress response as function of time

The experimentally obtained stress response of the material as a result of a cyclic strain history with a period of 100 s is shown in Figure 4.17. The model prediction of this experiment is shown in Figure 4.18. The stress amplitudes of both experiments are of approximately the same order. The phase difference seems to be of the same order of magnitude, but the time series are not the best instrument to assess the phase difference. The model prediction gives the steady-state response to a sinusoidal input, thus transient effects were not modelled.

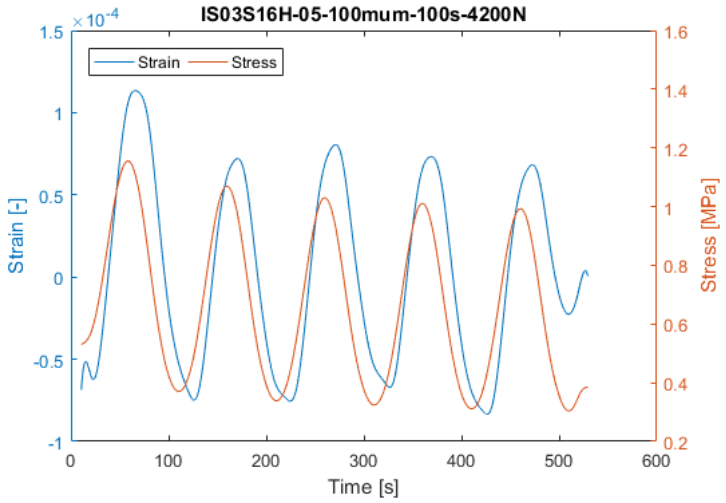

Figure 4.17 Experimental results

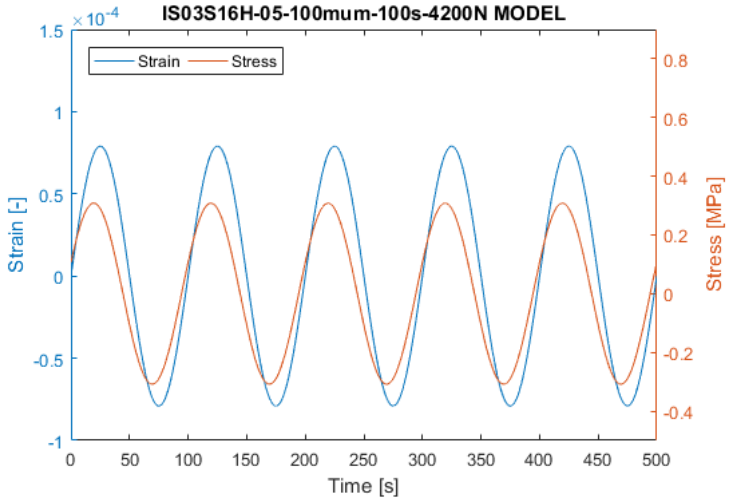

Figure 4.18 Model prediction repeated to show multiple cycles

4.4.4. Comparison of stress-strain curves

The stress-strain curves of the detrended experimental results are compared to a model prediction of the curve. The axes of the pair of figures have the same scale in Table TT.

For the experiment with a period of 10 000 s not enough cycles were performed to get to a steady state. In these experiments creep and stress relaxation seem to have a large influence on the results. The loop is closed when the period is 1000 s. The amplitudes are in the same range, however the area of the loops of the model prediction is smaller. The model is linear; thus it is not possible to simulate non-linearity. Two cycles are still not sufficient to see if the loops change over time. The first cycle of the experiments is heavily influenced by stress relaxation. To assess the stability of the loop shape at least two subsequent cycles are recommended.

The stress-strain curve of the experiments with a period of 333 s and 100 s matched well with the model predictions.

Table 4.11 Experimental and modelled stress-strain curves

Experimental results	Model prediction
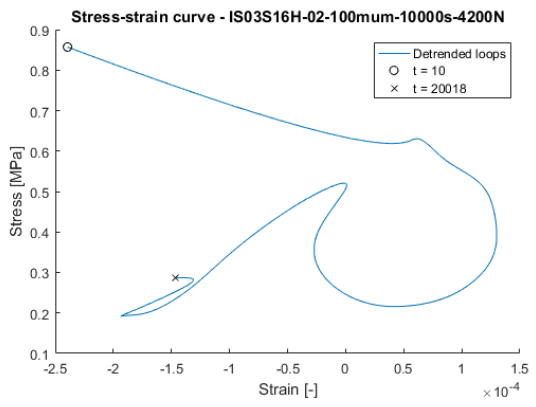	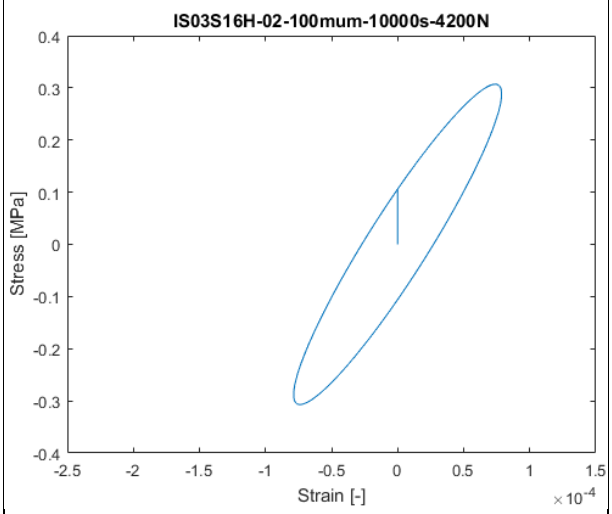

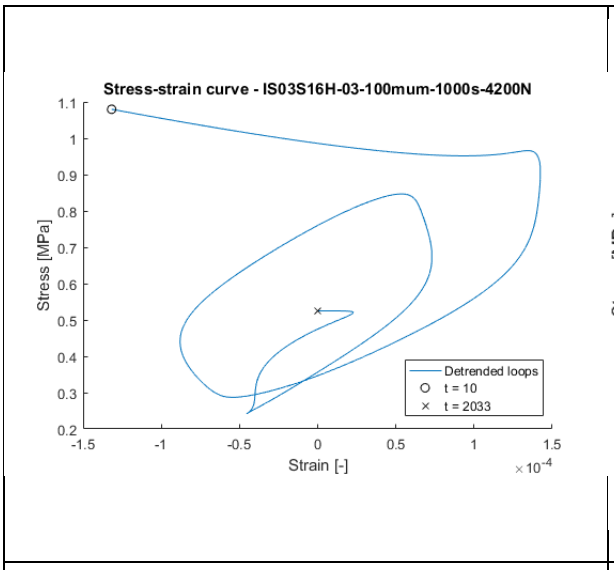
Stress-strain curve - IS03S16H-03-100mum-1000s-4200N
Stress [MPa]
Strain [-]
×10^-4
Detrended loops
t = 10
t = 2033

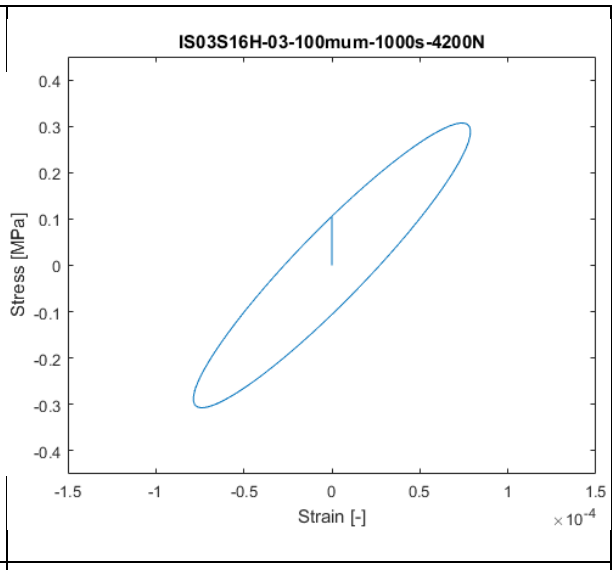
IS03S16H-03-100mum-1000s-4200N
Stress [MPa]
Strain [-]
×10^-4

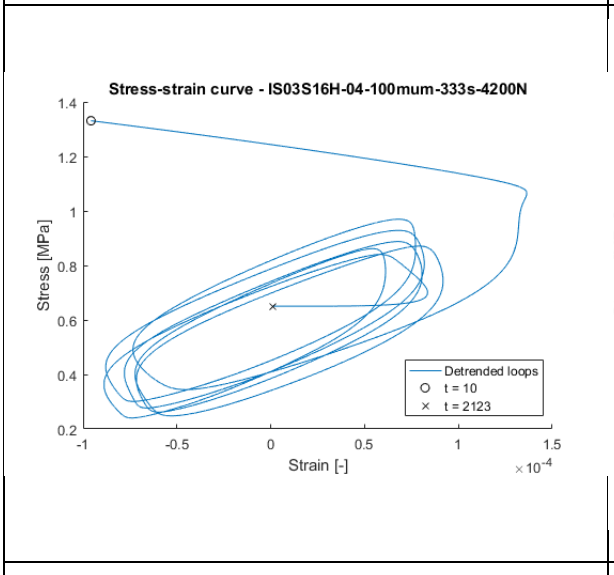
Stress-strain curve - IS03S16H-04-100mum-333s-4200N
Stress [MPa]
Strain [-]
×10^-4
Detrended loops
t = 10
t = 2123

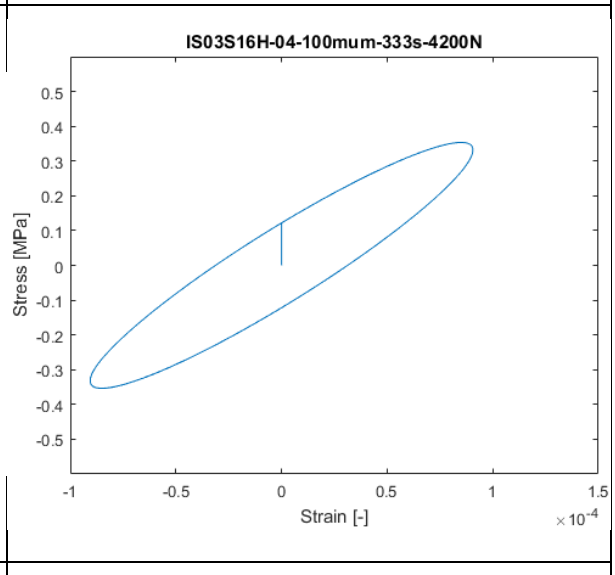
IS03S16H-04-100mum-333s-4200N
Stress [MPa]
Strain [-]
×10^-4

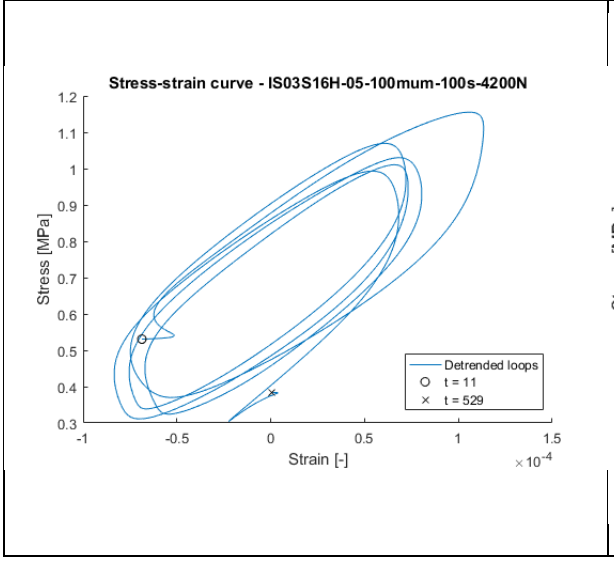
Stress-strain curve - IS03S16H-05-100mum-100s-4200N
Stress [MPa]
Strain [-]
×10^-4
Detrended loops
t = 11
t = 529

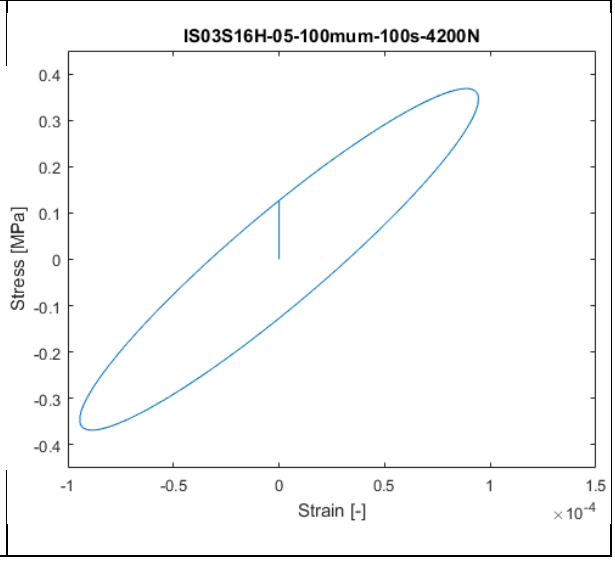
IS03S16H-05-100mum-100s-4200N
Stress [MPa]
Strain [-]
×10^-4

4.4.5. Dynamic compliances as function of frequency

The loss and storage compliance as a function of the frequency is plotted in Figure 4.19. In the figure, the loss compliance and storage of each loop of the experiments are plotted in the same graph. The loss compliance model prediction shows the same trend and magnitude as the experimental data points. The storage compliance resembles the data points for the double amplitude of 100 μm as shown in Figure 4.20. However, for the other amplitudes the model storage compliance is higher than the data points, especially for higher frequencies.

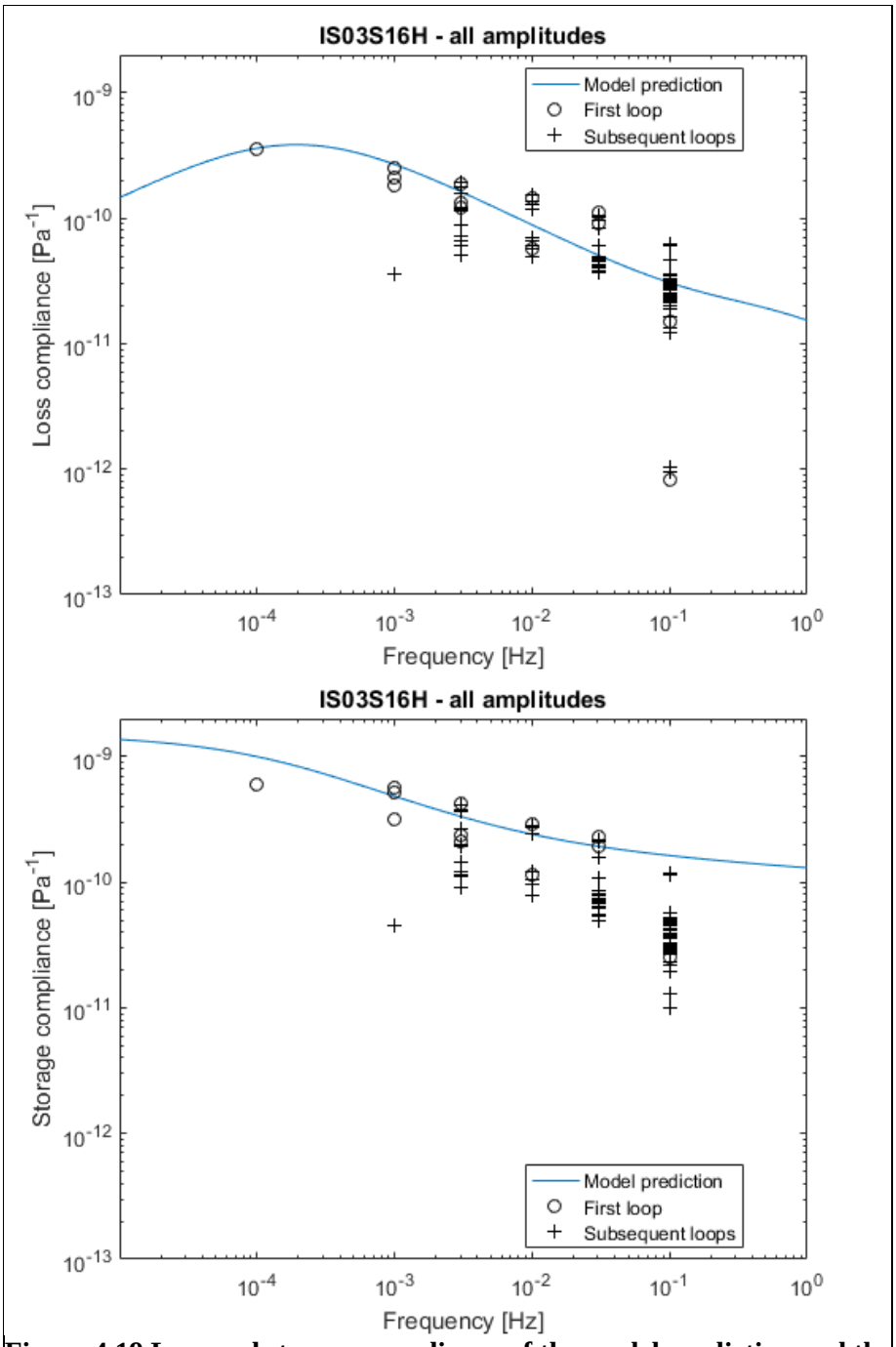

Figure 4.19 Loss and storage compliance of the model prediction and the experimentally obtained data points

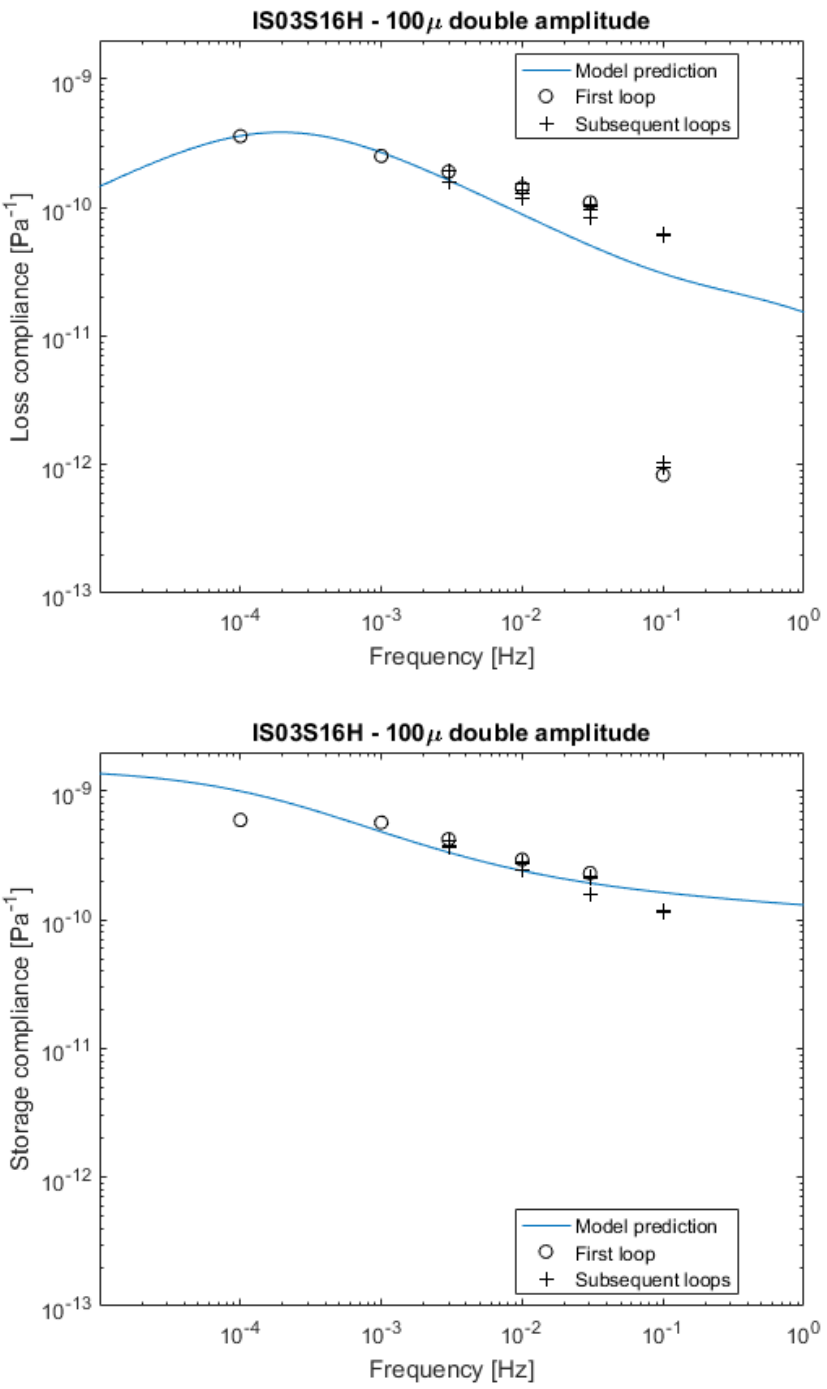

Figure 4.20 Loss and storage compliance of the model prediction and the experimentally obtained data points with a double amplitude of 100 μm.

5. Conclusions and recommendations

5.1. Conclusions

A successful experimental campaign on the cyclic straining of laboratory prepared sea ice was designed and conducted. A complete description of the experimental campaign is included in the work resulting in a reproducible method.

The model implemented, which was originally derived for stress control, was shown to be also useful for strain-controlled experiments by employing the reciprocal relation between the complex compliance and complex modulus.

The modelled steady-state response to a stress history or strain history matched well with the experimental observations, for both the individual experiments as the frequency dependence of the storage and loss compliance.

5.2. Recommendations for future work

5.2.1. Suggested improvements to experiments

No meaningful observation tests could be conducted with the current equipment, and therefore no precise measurements of the dislocation densities could be made. A strain sensor with a higher resolution is thus recommended. It is further recommended to assess the stiffness of the loading frame during these cyclic loading tests by using a calibrated specimen.

Control of the time-offset in the sinusoidal function for the stepper signal would be advantageous to prevent load and displacement jumps.

It is worth mentioning, that the development of the experiments was performed parallel to the assessment of their results, and therefore only the last specimen proved to be useful, with full control of stress history and temperature. If the described experimental campaign is to be repeated, more meaningful results are expected.

5.2.2. Suggested improvements to model

To improve the predictive merit of the model it would be beneficial if the model parameters were derived from the ice microstructure and not simply determined from literature

Furthermore, a study of the transient behaviour of the model could potentially illuminate further response characteristics, as could model studies with changing dislocation densities.

References

Baker, I. (2002) ‘Examination of Dislocations in Ice’, *Crystal Growth & Design*, 2(2), pp. 127–134. doi: 10.1021/cg0100282.

Baker, I., Liu, F., Jia, K. and Hu, X. (2000) ‘Dynamic observations of dislocation/grain-boundary interactions in ice’, *Annals of Glaciology*, 31, pp. 236–240. doi: 10.3189/172756400781820525.

Bueide, I. M. (2014) *Freeze-bond strength experiments ,*. Master thesis, Norwegian University of Science and Technology.

Callister, W. D. J. (2001) *Fundamentals of Materials Science and Engineering*, *Phoenix Usa*. doi: 10.1017/CBO9781107415324.004.

Cole, D. M. (1991) ‘Anelastic straining in polycrystalline ice’, in *Proceedings of the 6th International Specialty Conference on Cold Regions Engineering*, pp. 504–518.

Cole, D. M. (1995) ‘A model for the anelastic straining of saline ice subjected to cyclic loading’, *Philosophical Magazine A*, 72(1), pp. 231–248. doi: 10.1080/01418619508239592.

Cole, D. M. (1995) ‘A model for the anelastic straining of saline ice subjected to cyclic loading’, *Philosophical Magazine A*. Taylor {&} Francis, 72(1), pp. 231–248. doi: 10.1080/01418619508239592.

Cole, D. M. (1998) ‘Modeling the cyclic loading response of sea ice’, *Int. J. Solids Struct.*, 35(97), pp. 4067–4075. doi: 10.1016/S0020-7683(97)00301-6.

Cole, D. M. (2001) ‘The microstructure of ice and its influence on mechanical properties’, *Engineering Fracture Mechanics*, 68(17–18), pp. 1797–1822. doi: 10.1016/S0013-7944(01)00031-5.

Cole, D. M. and Durell, G. D. (1995) ‘The cyclic loading of saline ice’, *Philosophical Magazine A*, 72(1), pp. 209–229. doi: 10.1080/01418619508239591.

Cole, D. M., Johnson, R. A. and Durell, G. D. (1996) ‘The cyclic loading response of aligned first-year sea ice’, in *IAHR 13th Int’l. Ice Symp., Beijing*, pp. 1–7.

Cole, D. M., Johnson, R. A. and Durell, G. D. (1998) ‘The cyclic loading and creep response of aligned first-year sea ice’, *J. Geophys Res.*, 103(No. C10), p. 21,751 – 21, 758.

Cox, G. F. N. and Weeks, W. F. (1983) ‘Equations for determining the gas and brine volume in sea-ice sample’, *Journal of Glaciology*, 29(102), pp. 306–316.

Cox, G. F. N. and Weeks, W. F. (1986) ‘Changes in the salinity and porosity of sea-ice samples during shipping and storage’, *Journal of Glaciology*, 32(112), pp. 371–375.

Dempsey, J. P. (2000) ‘Research trends in ice mechanics’, *International Journal of Solids and Structures*, 37(1–2), pp. 131–153. doi: 10.1016/S0020-7683(99)00084-0.

Gautier, D. L., Bird, K. J., Charpentier, R. R., Grantz, A., Houseknecht, D. W., Klett, T. R., Moore, T. E., Pitman, J. K., Schenk, C. J., Schuenemeyer, J. H., Sorensen, K., Tennyson, M. E., Valin, Z. C. and Wandrey, C. J. (2009) ‘Assessment of Undiscovered Oil and Gas in the Arctic’, *Science*, 324(5931), pp. 1175–1179. doi: 10.1126/science.1169467.

Glen, J. W. (1974) *The physics of ice*. Hanover, N.H.: Corps of Engineers, U.S. Army, Cold Regions Research and Engineering Laboratory.

Granskog, M., Kaartokallio, H., Kuosa, H., Thomas, D. N. and Vainio, J. (2006) ‘Sea ice in the Baltic Sea - A review’, *Estuarine, Coastal and Shelf Science*, 70(1–2), pp. 145–160. doi: 10.1016/j.ecss.2006.06.001.

Gulas, S., Downton, M., D’Souza, K., Hayden, K. and Walker, T. R. (2017) ‘Declining Arctic Ocean oil and gas developments: Opportunities to improve governance and environmental pollution control’, *Marine Policy*. Elsevier, 75(June 2016), pp. 53–61. doi: 10.1016/j.marpol.2016.10.014.

Hendrikse, H. (2017) *Ice-induced vibrations of vertically sided offshore structures*. doi: 10.4233/uuid:325ebcfb-f920-400c-8ef6-21b2305b6920.

Hondoh, T. (2000) ‘Nature and behavior of dislocations in ice’, *Physics of Ice Core Records*, pp. 3–24.

Irgens, F. (2008) *Continuum mechanics, Continuum Mechanics*. Bergen: Springer-Verlag Heidelberg. doi: 10.1007/978-3-540-74298-2.

Kolari, K. (2016) ‘23 r d IAHR International Symposium on Ice Strain-Rate Softening of Granular Ice in Brittle Regime : Fact or Artifact ?’, pp. 1–8.

Kovacs, A. (1996) *Sea Ice: Part I. Bulk Salinity Versus Ice Floe Thickness*. Hanover, New Hampshire.

Kressel, H. and Brown, N. (1967) ‘Lattice defects in shock-deformed and cold-worked nickel’, *Journal of Applied Physics*, 38(4), pp. 1618–1625. doi: 10.1063/1.1709733.

Lakes, R. (2009) ‘Viscoelastic Materials’, *Viscoelastic Materials*, pp. 1–461. doi: 10.1017/CBO9780511626722.

Lakki, A., Schaller, R., Nauer, M. and Carry, C. (1993) ‘High temperature superplastic creep and internal friction of yttria doped zirconia polycrystals’, *Acta Metallurgica Et Materialia*, 41(10), pp. 2845–2853. doi: 10.1016/0956-7151(93)90099-E.

Lavrov, V. V. (1971) ‘Deformation and strength of ice’, in *Problems of the Physics and Mechanics of Ice*, p. 170.

Mellor, M. and Cole, D. (1981) ‘Cyclic loading and fatigue in ice’, *Cold Regions Science and Technology*, 4, pp. 41–53.

Myklebust, T. O. (2014) *Equipment and Production of Columnar Sea Ice Replica in NTNU Cold Lab*. Master thesis NTNU.

Nowick, A. S. and Berry, B. S. (1972) *Anelastic Relaxation in Crystalline Solids*. New York: Academic Press.

Pounder, E. R. (1965) ‘The physics of ice’, *Oxford, Pergamon press Library of Congress Catalog*, No. 65.211, p. 151 p.

Pustogvar, A. and Kulyakhtin, A. (2016) ‘Sea ice density measurements. Methods and uncertainties’, *Cold Regions Science and Technology*. Elsevier B.V., 131, pp. 46–52. doi: 10.1016/j.coldregions.2016.09.001.

Schulson, E. M. (1990) ‘The brittle compressive fracture of ice’, *Acta Metallurgica Et Materialia*, 38(10), pp. 1963–1976. doi: 10.1016/0956-7151(90)90308-4.

Schulson, E. M. and Duval, P. (2009) ‘Creep and fracture of ice’.

Schulson, E. M. and Duval, P. (2009) *Creep and Fracture of Ice, Cambridge University Press*. Cambridge: Cambridge University Press. doi: 10.1017/CBO9780511581397.

Shaw, R. A., Durant, A. J. and Mi, Y. (2005) ‘Heterogeneous Surface Crystallization Observed in Undercooled Water’, *The Journal of Physical Chemistry B*, 109(20), pp. 9865–9868. doi: 10.1021/jp0506336.

Sinha, N. K. (1977) ‘Instruments and methods technique for studying structure of sea ice’, *Journal of Glaciology*, 18(79), pp. 315–324.

Sinha, N. K. (1978) ‘Rheology of columnar-grained ice’, *Experimental Mechanics*, 18(12), pp. 464–470. doi: 10.1007/BF02324282.

Thomas, D. N. (2016) *Sea Ice*. Wiley. Available at: https://books.google.nl/books?id=3h3NDQAAQBAJ.

Timco, G. W. and Weeks, W. F. (2010) ‘A review of the engineering properties of sea ice’, *Cold Regions Science and Technology*. Elsevier B.V., 60(2), pp. 107–129. doi: 10.1016/j.coldregions.2009.10.003.

Weeks, W. . and Ackley, S. F. (1982) *The growth, structure, and properties of sea ice*. Hanover, New Hampshire 03755.

Weertman, J. (1955) ‘Theory of steady-state creep based on dislocation climb’, *Journal of Applied Physics*, 26(10), pp. 1213–1217. doi: 10.1063/1.1721875.

Whitworth, R. W. (1978) ‘THE CORE STRUCTURE AND THE MOBILITY OF’.

Wilson, C. and Marmo, B. (2000) ‘Flow in polycrystalline ice’, *Journal of the Virtual Explorer*, 2. doi: 10.3809/jvirtex.2000.00023.

Wu, H. C., Chang, K. J. and Schwarz, J. (1976) ‘Fracture in the compression of columnar gained ice’, *Engineering Fracture Mechanics*, 8(2), pp. 365–370. doi: 10.1016/0013-7944(76)90016-3.

Appendix A1 – Code for model

```
%% Model
% 26/07/2017
%
clear all
close all

%% Experimental parameters
period = 100; %[s] period
s_0 = 0; %[Pa] input stress amplitude
n = 3; % [-] number of loops
e_0 = .95E-4; %[-] input strain amplitude

%% Check for input and response
M = {'Stress','[MPa]';'Strain','[-]'};

if e_0==0
    in_0=s_0;
    exp_nr = 1;
else
    in_0=e_0;
    exp_nr = 2;
end



%% Specimen parameters
T_C = -10; %[C]
% dislocation relaxation
parameters = {'HOF1',1.4E-9,.53,.07;'HOF2',1.4E-9,.53,.07;
    'HOP2',1.4E-9,.55,.05;'PL19',1.8E-9,.59,.07}; %[name,dD,alpha,K]
specimen = 2;
alpha_d = parameters{specimen,3}; %[-]
K = parameters{specimen,4}; %[-]
dD_d = parameters{specimen,2}; %[m-2]

% grain boundary relaxations
dD_gb = 3E-11; %[Pa]
alpha_gb = 0.6;%[-]
Q_gb = 1.32; %[eV]
pre_exp = 8E-28;

%% calculated parameters
% experiment
w = 2*pi./period; %[rad/s] angular frequency
f = 1./period; %[Hz] frequency
fs = 20; %[Hz] "sampling" frequency
t  = linspace(0,period*n,fs*n*period); % [s] timearray
input = imag(in_0*exp(1i*w*t)); % [MPa] timeseries input signal
T = 273.15+T_C; %[K]

% constants
k = 8.617E-5;
Mu = 9E9; %[Pa] unrelaxed modulus
O = pi^-1; % value for horizontal values
b = 4.52E-10;
B_0 = 1.205E-9;
Q = 0.55;
rho = dD_d*K/(O*b^2);
```

```
% equations for all parameters of compliances
B_d = B_0*exp(Q/(k*T));
B_gb = pre_exp*exp(Q_gb/(k*T));
tau_d = B_d/K;
tau_gb = B_gb/K;
si_d  = log(tau_d*w);
si_gb = log(tau_gb*w);
% dD_d = D*O*b^2/K;
Du_d = 1/Mu;
Du_gb = 1/Mu;

% parameters for loss and storage compliance plot
f2 = logspace(-7,3,100);
w2 = 2*pi*f2;

%% Dynamic compliances
% per experiment
[D1_d,D2_d] = compliances(Du_d,dD_d,alpha_d,si_d);
[D1_gb,D2_gb] = compliances(Du_gb,dD_gb,alpha_gb,si_gb);
D1 = D1_d+D1_gb-Du_d;
D2 = D2_d+D2_gb;
D_im = D1-1i*D2;

% as function of f
si_d2 = log(tau_d*w2);
si_gb2 = log(tau_gb*w2);
[D1_d2,D2_d2] = compliances(Du_d,dD_d,alpha_d,si_d2);
[D1_gb2,D2_gb2] = compliances(Du_gb,dD_gb,alpha_gb,si_gb2);

%% stress and strain functions
output = imag(in_0*((D_im)^(-2*exp_nr+3))*exp(1i*w*t));

if exp_nr ==1
    stress = input;
    strain = output;
else
    stress = output;
    strain = input;
end

%% plot signals
figure(1)
subplot(2,1,1)
plot(t,input)
subplot(2,1,2)
plot(t,output)

figure(2)
plot(strain,stress)
```

Appendix A2 – Function for dynamic compliances

```
function [ D1,D2 ] = compliances( Du,dD,alpha,s )
%UNTITLED Summary of this function goes here
%   Detailed explanation goes here
D1  = Du + dD.*(1-(2/pi).*atan(exp(alpha.*s)));
D2  = alpha.*dD.*1./(exp(alpha.*s)+exp(-alpha.*s));


end
```

Appendix B – Start times IS03S16H

Experiment	Start time
IS03S16H-01-20mum-10s-800N	9:57
IS03S16H-02-100mum-10000s-4200N	10:18
IS03S16H-03-100mum-1000s-4200N	16:15
IS03S16H-04-100mum-333s-4200N	17:15
IS03S16H-05-100mum-100s-4200N	18:10
IS03S16H-06-100mum-33s-4200N	18:39
IS03S16H-07-100mum-10s-4200N	19:03
IS03S16H-08-20mum-10s-800N	19:25
IS03S16H-09-20mum-10s-800N	10:53
IS03S16H-10-50mum-1000s-4200N	11:40
IS03S16H-11-50mum-333s-4200N	12:40
IS03S16H-12-50mum-100s-4200N	13:36
IS03S16H-13-50mum-33s-4200N	14:10
IS03S16H-14-50mum-10s-4200N	14:44
IS03S16H-15-20mum-10s-800N	15:11
IS03S16H-16-200mum-1000s-4200N	15:36
IS03S16H-17-200mum-333s-4200N	16:38
IS03S16H-18-200mum-100s-4200N	17:33
IS03S16H-19-0mum-s-4200N	

Appendix C – Stress-strain curves specimen IS03S16H

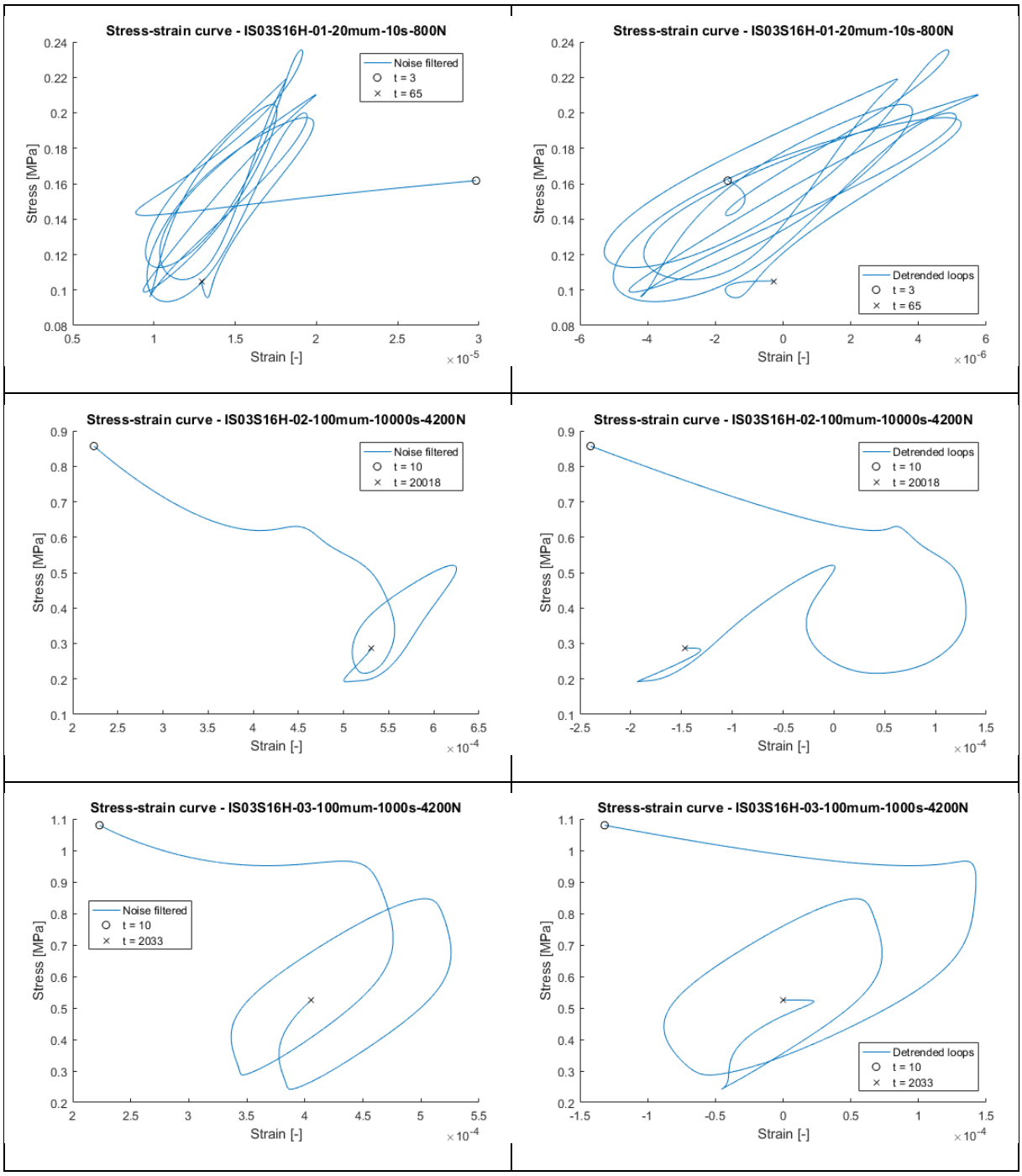

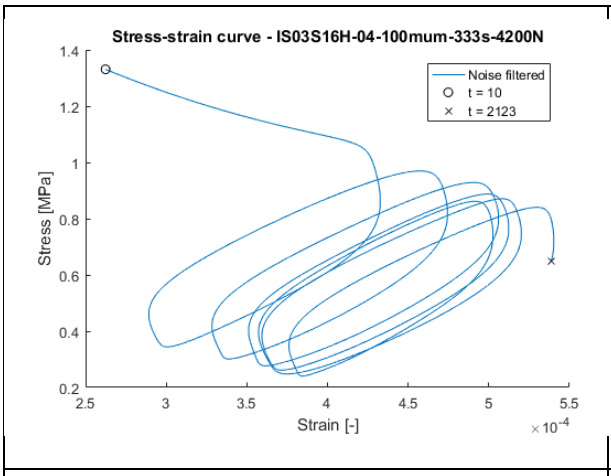
Stress-strain curve - IS03S16H-04-100mum-333s-4200N
Noise filtered
t = 10
t = 2123
Stress [MPa]
Strain [-]
×10^-4

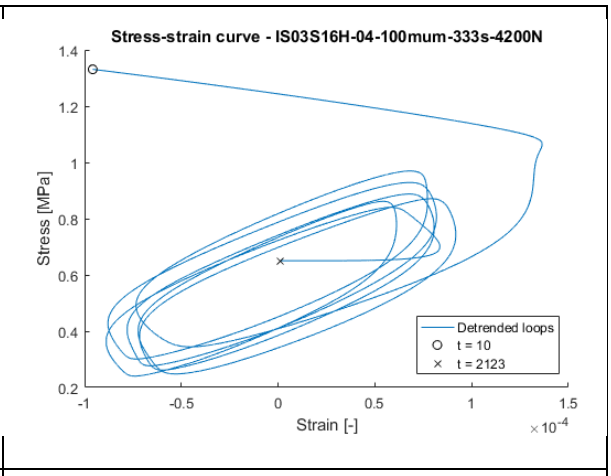
Stress-strain curve - IS03S16H-04-100mum-333s-4200N
Detrended loops
t = 10
t = 2123
Stress [MPa]
Strain [-]
×10^-4

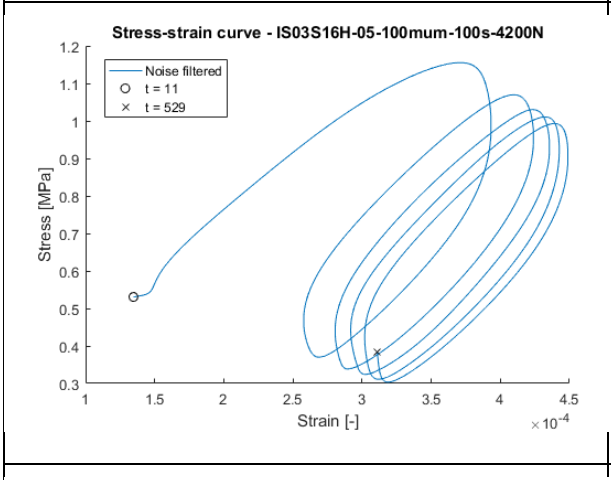
Stress-strain curve - IS03S16H-05-100mum-100s-4200N
Noise filtered
t = 11
t = 529
Stress [MPa]
Strain [-]
×10^-4

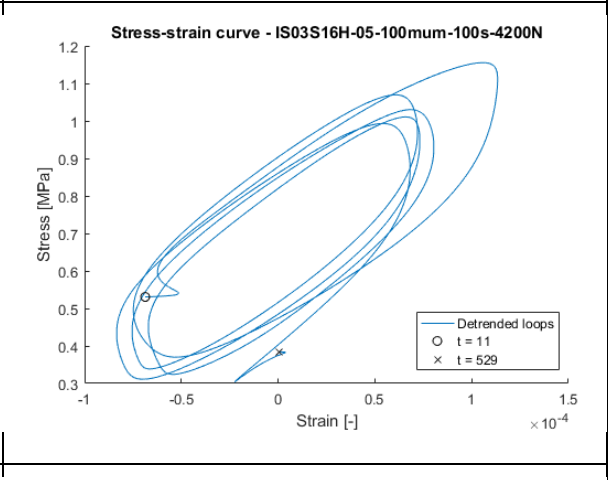
Stress-strain curve - IS03S16H-05-100mum-100s-4200N
Detrended loops
t = 11
t = 529
Stress [MPa]
Strain [-]
×10^-4

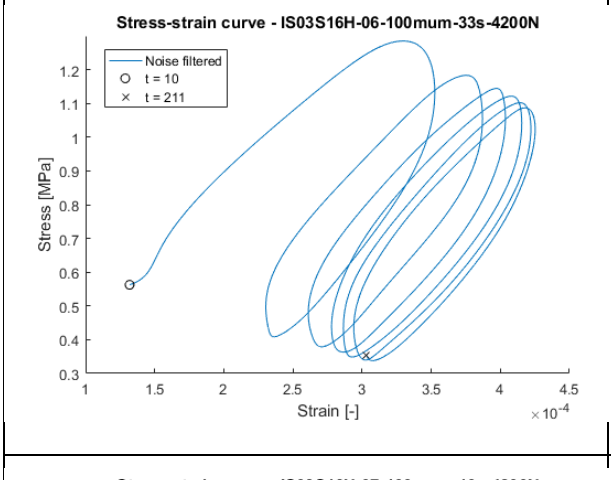
Stress-strain curve - IS03S16H-06-100mum-33s-4200N
Noise filtered
t = 10
t = 211
Stress [MPa]
Strain [-]
×10^-4

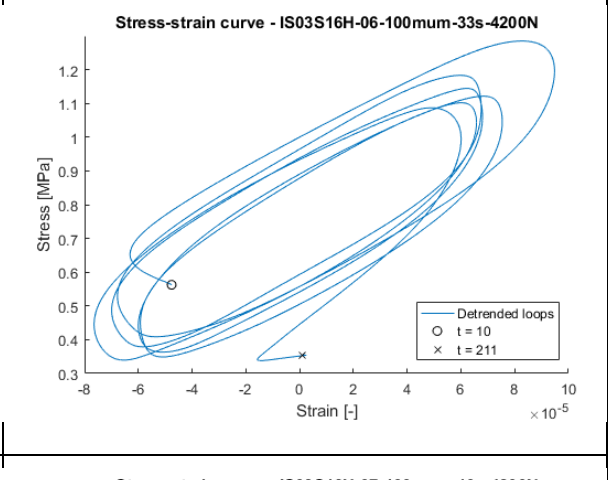
Stress-strain curve - IS03S16H-06-100mum-33s-4200N
Detrended loops
t = 10
t = 211
Stress [MPa]
Strain [-]
×10^-5

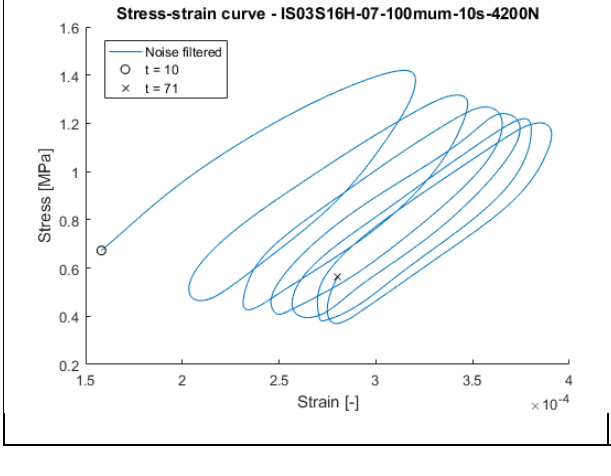
Stress-strain curve - IS03S16H-07-100mum-10s-4200N
Noise filtered
t = 10
t = 71
Stress [MPa]
Strain [-]
×10^-4

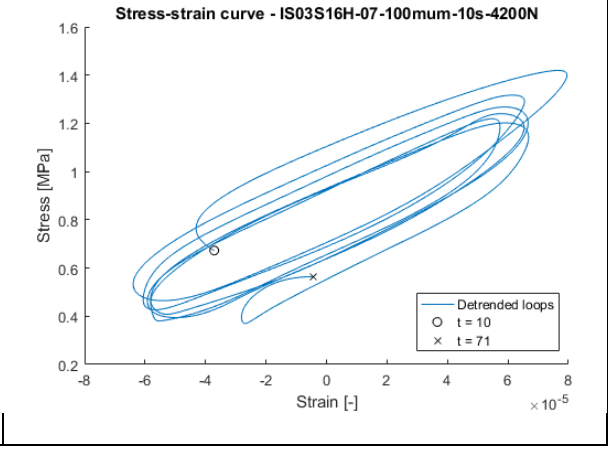
Stress-strain curve - IS03S16H-07-100mum-10s-4200N
Detrended loops
t = 10
t = 71
Stress [MPa]
Strain [-]
×10^-5

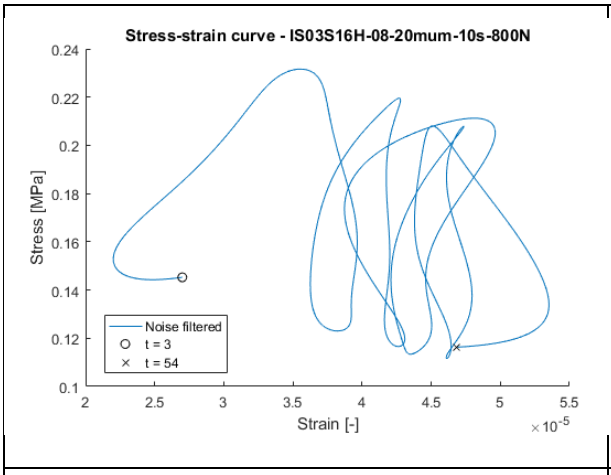
Stress-strain curve - IS03S16H-08-20mum-10s-800N
Stress [MPa]
Strain [-]
×10^-5
Noise filtered
t = 3
t = 54

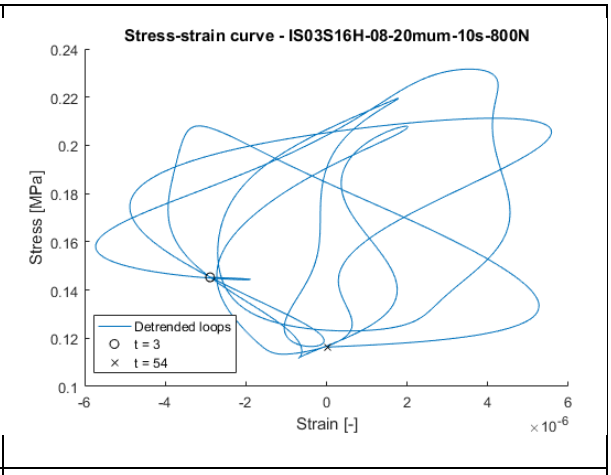
Stress-strain curve - IS03S16H-08-20mum-10s-800N
Stress [MPa]
Strain [-]
×10^-6
Detrended loops
t = 3
t = 54

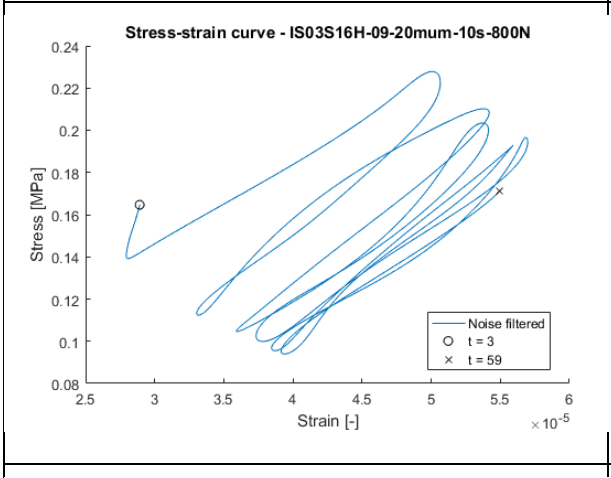
Stress-strain curve - IS03S16H-09-20mum-10s-800N
Stress [MPa]
Strain [-]
×10^-5
Noise filtered
t = 3
t = 59

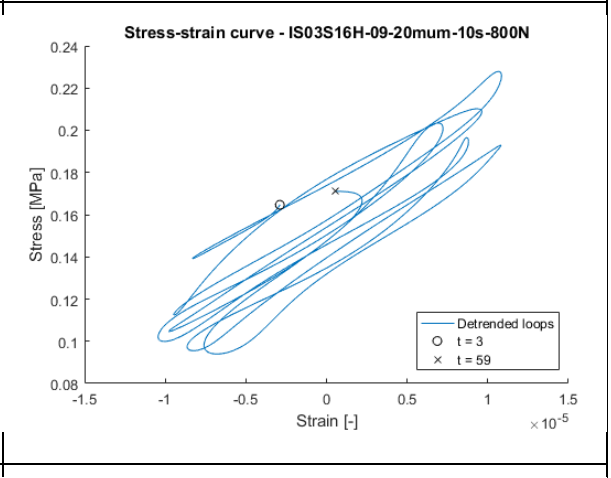
Stress-strain curve - IS03S16H-09-20mum-10s-800N
Stress [MPa]
Strain [-]
×10^-5
Detrended loops
t = 3
t = 59

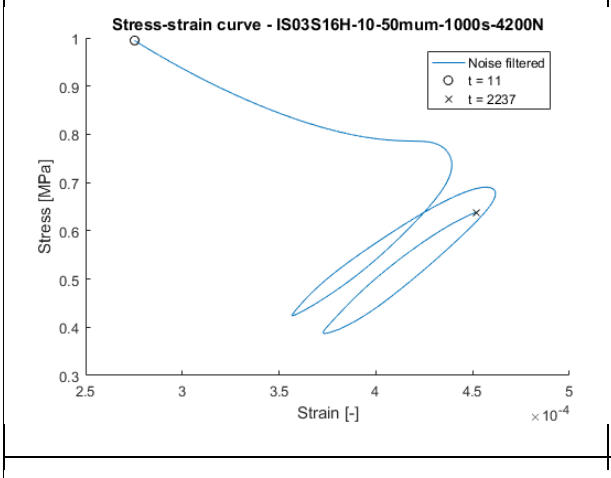
Stress-strain curve - IS03S16H-10-50mum-1000s-4200N
Stress [MPa]
Strain [-]
×10^-4
Noise filtered
t = 11
t = 2237

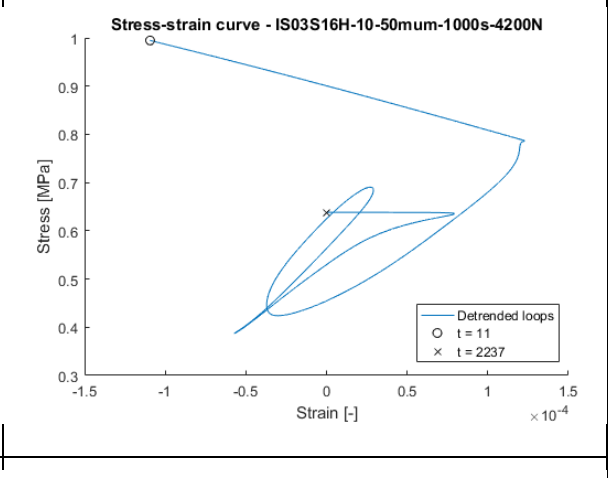
Stress-strain curve - IS03S16H-10-50mum-1000s-4200N
Stress [MPa]
Strain [-]
×10^-4
Detrended loops
t = 11
t = 2237

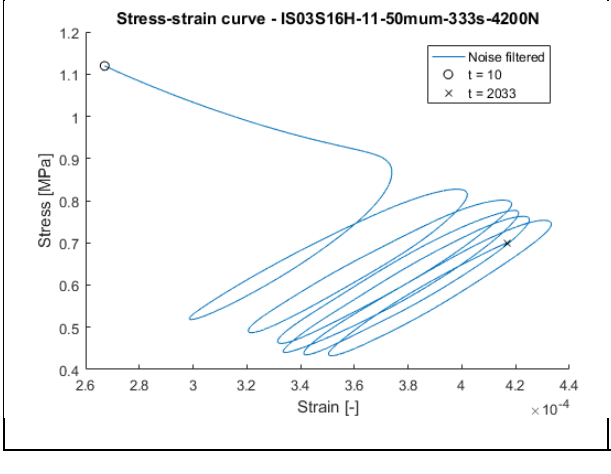
Stress-strain curve - IS03S16H-11-50mum-333s-4200N
Stress [MPa]
Strain [-]
×10^-4
Noise filtered
t = 10
t = 2033

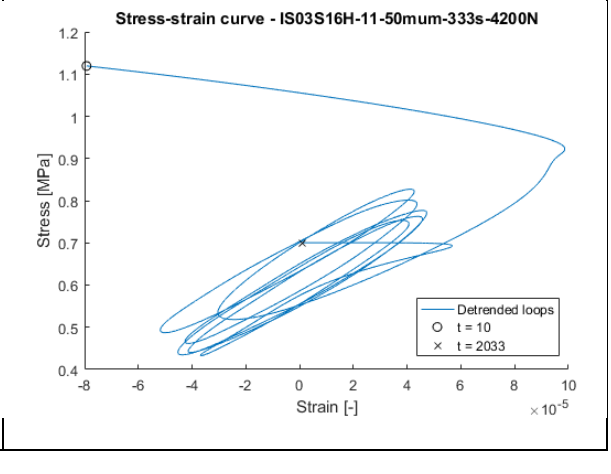
Stress-strain curve - IS03S16H-11-50mum-333s-4200N
Stress [MPa]
Strain [-]
×10^-5
Detrended loops
t = 10
t = 2033

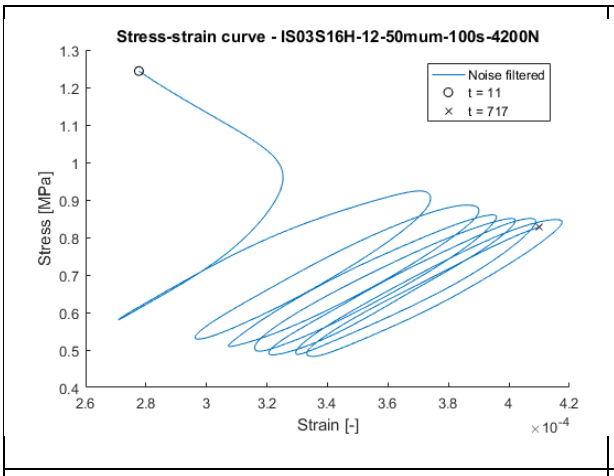
Stress-strain curve - IS03S16H-12-50mum-100s-4200N
Noise filtered
t = 11
t = 717
Stress [MPa]
Strain [-]
×10^-4

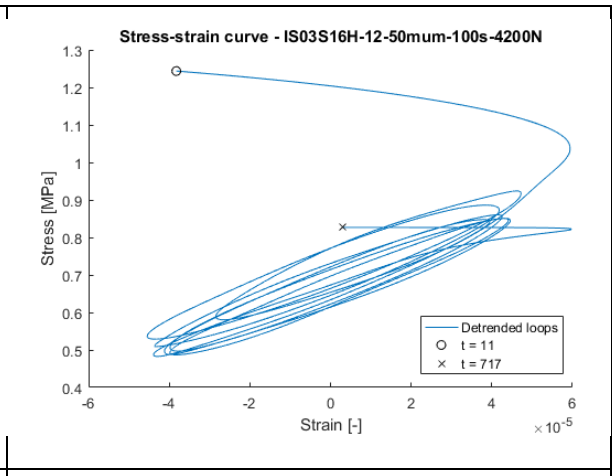
Stress-strain curve - IS03S16H-12-50mum-100s-4200N
Detrended loops
t = 11
t = 717
Stress [MPa]
Strain [-]
×10^-5

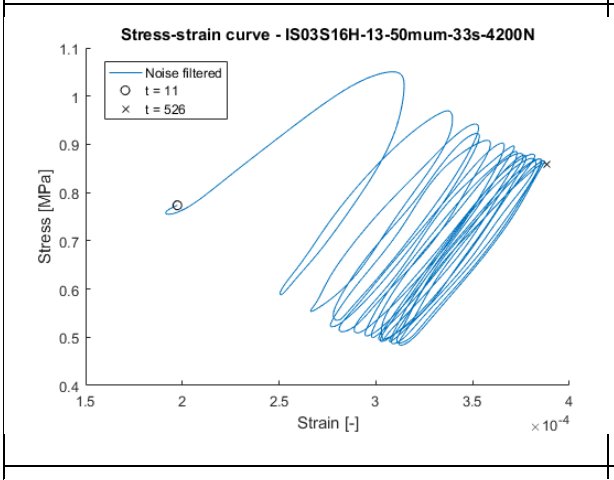
Stress-strain curve - IS03S16H-13-50mum-33s-4200N
Noise filtered
t = 11
t = 526
Stress [MPa]
Strain [-]
×10^-4

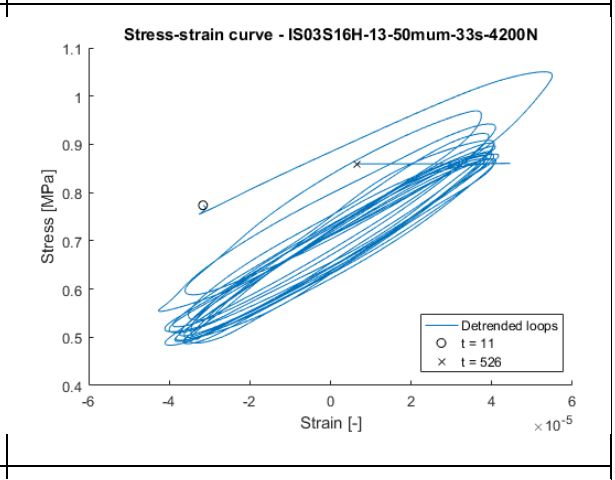
Stress-strain curve - IS03S16H-13-50mum-33s-4200N
Detrended loops
t = 11
t = 526
Stress [MPa]
Strain [-]
×10^-5

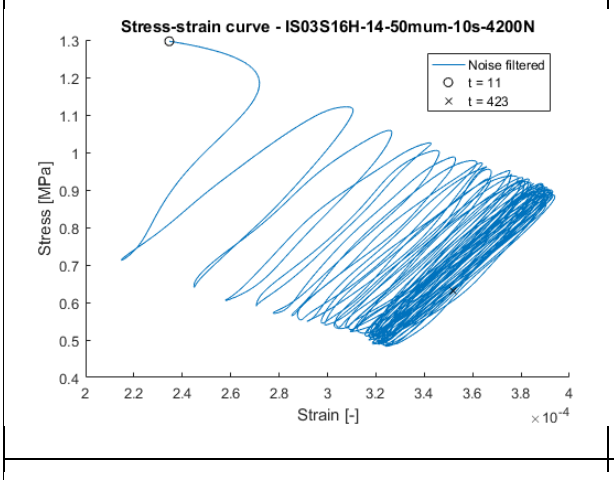
Stress-strain curve - IS03S16H-14-50mum-10s-4200N
Noise filtered
t = 11
t = 423
Stress [MPa]
Strain [-]
×10^-4

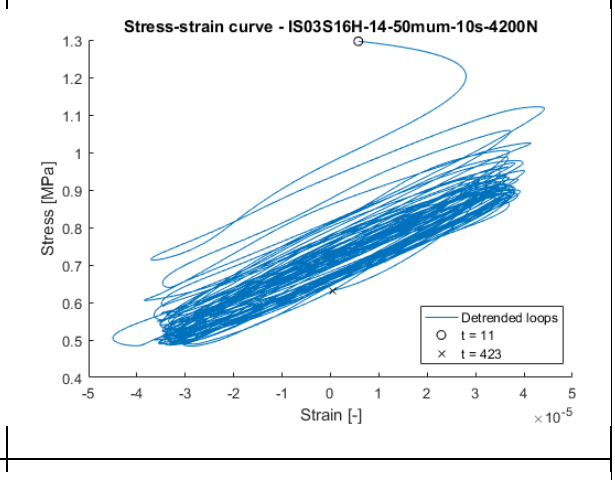
Stress-strain curve - IS03S16H-14-50mum-10s-4200N
Detrended loops
t = 11
t = 423
Stress [MPa]
Strain [-]
×10^-5

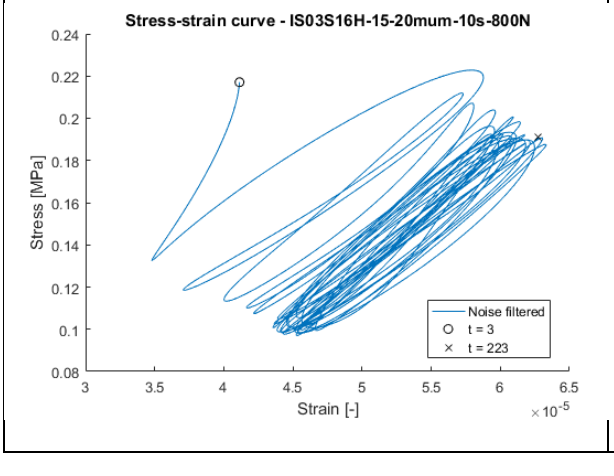
Stress-strain curve - IS03S16H-15-20mum-10s-800N
Noise filtered
t = 3
t = 223
Stress [MPa]
Strain [-]
×10^-5

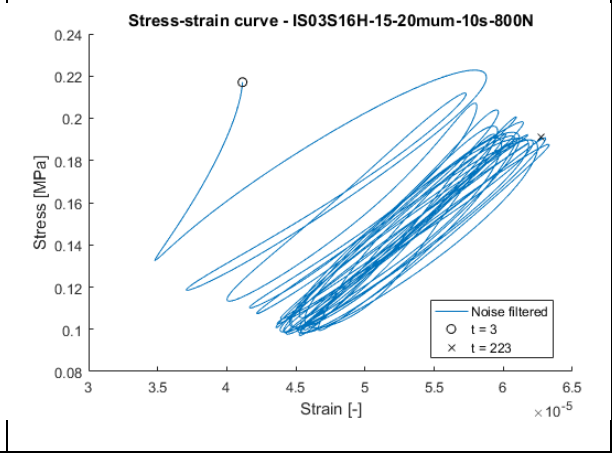
Stress-strain curve - IS03S16H-15-20mum-10s-800N
Noise filtered
t = 3
t = 223
Stress [MPa]
Strain [-]
×10^-5

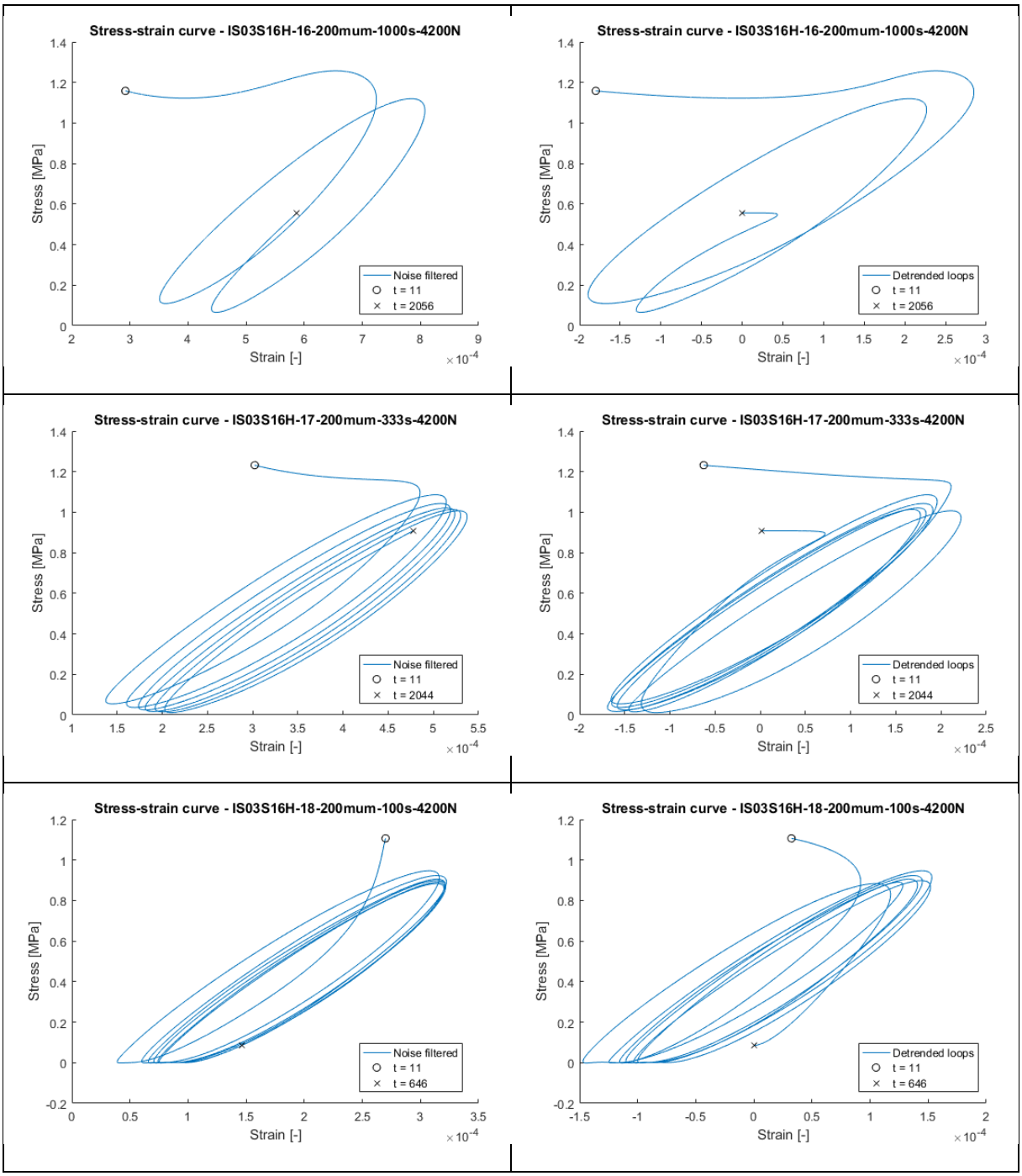
Stress-strain curve - IS03S16H-16-200mum-1000s-4200N
Stress [MPa]
Strain [-]
×10^-4
Noise filtered
t = 11
t = 2056
Stress-strain curve - IS03S16H-16-200mum-1000s-4200N
Stress [MPa]
Strain [-]
×10^-4
Detrended loops
t = 11
t = 2056
Stress-strain curve - IS03S16H-17-200mum-333s-4200N
Stress [MPa]
Strain [-]
×10^-4
Noise filtered
t = 11
t = 2044
Stress-strain curve - IS03S16H-17-200mum-333s-4200N
Stress [MPa]
Strain [-]
×10^-4
Detrended loops
t = 11
t = 2044
Stress-strain curve - IS03S16H-18-200mum-100s-4200N
Stress [MPa]
Strain [-]
×10^-4
Noise filtered
t = 11
t = 646
Stress-strain curve - IS03S16H-18-200mum-100s-4200N
Stress [MPa]
Strain [-]
×10^-4
Detrended loops
t = 11
t = 646